Air pollution modelling over complex topography

Gianluca Antonacci

UNIVERSITÀ DEGLI STUDI DI TRENTO

2004

Doctoral thesis in Environmental Engineering (XVI cycle)
Faculty of Engineering, University of Trento
Year: 2004
Supervisor: Prof. Marco Tubino

Università degli Studi di Trento
Trento, Italy
2004

dilution
is no longer the solution
to pollution:
avoiding pollution
is the best solution
to pollution!

Acknowledgements

The author wishes to thank Marco Tubino for rare but illuminating suggestions about the interpretation of data and providing valuable comments. Discussion with Dino Zardi was of great help to the author in focusing on the problem, especially from the meteorological point of view. Special thanks to Marco Ragazzi for useful suggestions and to Massimiliano de Franceschi for providing data acquired with the sonic anemometer

This work has been partly supported by the Environmental Protection Agency (APPA) of Bolzano and Trento, which have provided meteorological data used for testing the proposed conceptual tools.

Inoltre un grazie sentito agli amici e colleghi (prima amici che colleghi): Gianluca, Giuliano, Guido, Ilaria, Marco B & T, Walter e, last but not the least... Lauretta con cui condivido gli sforzi per la preparazione della tesi e con cui spero, in futuro, di condividere anche di più.

Contents

List of Figures

List of Tables

Foreword

The aim of this thesis is the study of pollutant dispersion in complex topographies. Two different contexts are considered, which correspond to two different spatial scales: the case of dispersion in valleys and the case of traffic-determined pollution in urban areas. Although the above contexts seem quite different, they share an analogous geometrical complexity.

In the last years environmental consciousness has been growing so much that very sophisticated tools are now required for monitoring and studying the effects of the anthropic activities on the atmosphere. In environmental planning complete information should be collected, in order to judge in an objective way the ongoing choices. Therefore, when pointing to a selected solution, a correct assessment of conceptual tools turns out to be essential. In particular, it is now quite established that the effects connected to human activities, and among these atmospheric pollution, have to be estimated on suitable spatial and time scales and different approaches have to be chosen depending on them.

Advances in the knowledge of atmospheric sciences in the last decades, along with the increased availability of computational resources, has allowed to achieve remarkable results in meteorological simulation by means of mathematical and numerical models; as a consequence, we now have reliable tools for the forecast of the atmospheric motions and the associated phenomena, among which the transport and chemical reactions of pollutants. However, while in meteorology there exists a consolidated flux of information from the scientific community to the customers of the numerical models, it seems that in the field of dispersion modelling, which is on the other hand closely related to the previous one, a cognitive gap remains. This sometimes leads the user to consider as "general purpose" models which are actually developed under restrictive hypothesis, different from those under which they are adopted (a clear example is the common adoption of "far field" models for studying "near field" dispersion processes). Hence, the main target of this work is not to supply instruments and results of general validity, but to highlight which the critical points

in air pollution modelling, focusing on those cases for which the adoption of "standard" procedures is not recommended.

In the first part air pollution modelling in mountainous terrain is examined. A three-dimensional lagrangian modelling is proposed which takes advantage of modified profiles of eddy diffusivity, expressly developed for complex orography. In fact, the estimate of pollutant dispersion over complex terrain has to be faced accounting, in the vertical and horizontal directions, for different spatial and temporal scales which are influenced by orography, wind regime and thermal balance. Both global and local approach for computing eddy diffusivity are studied and compared.

In the second part of present work the problem of traffic, determining pollution in urban areas, is tackled. Using the town of Trento as a study case, two models working at different scales are developed. The first model uses an eulerian finite-volume scheme and simulates dispersion over the whole urban area, explicitly accounting for roughness elements (i.e. the buildings); the second is a vertical two-dimensional lagrangian model which is able to simulate canyon effects in relatively narrow streets and the consequent trapping of pollutants. These two models are mainly suitable for studying acute pollution cases, for which highly resolved models are needed, since they work at relatively small time and spatial scales.

Part I.

Dispersion in valleys

1. Introduction to atmospheric physics

1.1. Dynamics in the atmospheric boundary layer

Stull (1988) defines the atmospheric boundary layer (ABL) as the part of the troposphere that is directly influenced by the presence of the earth surface, and responds to surface forcing with a time scale of about one hour or less. The local wind conditions in alpine valleys are often determined either by the topographic forcing of the meso-scale circulation or by thermally driven valley breezes. As a result, the circulation exhibits a complex pattern, which is neither homogeneous nor stationary, thus preventing the use of classical gaussian approaches for modeling pollutant dispersion and the resulting ground level concentrations. Hence, when modeling pollutant concentrations for the entire atmospheric boundary layer, the flow field has to be carefully investigated.

1.1.1. Time and space scales

Many layers characterize the vertical structure of atmosphere. Their time, vertical, and horizontal distance scales are different (see table 1.1).

The influence of earth surface roughness is limited to the troposphere, the lowest $10\,km$ layer of the atmosphere. In reality, on the time scale of one day, this influence is restricted to a smaller zone, the atmospheric boundary layer, which is characterized by complete mixing due to frictional drag. The boundary layer receives much of its heat and all of its water through the turbulent processes. Its height is not constant and depends on turbulence. During day-time, when the ground is heated by the sun, the upward transfer of heat into the cooler atmosphere increases the convection and extends the boundary layer depth to about $1 \div 2\,km$. During the night the ground is cooler than the atmosphere; therefore, the downward heat transfer suppresses mixing and the boundary layer may shrink to less than $100\,m$. This daily cycle may be disturbed by large scale weather events not related to local surface configuration or heating cycle. The upper horizontal scale limit of boundary layer is $50\,km$, and the vertical scale of about $1\,km$. The turbulent surface layer is characterized by intense small-scale turbulence generated by the surface roughness and convection, which

Table 1.1.: Time and distance magnitude scales for atmospheric layers (adapted from Santamouris and Dascalaki, 2003).

Layer	Time	Horizontal distance	Vertical distance
Troposphere	*days*	$\sim 500\,km$	$\sim 10\,km$
Atm. bound. layer	$\sim 1\,hour$	$\sim 50\,km$	$\sim 1\,km$
Surface layer	$\sim 10\,min$	$\sim 1\,km$	$10 \div 100\,m$
Roughness layer	*seconds*	$1 \div 5\,elem.\,height$	$1 \div 5\,elem.\,height$

displays strong fluctuations over short periods of time (seconds). During the day its height is about $50\,m$ while during night-time reduces to few meters.

The roughness layer extends around the surface elements to at least $1 \div 5$ times their vertical and horizontal size. The flow of this layer is highly irregular being affected by the nature of the obstacles (Santamouris and Dascalaki, 2003).

The depth of the ABL may vary in space due to orographic characteristics. Moreover, the structure of the layer varies along the day. According to Stull (1988) three main patterns can be distinguished: the mixed layer, the residual layer and the stable boundary layer (see figure 1.1).

We may notice that in the surface layer the vertical fluxes (momentum, heat, humidity) are considered nearly constant. It is generally assumed that the surface layer has a depth which is more or less 10% of the entire ABL, both in the case of stable layer and of mixed layer. In the latter case turbulence, to which fluxes are related, is mainly convective: vortexes arise, whose dimensions are of the order of magnitude of the mixing layer itself; warm air updrafts and cold air downdrafts are therefore observed. The solar heating causes thermal plumes to rise, transporting moisture, heat and momentum. The plumes rise and expand adiabatically until a thermodynamic equilibrium is reached at the top of the atmospheric boundary layer.

On the other hand the stable boundary layer is mainly characterized by mechanical turbulence (shear effect).

1.1.2. The daily cycle of the atmospheric boundary layer

Pollutant emissions are often due to sources located near to the ground: therefore, transport processes mainly occur within the lower region of the atmosphere.

In general the conceptual scheme for the boundary layer is developed with reference to flat uniform terrain and synoptic fair weather condition. Under the hypothesis of horizontal

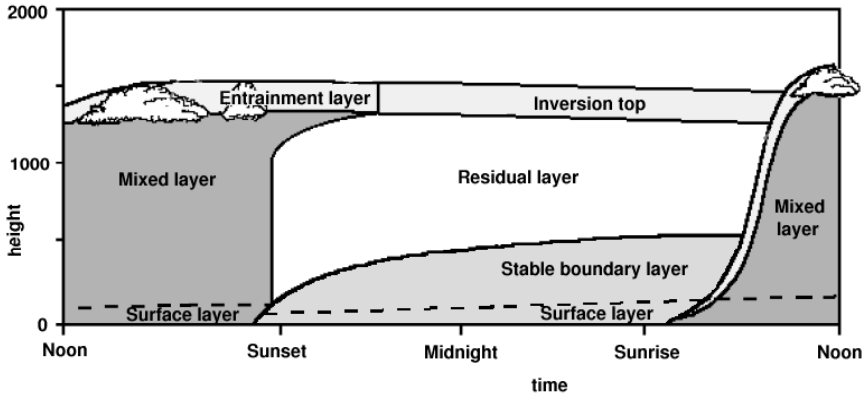

Figure 1.1.: Daily evolution of the atmospheric boundary layer (Stull, 1988).

homogeneity, the average values of temperature, flow field and heat flux, turn out to depend only on the height over the ground (Lumley and Panofsky, 1964).

Heterogeneous surfaces affect the ABL in several ways. Local surface properties (water vs. land, field vs. forest) lead to differences in surface fluxes of momentum, heat and moisture. The resulting uneven surface fluxes combine with terrain irregularities to generate both standing and transient eddies, which can modify the local turbulent fluxes. A peculiar feature of complex terrain meteorology is the occurrence of up-valley (anabatic) wind during day-time and down-valley (catabatic) wind, typically during night-time, caused by the different heating of valley floor and mountains ridges. Secondary circulations are often observed for the same reason, which are characterized by up- and down-slope flows on the sides of the valleys. Hence, in a valley, both the mechanical and the thermal boundary condition, are different with respect to flat uniform terrain and the daily cycle of the boundary layer is more complex (Whiteman, 1982).

1.1.3. Meteorological modelling

Simulation of dispersion processes requires an adequate characterization of the flow field and stability within the ABL. In the last years, the increasing knowledge on the structure of the ABL, along with the growth of computational possibilities has lead to the development of numerical models which may simulate quite accurately the meteorological evolution at various time and spatial scales. For a review on this subject see Haltiner (1980); Pielke (2002). These models solve numerically the equations governing the atmospheric motion, by using physical principles and suitable parameterizations. However the complexity of

the problem still prevent from simulating the ABL evolution at each scale. Different types of models are thus adopted, which are often framed within a "nesting" procedure, from the largest to the smallest scale.

Numerical models can be classified as prognostic or diagnostic. The first type is used to forecast the evolution in time of meteorological conditions, while the second type of models simulates the field of meteorological quantities over a given domain starting from real acquired data. Among the diagnostic models, the so-called "mass consistent" model uses the mass-conservation instead of solving the flow equations. In the present work the analysis of the flow field will be carried out with the mass-consistent diagnostic model CALMET, released by EarthTech Inc. (Scire et al., 1999). The model predicts flow and temperature field are predicted by CALMET on a three-dimensional grid, accounting for the presence of orography, while turbulence parameters (friction velocity, Obukhov length, stability class) as well as the mixing height are given on a two-dimensional grid.

1.2. Atmospheric stability

Atmospheric stability values and functions are derived using standard similarity theory profiles as given in Garratt (1992). The Monin-Obukhov length is defined as:

$$L_{MO} = -\frac{\rho c_P u_*^3 T}{kgQ_H}, \tag{1.1}$$

where Q_H and T are the sensible heat flux and air temperature at ground level $u_*$is the friction velocity, ρ the air density, c_P the specific heat at constant pressure, $k = 0.4$ the von Karman constant. The sign of L_{MO} is consistent with Q_H: if the flux is directed away from the surface (positive) it gives unstable conditions ($L_{MO} < 0$), while when it is directed toward the ground (negative), it is associated with stable conditions ($L_{MO} > 0$).

A physical description of L_{MO} can be given as follows:

- in unstable conditions, $-L_{MO}$ is the distance from the ground above which convective turbulence is more important than mechanical shear stress due to friction at the surface;
- in stable conditions, L_{MO} is the height above which the vertical turbulent motion is strongly inhibited due to stable stratification.

1.2.1. Stability functions in the surface layer

In the surface layer turbulent fluxes can be expressed using Monin-Obukhov similarity theory: vertical fluxes of momentum, heat and moisture are assumed to be proportional to universal functions of the stability parameter

$$\zeta = \frac{z}{L_{MO}}, \tag{1.2}$$

z being any reference height. These vertical fluxes display an almost similar structure; in the following, only the expression for momentum will be used, as passive dispersion refers to mass transfer processes. The wind speed vertical profile is related to stability (Dyer and Hicks, 1970; Dyer, 1974) through the following equation:

$$\frac{kz}{u_*}\frac{\partial U}{\partial z} = \Phi\left(\frac{z}{L_{MO}}\right). \tag{1.3}$$

The gradient function Φ is defined as a piecewise continuous function, which depends on stability (Dyer and Hicks, 1970):

$$\Phi = \begin{cases} (1-16\zeta)^{-1/4} & \zeta < 0 \\ 1 & \zeta = 0 \\ 1+5\zeta & \zeta > 0. \end{cases} \tag{1.4}$$

Similar functions, with a small variation in the value of coefficients, are suggested by many authors, e.g . Businger (1973); Panofsky and Dutton (1984); Businger (1988); Hogstrom (1988); Holtslag and Moeng (1991); Trombetti and Tagliazucca (1994).

Assuming the principle of a no-slip interface, the vertical momentum flux can be obtained as the product of the free wind above the ABL (the geostrophic wind) and the frictional drag of the earth's surface (the roughness length). The shape of the velocity profile changes with the stability of the atmosphere, i.e. the effect of free convection. For neutral stability (i.e. no free convection, forced convection only) the actual wind speed may be calculated from the usual logarithmic profile:

$$\frac{kz}{u_*}\frac{\partial U}{\partial z} = 1. \tag{1.5}$$

Another function, the stability profile function Ψ, is also often used in stability-related equations; it is derived from the gradient function Φ using the following relationship (e.g. Businger, 1988):

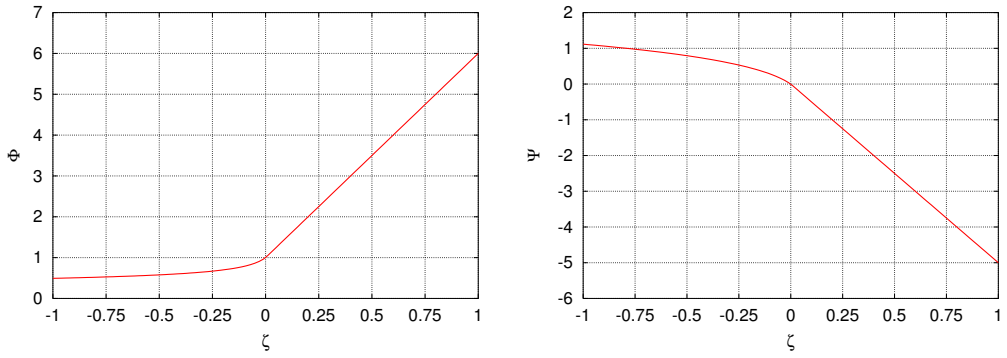

Figure 1.2.: The dimensionless functions Φ and Ψ.

$$\Phi = 1 - \zeta \frac{\partial \Psi_m}{\partial \zeta}. \tag{1.6}$$

The form of both functions Φ and Ψ is reported in figure 1.2.

The integral forms of the similarity functions for momentum flux can be detailed through (1.6) in the form (Paulson, 1970):

$$\Psi = \begin{cases} \ln \frac{(1+\eta)^2(1+\eta^2)}{8} + 2\left[\frac{\pi}{4} - \arctan(\eta)\right] & \zeta < 0 \\ 1 & \zeta = 0 \\ -5\zeta & \zeta > 0 \end{cases}, \tag{1.7}$$

where

$$\eta = (1 - 16\zeta)^{\frac{1}{4}}. \tag{1.8}$$

These closures are often used above the surface layer, although, at least for unstable situations, these profiles have been deduced only for the surface layer (Dyer, 1974; Hogstrom, 1988). However, many dispersion models make use of this approximation. This is acceptable only in the case of ground-based sources, which produce a maximum concentration close to the emission and imply a reduced mass transfer above the surface layer height. In any case some corrections have been proposed to account for diffusion in the outer layer (see section 1.4.2)

For convective situations not only the friction velocity is needed to characterize the turbulent flow, but also the vertical convective velocity scale, denoted as w_* and defined

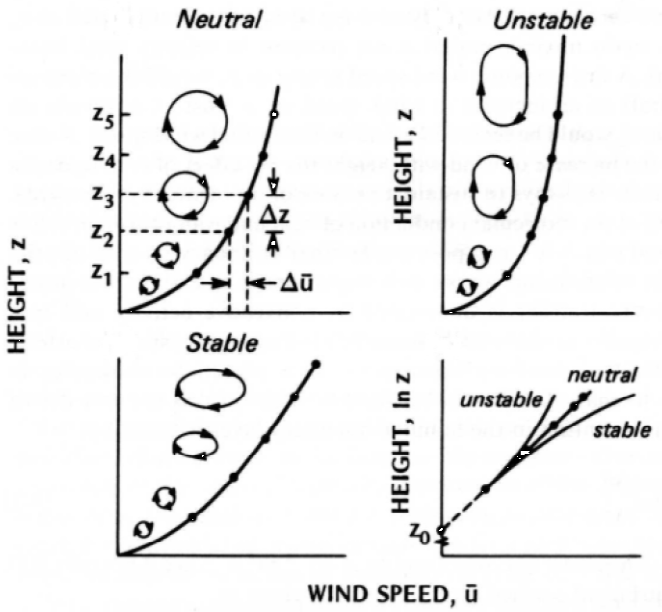

Figure 1.3.: Wind profile modification due to stability (Thom, 1975).

as

$$w_* = \left(\frac{z_i g Q_H}{T} \right)^{\frac{1}{3}}, \tag{1.9}$$

where z_i is a length scale representing the boundary layer depth, whose order of magnitude is around $1000\,m$. w_* is the velocity scale of an air parcel being lifted from the ground to the top of the boundary layer and vice versa, inside a vertical thermal circulation. Monin-Obukhov length L_{MO} and friction velocity u_* are usually computed iteratively, using two coupled equations, according to the procedure reported in section 2.2.2.5 (Panofsky and Dutton, 1984).

Under unstable conditions, the shape of the profile changes because the shape of the eddies is stretched. On the contrary, under stable condition, the eddies are compacted as shown in figure 1.3.

Integrating equation 1.3 we obtain

$$U(z) = \frac{u_*}{k} \left[\ln \left(\frac{z}{z_0} \right) - \Psi \left(\frac{z}{L_{MO}} \right) + \Psi \left(\frac{z_0}{L_{MO}} \right) \right]. \tag{1.10}$$

Once L_{MO} and u_* are computed with respect to the speed measurement $U(z_1)$ at height z_1, the vertical profile may be derived through the relationship

$$U(z) = U(z_1)\frac{\ln\left(\frac{z}{z_0}\right) - \Psi\left(\frac{z}{L_{MO}}\right)}{\ln\left(\frac{z_1}{z_0}\right) - \Psi\left(\frac{z_1}{L_{MO}}\right)}, \tag{1.11}$$

where the last term $\Psi\left(\frac{z_0}{L_{MO}}\right)$ is omitted because it is negligible.

1.2.2. Stability over the entire ABL

In some models the effect of stability is included, instead of using the dimensionless variable $\zeta = z/L_{MO}$, through the constant value h/L_{MO}, where h is the boundary layer depth. An example is given in the ADMS User's Guide, released by CERC (Apsley et al., 2000). In terms of this parameter, stability is defined as:

$$\begin{cases} h/L_{MO} > 1 & unstable, \\ -0.3 \leq h/L_{MO} \leq 1 & neutral, \\ h/L_{MO} < -0.3 & stable. \end{cases} \tag{1.12}$$

Table 1.2.: Examples of the relationship between the stability criterion based on equation 1.12 and Pasquill-Gifford stability classes.

$U\,[m/s]$	$L_{MO}[m]$	$h\,[m]$	$h/L_{MO}[-]$	$P-G$ class
1	-2	1300	-650	A
2	-10	900	-90	B
5	-100	850	-8.5	C
5	∞	800	0	D
3	100	400	4	E
2	20	100	5	F
1	5	100	20	G

Examples of the correspondence between the above stability criterion and that based on classical Pasquill-Gifford ranges are given in table 1.2.

1.3. Air pollution modelling

1.3.1. Mathematical formulation

The partial differential equation describing the dispersion process of passive tracers reads:

$$\frac{\partial C}{\partial t} + \mathrm{u} \cdot \nabla C = \nabla \cdot (\mathrm{K} \cdot \nabla C) + \dot{S}, \tag{1.13}$$

where C is the concentration, u is the flow field, K is a tensor (in general diagonal) which denotes turbulent diffusivity, and $\dot{S}$ represents the source (or sink) term. It should here be remembered that C in (1.13) is indeed an average concentration; furthermore, turbulent fluctuations are represented through Fick's law:

$$\left\langle \mathrm{u}' C' \right\rangle = -\mathrm{K} \cdot \nabla C. \tag{1.14}$$

The values of turbulent diffusivity are required for solving equation 1.13. In particular, the vertical eddy diffusivity profile $K_z(z)$ is needed or, equivalently (when a lagrangian viewpoint is adopted), vertical profile of velocity variance σ_W^2 .

Horizontal diffusivity $K_x(z)$ and $K_y(z)$ are generally given as a linear function of $K_z(z)$; they are typically of the same order of magnitude and their effect is often negligible, at least in long range transport, since the advection terms $u\frac{\partial C}{\partial x}$ and $v\frac{\partial C}{\partial y}$ are typically larger than diffusion terms. This is not the case for the vertical term, since vertical velocity is typically quite small and hence convective transport is comparable to diffusive transport.

The importance of the estimate of $K_{x,y,z}$ is related to the fact that this quantity can vary over several orders of magnitude within the ABL; hence, its variation in equation 1.13 may dramatically affect results in terms of concentration.

The turbulent velocity variances, namely $\sigma_{U,V,W}$ are related to eddy diffusivity through the relationship

$$K_{x,y,z} = T_L \sigma_{U,V,W}, \tag{1.15}$$

where T_L is the lagrangian time scale, which will be further discussed in section 3.1.3. The lagrangian time scale is expected to be larger over complex terrain, in particular inside a valley, than in a stable boundary layer over flat, uniform terrain because the size of the energy containing eddies in the lateral direction is usually larger in complex terrain (Luhar and Rao, 1994). The following estimate, $\sigma_{U,V} \simeq c_1 \sigma_W$, with $c_1 \simeq 1$ is often assumed; for example Tinarelli et al. (1994) report a value of 0.85 in the surface layer and 1.55 above.

1.3.2. Lagrangian and Eulerian timescale

The knowledge about correlation between the eulerian time scale (examples are given in table 1.1) and the lagrangian one is required when approaching diffusion problems by

means of lagrangian schemes, as it will be done in chapter 3. Pasquill and Smith (1983) use the relationship

$$\frac{T_L}{T_E} = a\frac{W}{\sigma_W}, \tag{1.16}$$

where W is the mean vertical velocity and σ_W represents the standard deviation of velocity (the expression is indeed valid also for the other component of the velocity). The factor a is an empirical constant, which ranges between 0.35 and 0.8, depending on the context (Pasquill and Smith, 1983); also theoretically estimate and experimental verification through wind tunnel data by Koeltzsch (1999) suggest a value equal to about 0.8.

The eulerian integral time scale should be determined through a space correlation; it is however often computed using time correlation, adopting Taylor's hypothesis of "frozen turbulence", which is not always true; anyway, in this case, there is no difference between these two correlation functions. Being both the lagrangian and eulerian time scales determined in the same flow field, they should in some way be related, except in the near field. The lagrangian length scale L_L can be determined experimentally by dispersion measurements, or using the relationship $L_L = \sigma_W T_L$, while the eulerian scale is given by

$$L_E = \frac{T_E W}{\sqrt{1 + \frac{\sigma_W^2}{W^2}}}. \tag{1.17}$$

In this case Taylor's restriction is no more necessary (Koeltzsch, 1999). The ratio of both time scales may be interpreted as a function of the turbulence intensity and depends on the stability of the atmosphere as well.

1.3.3. Phenomenology

Meteorological factors influencing pollutant dispersion are wind speed and direction and vertical temperature gradient (i.e. air stability or eddy diffusivity). The presence of thermal inversion decreases air quality as it inhibits the mixing of the pollutant in the layers above of the inversion, reducing the extent of the domain over which the dilution process can act. From the phenomenological point of view some cases may be distinguished, as shown in figure 1.4.

Classification with respect to source geometry is divided in: isolated sources (e.g. stacks), line sources (typically roads) and area sources (e.g. waste dumps). On the other hand emission type may be roughly divided into instant release and continuous release. An instant release is represented by an emission (gas or particles) which is restricted in time,

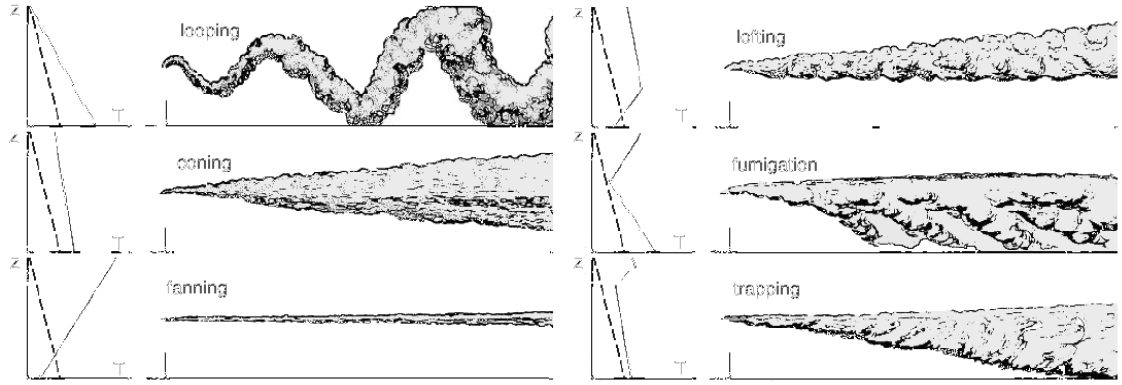

Figure 1.4.: Behaviour of the effluent depending on the vertical temperature gradient; the dashed line represents the adiabatic temperature profile (adapted from Santomauro, 1975).

for example emergency releases or incidents. On the contrary, continuous sources are commonly encountered in human activities (e.g. domestic heating, industrial emissions, urban traffic).

1.4. Eddy diffusivity

1.4.1. Estimate of eddy diffusivity in the surface layer

As introduced above, inside the surface layer mass exchange is based on local similarity (e.g. Nieuwstadt, 1984); vertical turbulent diffusivity is defined as

$$K_z = l_m^2 \left| \frac{\partial U}{\partial z} \right|, \tag{1.18}$$

where $l_m = kz$ is the mixing length scale, and the vertical speed gradient is given by equation 1.3. Therefore (1.18) yields:

$$K_z(z) = \frac{k u_* z}{\Phi\left(\frac{z}{L_{MO}}\right)} \tag{1.19}$$

In order to account for turbulence length scale difference in the boundary and in the outer layer, a modified mixing length, as introduced by Blackadar (1962), can be used. In fact, the mixing length $l_m = kz$ used in the surface layer is extended to the outer layer

introducing an asymptotic length scale $\lambda_m\beta$, thus yielding:

$$\frac{1}{l_m} = \frac{1}{kz} + \frac{1}{\lambda_m\beta} \tag{1.20}$$

The underlying idea is that the vertical extent of the boundary layer limits the turbulence scale. λ_m has a typical value ranging $100 \div 200\,m$, while the parameter β is equal to 1 in the boundary layer and decrease in the free atmosphere; the following expression is used

$$\beta = \beta_0 + \frac{1-\beta_0}{1+\left(\frac{z}{H_b}\right)^2}, \tag{1.21}$$

with $\beta_0 = 0.2$ and $H_b = 4000\,m$.

1.4.2. Extension to the atmospheric boundary layer

Under unstable surface conditions exchange coefficients can be expressed as integral profiles for the entire convective mixed layer, multiplying (1.19) by a scaling factor related to z_i. This formulation is proposed by Troen and Mahrt (1986) and leads to the following expression:

$$K_z(z) = \frac{kzu_*}{\Phi\left(\frac{z}{L_{MO}}\right)}\left(1-\frac{z}{z_i}\right)^2. \tag{1.22}$$

1.4.2.1. Non-local transport

The term $\left(1-\frac{z}{z_i}\right)^2$ in equation 1.22 accounts for the so-called "non-local" transport by convective turbulence. In (1.19) the turbulent flux is proportional to the local gradient. This is a reasonable assumption when the length scale of the largest turbulent eddies is smaller than the size of the domain over which turbulence spans. In the boundary layer this is typically true for neutral and stable conditions, while for the unstable case the mixing layer may be larger than the largest transporting eddies and the flux can show a counter-gradient behaviour (Deardorff, 1972; Holtslag and Moeng, 1991). In other words, the flux $\overline{w'C'}$ is no longer equal to $-K_z\frac{\partial C}{\partial z}$ but takes the following form:

$$\overline{w'C'} = -K_z\left(\frac{\partial C}{\partial z} - \gamma_c\right), \tag{1.23}$$

where γ_c represents the counter-gradient "non-local" transport. For stable and neutral conditions γ_c is negligible and can be safely set to 0. However, in the "non-local" diffusion

scheme equation 1.22 can be cast in the general form:

$$K_z(z) = \frac{kzw_{turb}}{\Phi\left(\frac{z}{L_{MO}}\right)}\left(1-\frac{z}{h}\right)^2, \tag{1.24}$$

which is valid for any stability class. In (1.24) h is the depth over which turbulent transport extends ($=z_i$ in a convective mixed layer); w_{turb} is a characteristic turbulent velocity scale, which is computed as $w_{turb} = u_*$ for stable and neutral conditions and $w_{turb} = \left(u_*^3 + 0.6w_*^3\right)^{1/3}$ under unstable conditions. It should be noted that in very convective atmosphere w_{turb} has the same order of magnitude of w_* as deduced by Troen and Mahrt (1986).

Alternatively, if the turbulent diffusivity coefficients are calculated on the basis of global stability, the ABL height is then calculated using the method which will be discussed in section 2.1. For stable situations these values are retained. For unstable situations, new values are calculated for layers below the mixing height using the O'Brien (1970) profile:

$$\begin{aligned} K_z(z) &= K_z(z_i) + \left(\frac{z_i - z}{z_i - h_s}\right) \\ &\cdot \left\{K_z(h_s) - K_z(z_i) + (z-h_s)\left[\left.\frac{\delta K_z}{\delta z}\right|_{z=h_s} + 2\frac{K_z(h_s) - K_z(z_i)}{z_i - h_s}\right]\right\} \end{aligned} \tag{1.25}$$

in which z_i is the mixing height and h_s is the height of the surface boundary layer (or the so-called constant flux layer). In models h_s is typically set to $0.1z_i$ (see, e.g. Stull, 1988; Garratt, 1992).

1.4.2.2. Unstable boundary layer

A small value of turbulent diffusivity, typically $K_z = 10^{-3}$, is adopted for the free troposphere, above the ABL, and also within the stable layer. Being this value reduced of $3 \div 4$ order of magnitudes with respect to a well-mixed convective layer, it practically corresponds to a superior limit confining diffusion processes below.

1.4.2.3. Power law form

An alternative formulation for the vertical profile of turbulent diffusivity, which is used in many dispersion models, is the power law form reported ,for example, by Panofsky and Dutton (1984):

$$K_z(z) = K_{z,m}\left(\frac{z}{z_m}\right)^n. \tag{1.26}$$

Notice, however, that equation 1.26 also relies on similarity functions for the estimate of the value $K_{z,m}$ at the measurement height z_m:

$$K_{z,m}(z) = k^2 \frac{z_m U_m(z)}{G(\zeta)\cdot\phi(\zeta)}, \tag{1.27}$$

where the function G is defined as:

$$G = \begin{cases} \ln\left[\frac{(\eta_m-1)(\eta_0+1)}{(\eta_m+1)(\eta_0-1)}\right] + 2\left[\arctan(\eta_m) - \arctan(\eta_0)\right] & \zeta < 0 \\ \ln\left(\frac{\zeta_m}{\zeta_0}\right) & \zeta = 0 \\ \ln\left(\frac{\zeta_m}{\zeta_0}\right) + 5\zeta_m & \zeta > 0 \end{cases} \tag{1.28}$$

and η has the same definition given by (1.8); the subscript m refers to measurement height, while subscript 0 denotes the roughness length. Exponent n in equation 1.26 depends on stability and is given through tables (Panofsky and Dutton, 1984). Finally, it is worth noticing that equation 1.2 seems not to be suitable especially for complex terrain because it doesn't account for a correction term for the varying boundary layer depth.

2. Computing eddy diffusivity in valleys

2.1. The global approach

The introduction of turbulent parameterizations through a global approach implies the use of average quantities integrated over the domain (or over part of it). The above procedure is meant to simulate the evolution of the vertical profile of eddy diffusivity in a valley during a diurnal cycle, starting at sunrise. After the sun begins heating the valley, energy is transmitted to the surface layer. The thermal instability determines convective motion on a depth which gradually increases, until energy is provided. As a consequence, the ground based inversion, which normally establishes during night-time, is destroyed and the entire boundary layer up to the inversion top is well mixed, roughly, at noon. An upslope flow on the sidewalls arises determining the subsidence of the stable core of colder (and therefore heavier) air at the center of the valley.

During the morning, the stable core is gradually destroyed starting from the bottom (individuated by the height of the CBL, convective boundary layer) until it disappears at the so called "break-point" time (see figure 2.1). This condition of well mixed atmosphere corresponds to a constant vertical profile of potential temperature (see also figure 2.2), which is defined as

$$\theta = T \left(\frac{p_0}{p} \right)^{R/c_p}, \tag{2.1}$$

where T is the temperature, p the pressure and p_0 the reference pressure at sea level; the ratio between R (gas constant) and c_P (specific heat at constant pressure) has a value of 0.287 for dry air.

At the same time, the inversion top (IT), which represents the superior limit of the nocturnal stable layer, gradually descends. Both processes are fed by the solar forcing which is in turn affected by orographic factors in its turn. The importance of the estimate of the depth of the CBL is related to the fact that within this layer the dispersion of ground based pollutant sources is mainly confined, while it is inhibited in the upper layers. At sunset the solar forcing ceases and a stable boundary layer develops starting from the

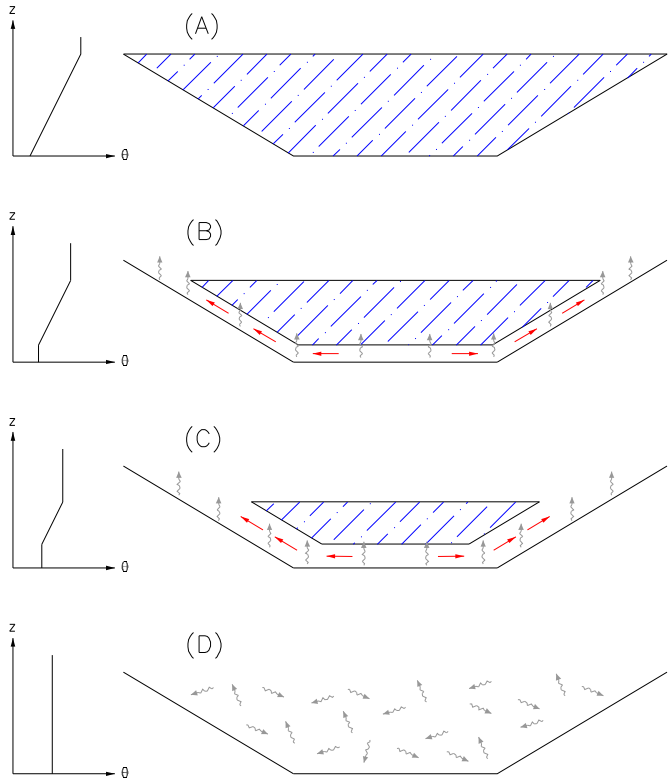

Figure 2.1.: Removal of the nocturnal stable layer (Whiteman, 1982). a) At sunrise the thermal inversion over the depth of the valley determines a situation of stable atmosphere; b) with the heating of the valley floor the growth of the CBL starts; c) the stable core sinks and upslope flows arise (secondary circulation); d) the well-mixed situation is reached around noon time.

ground, leaving a residual layer above which gradually disappears through the transfer of energy to the layers below.

The above processes are schematized in the present work building upon the procedure adopted in VALDRIFT model (Allwine et al., 1996): this is a streamtube three-dimensional atmospheric transport and dispersion model which can be used in well-defined compact, regular (trapezoidal) and fairly straight mountain valleys. The model is phenomenological, that is the dominant meteorological processes governing the behaviour of the valley atmosphere are formulated explicitly in the model. Of course, computing a quantity as an average over a section (or equivalently over a volume), doesn't allow one to account for the spatial variations of the variables, which may be relevant, especially over complex

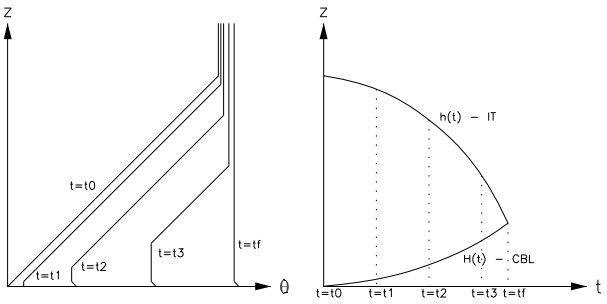

Figure 2.2.: Qualitative evolution of a) potential temperature and b) CBL and IT.

terrain; however, a global approach is suitable for models working on large scales or in case fine-grained input are not available.

Required inputs for a streamtube model are the valley geometric characteristics, the release rate as a function of time and space, the along-valley wind speed as a function of time, and the sensible heat flux or, alternatively, as in VALDRIFT, the eddy diffusivity. A streamtube model defines the tubes with a geometrical criterion (see figure 2.12): the ratio between the surface of a cell (in the crosswind direction) and the whole valley section Ω_{tot} is constant at each cross-section of the valley:

$$\frac{\Omega_{jk}}{\Omega_{tot}} = constant, \tag{2.2}$$

where subscripts j and k are denote the cross-valley and vertical direction, respectively. Also notice that streamtubes don't exchange flow in the crosswind direction but only mass due to turbulent diffusion.

The outputs of the model are the pollutant concentrations and the deposition fields as a function of time and space. The dynamical part of the model will not be further discussed here, while the thermodynamic scheme used in VALDRIFT will be extended to the case of a valley of any geometric form; this will allow us to use a global approach (i.e. integrated over the section) not only for the development of the CBL height, but also for the determination of the eddy diffusivity vertical profile. It is worth noticing that the present formulation for the computation of the vertical profile of K_z, which is proposed in section 2.1.1, overrides the limitations embodied in the original version of the procedure, where it is acquired to provide the eddy diffusivity as a piecewise constant function.

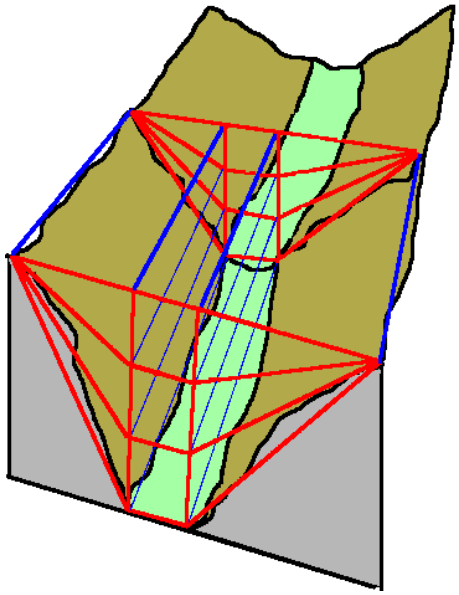

Figure 2.3.: Streamtubes scheme.

2.1.1. Day time

As a first step the evolution of the daily cycle of CBL and IT, averaged over a section of a valley, is simulated, as explained in section 2.1. According to Allwine et al. (1996), the variation of sensible heat flux can be written in the form:

$$\frac{dQ_H}{dt} = E(t)A_0 b(z), \tag{2.3}$$

where $E\,[W/m^2]$ is the solar radiation entering the atmosphere, A_0 the fraction of E which increases the air temperature in the valley, thus modifying the stratification, and $b(z)$ the width of the valley (at height z) which is crossed by the flux F. The structure of $E(t)$ is typically represented through a sinusoidal function:

$$E(t) = E_0 \sin\left[\frac{\pi}{\tau}(t - t_i)\right], \tag{2.4}$$

where $\tau\,[s]$ is the period spanning about half a day (from sunrise to sunset).

The sensible heat per unit length of the valley $Q_H\,[J/m]$ is the sum of two parts, namely Q_{IT}, which is responsible for the decrease of the IT, and Q_{CBL}, which causes the CBL depth to increase. An estimate of A_0 can be obtained through a quite simple heat balance (see the brief description in section 2.1.1.2), for instance by applying the thermodynamic

model of Whiteman and McKee (1982).

2.1.1.1. Geometric considerations

Let's consider a section of any form, limited at its top by an horizontal line at height ς from the valley floor.

The vertical coordinate of the barycenter is defined as:

$$\eta_G(\varsigma) = \varsigma - \frac{1}{\Omega(\varsigma)} \int_0^{\varsigma} \int_0^{b(z)} dy\, z\, dz, \tag{2.5}$$

where $\Omega(\varsigma)$ is the cross sectional area

$$\Omega(\varsigma) = \int_0^{\varsigma} \int_0^{b(z)} dy\, dz. \tag{2.6}$$

Furthermore, the function $M(\varsigma)$ is defined as:

$$M(\varsigma) = \Omega(\varsigma)\eta_G(\varsigma). \tag{2.7}$$

We then assume that the fractions of Q_H, which may induce a change of the height of CBL (H_C) and IT (H_I), are proportional to the width of the valley at the height at which the two layers are positioned at a given time t:

$$\frac{dQ_{CBL}}{dt} = f\left(H_C\right), \tag{2.8}$$

$$\frac{dQ_{IT}}{dt} = f\left(H_I\right). \tag{2.9}$$

Recalling the first law of thermodynamics $dQ = \rho c_p \frac{T}{\theta} d\theta$, the exchanged heat within the section per unit length, at the height of CBL, can be given the following form:

$$\begin{aligned} Q_{CBL}(\varsigma) &= c_0 \gamma_\theta \int_0^{\varsigma} \int_0^{b(z)} \gamma_\theta(\varsigma - z) dy dz \\ &= c_0 \gamma_\theta M(\varsigma), \end{aligned} \tag{2.10}$$

where the differential of potential temperature $d\theta$ is substituted by $\gamma_\theta dz$, $\gamma_\theta\,[K/m]$ being the vertical gradient of potential temperature when the removal of stable layer starts, i.e. at sunrise. Furthermore we set $c_0 = \frac{\rho c_p T}{\theta}$: the above ratio is nearly constant in vertical direction and its value is about $1100 \div 1200\, J/(m^3 K)$.

Rewriting equation 2.8 for the CBL ($\varsigma = H_C$), the variation of H_C is related to the variation of Q_{CBL} in the following form:

$$\begin{aligned} \frac{dQ_{CBL}}{dt} &= \frac{dQ_{CBL}}{dH_C}\frac{dH_C}{dt} \\ &= c_0\gamma_\theta \frac{dM}{dH_C}\frac{dH_C}{dt} = c_0\gamma_\theta \Omega\left(H_C\right)\frac{dH_C}{dt}. \end{aligned} \tag{2.11}$$

For the IT ($\varsigma = H_I$) a similar equation can be derived:

$$\frac{dQ_{IT}}{dt} = \frac{dQ_{IT}}{dH_I}\frac{dH_I}{dt} = c_0\gamma_\theta \frac{dM}{dH_I}\frac{dH_I}{dt} = c_0\gamma_\theta \Omega\left(H_I\right)\frac{dH_I}{dt}. \tag{2.12}$$

We then assume that the fraction of Q_S feeding the variation of CBL and IT is proportional to ratio of the width of the section at height H_I and H_C, respectively:

$$\frac{dQ_{CBL}}{dt} = \frac{dQ_H}{dt} f_c \frac{b\left(H_C\right)}{b\left(H_I\right)}, \tag{2.13}$$

$$\frac{dQ_{IT}}{dt} = \frac{dQ_H}{dt}\left[1 - f_c\frac{b\left(H_C\right)}{b\left(H_I\right)}\right], \tag{2.14}$$

where f_c is an empirical constant falling in the range $0 \div 1$, which has been introduced by Allwine et al. (1996) for the partition of the energy flux, in order to decouple equations 2.11 and 2.12.

The initial conditions are written as:

$$\begin{cases} H_C|_{t=0} = H_{C0} > 0 \\ H_I|_{t=0} = H_{I0} > H_{C0} \end{cases}, \tag{2.15}$$

where H_{I0} is the height over the valley floor of nocturnal stable layer before sunrise (equation 2.11). When no additional information is available, its upper limit is conventionally set at the height of the mountains ridges (provided their elevation is not too high, otherwise H_{I0} is set to a lower value). In any case, synoptic flow field over the mountain ridges is supposed not to interfere with the valley circulation, nor with the heat balance.

Equations 2.13 and 2.14 include different scenarios in the evolution of $H_I(t)$ and $H_C(t)$ according to the values attained by three parameters: the partitioning constant f_c, the width of the valley floor L, and the average inclination of the sidewalls; results are illustrated in figures 2.4, 2.5 and 2.6.

Partitioning of incident radiation is related to the valley geometry: “closed” valleys (i.e.

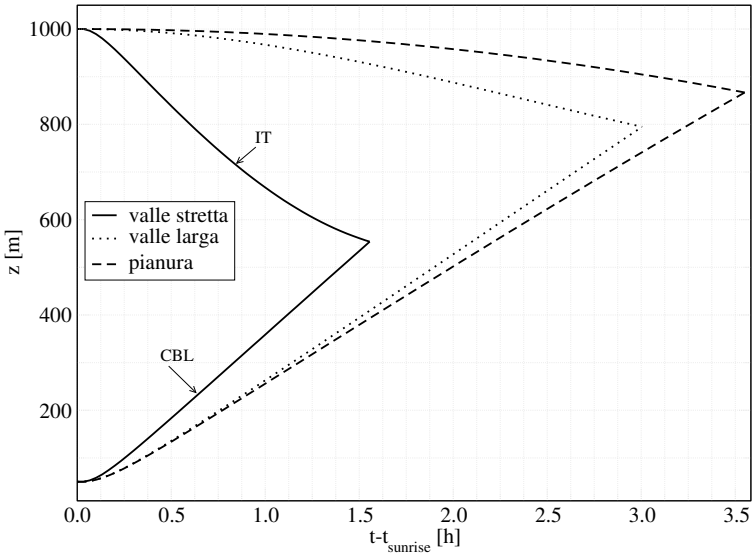

Figure 2.4.: CBL growth and IT decrease with different valley floor widths and $f_c = 0.75$.

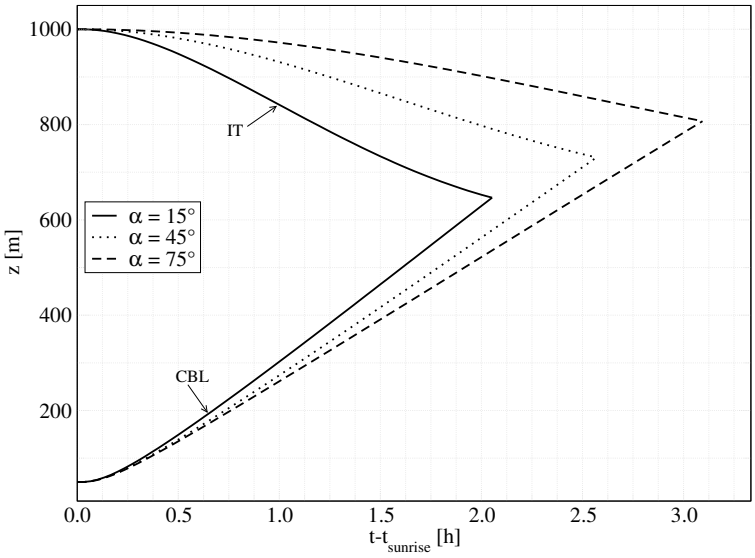

Figure 2.5.: CBL growth and IT decrease with different side slope inclination, $f_c = 0.75$ and valley floor width $L = 1000\,m$.

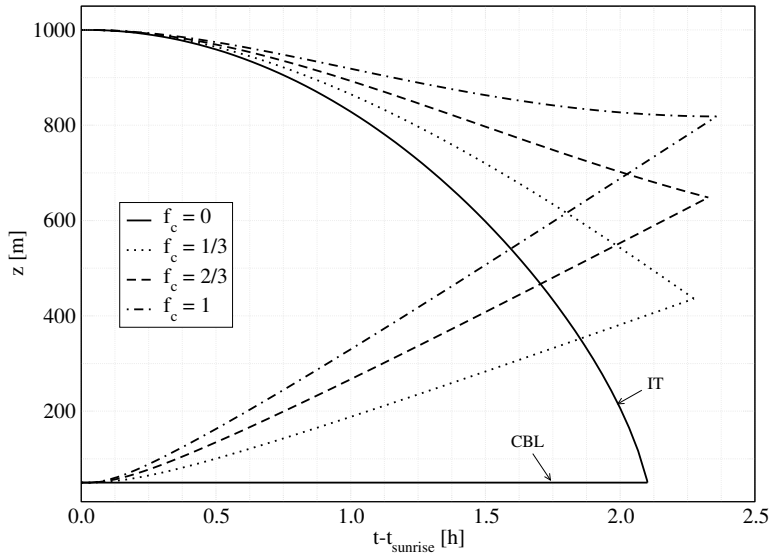

Figure 2.6.: CBL growth and IT decrease with different energy partitioning coefficient, valley floor width $L = 1000\,m$ and side slope inclination $\alpha = 30°$.

with nearly vertical slopes) show a ratio $\frac{b(H_C)}{b(H_I)} \to 1$; as a consequence the heat flux mainly feeds the CBL; on the contrary in "open" valleys (i.e. with low slope inclination) the core subsidence is more evident, because upslope flow are in this case enhanced. In a very large valley, or in the limit case of flat uniform terrain ($L \to \infty$), energy almost feeds the CBL development, leaving the IT nearly at the initial height. Moreover, the increase of L and tends to delay the "break-point" time, at which the stable core is completely removed. Finally, as one can readily deduce from equations, the lower is H_I, the quicker the "break-point" time is reached.

Some tests were performed on the Adige Valley, in the neighbourhood of Trento (further details on the location are given in section 1.2.1). From a rough analysis of the vertical temperature profile, reported in Rampanelli (2004), for this study area a value of $f_c = 0.75$ is obtained and adopted in the present work.

As the other parameters is concerned, we can observe that an increase of solar radiation obviously reduces the time required to reach the "break-point", while an increase of the thermal gradient γ_θ has an opposite effect.

At this point, substituting equations 2.3 and 2.11 in 2.13 we obtain the following expression:

$$\frac{dH}{dt} = \frac{A_0 E(t)}{c_0 \gamma_\theta} f_c \frac{b\left(H_C\right)}{\Omega\left(H_C\right)}. \tag{2.16}$$

Similarly, substituting equations 2.3 and 2.12 into (2.14), the equation governing the evaluation of the CBL takes the following form:

$$\frac{dh}{dt} = \frac{A_0 E(t)}{c_0 \gamma_\theta} \left[b\left(H_I\right) - f_c \frac{b\left(H_C\right)}{\Omega\left(H_I\right)} \right]. \tag{2.17}$$

2.1.1.2. Heat balance

An estimate of the fraction A_0 of the solar radiation which increases the air temperature can be obtained through to a thermal balance. The net energy flux Q_* in the air layer close to the ground, due to solar incident radiation, can be divided in two contributions: the first, K_*, is due to short wave radiation, and the second, L_*, is due to long wave radiation.

In turn, these contributes can be separated into ingoing and outgoing fluxes, as follows:

$$K_* = K\uparrow + K\downarrow, \tag{2.18}$$

$$L_* = L\uparrow + L\downarrow, \tag{2.19}$$

where $K\downarrow$ is representative of nearly the totality of solar incident radiation and can be again divided in direct and diffused radiation. A part of the incident radiation is reflected and is indicated by $K\uparrow$, so that $K\uparrow = -aK\downarrow$, where a is the albedo of the ground and $K_* = (1-a)K\downarrow$. In the same way, long waves, where the infrared band L_I covers the large part of energy ($L_* \simeq L_I$), are identified by the radiation flux $L\uparrow$ outgoing from the earth's surface. In fact $L\downarrow$ can be neglected since it is typically much lower than the incident short wave flux, such that $L_I \simeq L\uparrow$.

During night-time the solar irradiation vanishes, while L_* is important and, depending on the ground cooling, it may tend to sign reverse. The term $L\downarrow$ represents the heat release from the ground to the close atmosphere, through irradiation.

We then obtain (Sozzi et al., 2002):

$$\begin{aligned} Q_* &= K_* + L_* \\ &= (K\uparrow + K\downarrow) + (L\uparrow + L\downarrow) \\ &\simeq (-aK\downarrow + K\downarrow) + L\uparrow \\ &\simeq (1-a)K\downarrow + L_I, \end{aligned} \tag{2.20}$$

where $L\uparrow$ has been replaced by L_I. In the above equations negative values indicate fluxes outgoing from the earth's surface, while positive values indicate ingoing fluxes: therefore during the day $Q_* < 0$, while during the night $Q_* > 0$.

Notice that the backward radiation by the ground, in the infrared band can be estimated as $\frac{L_I}{\rho c_p} = 0.08\, K \cdot m/s$, while it vanishes for covered sky.

The flux Q_* supplies other physical phenomena as atmospheric turbulence, evaporation and, more in general, the cooling or heating processes by convection and conduction of all the bodies adjacent to the ground.

Now, considering the heat balance of all the fluxes at the surface, we can write:

$$Q_* + Q_G + Q_E + Q_H = 0, \tag{2.21}$$

where Q_G is the storage heat flux in the ground, Q_E is the latent heat flux referred to evaporation ($Q_E < 0$) and condensation ($Q_E > 0$), Q_H is the sensible heat flux responsible for temperature variation of the atmosphere and convective processes. If the air is perfectly dry, the term Q_E is null and the term Q_G can be computed using an empirical expression, like $Q_G \simeq 0.3\, Q_H$ (Tampieri, 1997), which implies:

$$Q_H \simeq -\frac{10}{13} Q_*. \tag{2.22}$$

In the thermodynamic model developed by Whiteman and McKee (1982) A_0 is the fraction of solar radiation converted in sensible heat that contributes to the CBL development, under the hypothesis of nearly dry air, A_0 can be estimated as $\left|\frac{Q_H}{Q_*}\right|$, which attains a value of 0.77, according to the above assumptions. It is worth noticing that this value is larger with respect to that one measured by Whiteman and McKee (1982) during surveys in the Brush Creek Valley (Colorado), i.e. $A_0 \simeq 0.3$; this is probably due to the difference both in meteorological field data and in the phenomena of absorption, diffusion and atmospheric refraction.

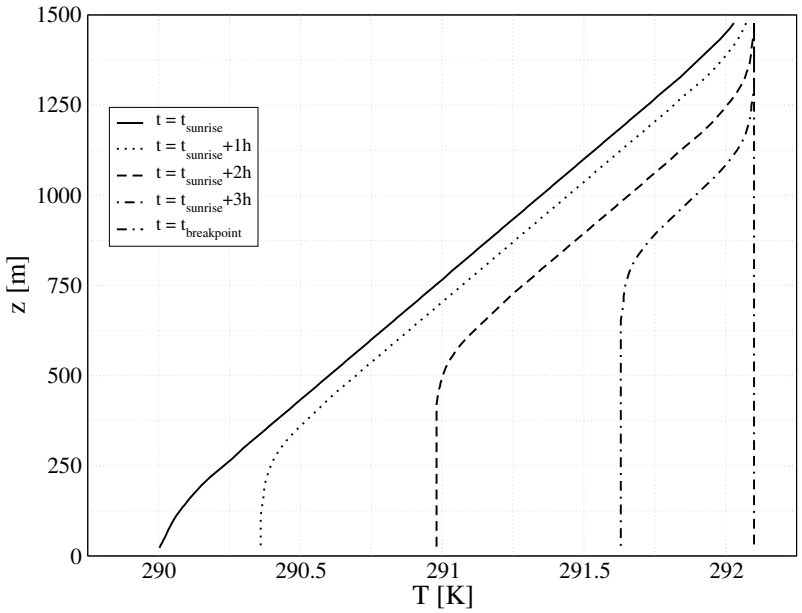

Figure 2.7.: Time evolution of potential temperature vertical profile.

2.1.1.3. Temperature and eddy diffusivity profile

Having computed the time evolution of H_C and H_I through numerical integration, we can now determine the atmospheric stability and, consequently, the turbulent diffusivity vertical profile (averaged over the width of the valley), which depend upon these two heights. In fact, following the approach adapted from Rampanelli (2004), it is possible to estimate the time evolution of potential temperature through the following expression:

$$\begin{aligned}\theta(t,z) &= \theta_{max} - \gamma_\theta \left[H_I(t) - z\right] + \gamma_\theta \left[H_C(t) - z\right] \\ &\quad -\frac{\gamma_\theta}{I} \ln\left\{2\cosh\left[I \cdot H_I(t) - I \cdot z\right]\right\} + \frac{\gamma_\theta}{I} \ln\left\{2\cosh\left[I \cdot H_C(t) - I \cdot z\right]\right\} \quad (2.23)\end{aligned}$$

where the initial condition is defined as $\theta_{max} = \theta\,|_{z=H_{I0},t=0}$ and I represents the intensity of variation (i.e. the local vertical gradient of θ) at the height $H_C$and H_I. Converting then the θ-profile (figure 2.7) to the T-profile using equation 2.1 (figure 2.8), one can apply the so called "heat budget method" which allows to compute eddy diffusivity profile (figure 2.9); for each section the expression reads (Goudsmit et al., 1997):

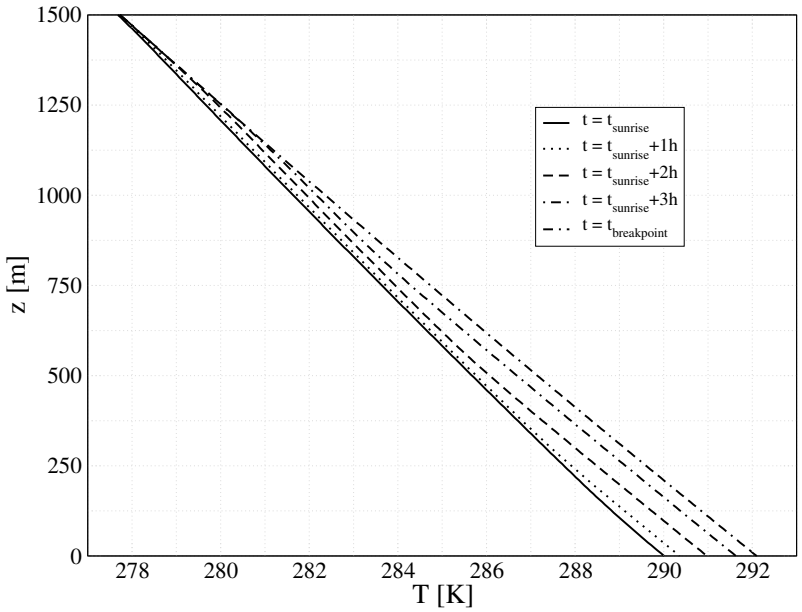

Figure 2.8.: Time evolution of temperature vertical profile.

$$K_z(t,z) = \frac{\int_0^z c_p \rho(\zeta) b(\zeta) \frac{\partial T(t,z)}{\partial t} d\zeta}{c_p \rho(z) b(z) \frac{\partial T(t,z)}{\partial z}}. \tag{2.24}$$

Implicit in this procedure is the assumption that the flux of energy crossing an horizontal plane equals the energy storage below it.

2.1.2. Night-time

During night-time a stably stratified atmosphere can be generally observed; pollutants are trapped inside the residual layer (see figure 1.1), whose height has a typical order of magnitude of $100\,m$ or less. Modelling this phenomenon is simply done by imposing an horizontal reflecting wall at that height, as in the case of day-time mixing height. In any case an inferior limit for K_z can be found using the value attained just before sunrise.

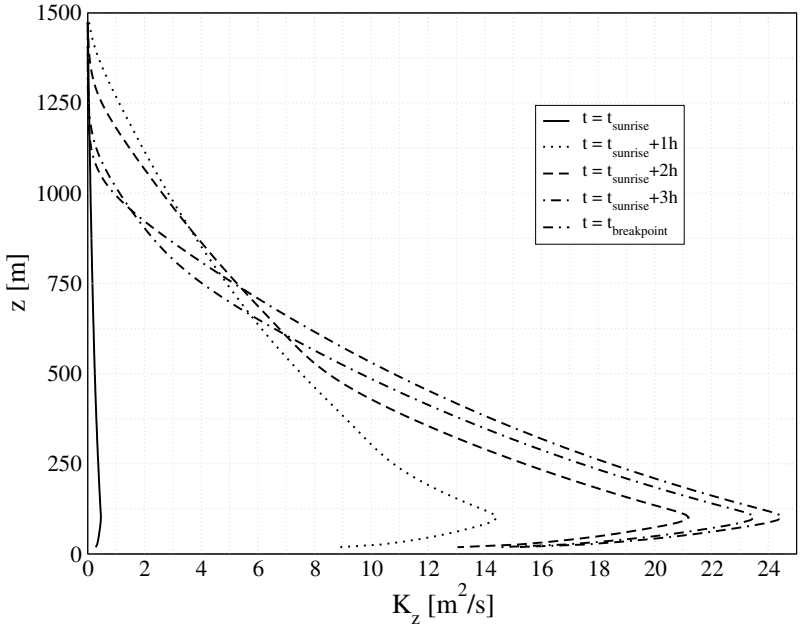

Figure 2.9.: Time evolution of eddy diffusivity vertical profile.

2.2. The local approach

An alternative method for the calculation of atmospheric turbulent diffusivity over complex terrain during day-time is presented herein, which may improve the predictions based on diagnostic meteorological models. The proposed procedure takes into account the geographic location of the area (latitude and longitude), the time of the day, the inclination and exposition of the surface, the soil type and the cloud cover. These data are used to compute the amount of solar heat flux contributing to the heating of the air mass above the ground level, and, consequently, the atmospheric turbulence. The model accounts for the effect of shadows generated by mountain profiles, which determine a differential heating at the valley floor and induce spatial and temporal variations of turbulent diffusivity. Model calibration has been performed through ground data collected during a field campaign in the Adige valley in the surrounding of the town of Trento.

2.2.1. Introduction

Diagnostic meteorological and dispersion models normally use the heat flux at ground level for the estimate of the parameters characterizing atmospheric turbulence. Calculation is performed using geographic position and time of the day, while the orographic factor is

often neglected. However, shadows generated by mountain profiles may strongly affect the heating of the air mass along the valley floor, which may differ substantially from the case of flat uniform terrain. As a consequence, secondary circulations are generated, which cannot be reproduced through diagnostic numerical model unless a suitable method for the calculation of distributed heat flux is included.

The proposed method has the aim to compute the atmospheric diffusivity over complex terrain during day-time, which accounts for the orographic factor. Two novel features are included:

- shadowed areas do not contribute to the heating of the air mass above the ground level;
- spatial variations of energy flux at ground level due to the local inclination with respect to solar beams are taken into account.

The first aspect implies that the model must be able to recognize whether each point of the terrain is shadowed by some other point of the domain, at a given date and time. To include the second effect a correction for the relative angle between the solar beams and the ground is computed at each point of the digital elevation model. As a consequence the distribution of global radiation is no more constant over the domain, but varies, at a given time, depending on the local exposition. Hence, the spatial distributions of net radiation, sensible heat flux and turbulent diffusivity change accordingly.

The surface energy balance is closed using different well known formulations in terms of local values of parameters (Holtslag and van Ulden, 1983) and taking into account the spatial variability of the relevant parameters. The model also considers that the absorption coefficient varies with the inclination of solar beams, depending upon the time of day.

Required input data for the model are:

- the digital elevation model of the area with a suitable resolution;
- land use categories or, alternatively, the distributed albedo coefficient and roughness length;
- the global radiation at ground level measured by one or more weather stations (which is required, at least, for calibration) or, alternatively, the cloud coverage.

The atmospheric parameters obtained from the model are: the atmospheric stability (Monin-Obukhov length), the friction velocity, the global radiation, the sensible heat flux

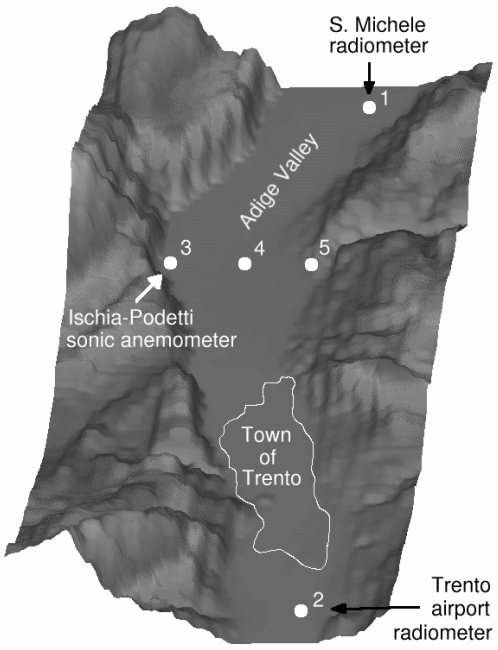

Figure 2.10.: Study area and location of measurement and test points.

and the vertical turbulent diffusivity at ground level. For the present study a height of $3\,m$ m above the ground has been adopted.

The model is tested through the inclusion of the proposed procedure within the code of CALMET, a meteorological diagnostic mass-consistent preprocessor which computes the 3D fields of wind and temperature (Scire et al., 1999). In its original formulation the code considers that mountains can influence the wind field, but not the solar radiation at ground level (and consequently the other quantities). In testing the model, the spatial and temporal variations of turbulent diffusivity are determined both with the standard procedure and including the effect of orographic factor. Calibration has been carried out by comparing the values estimated through the described procedure with those obtained with a sonic anemometer during a field campaign.

The study area is a part of the Adige Valley in the surrounding of the town of Trento (Northern Italy), characterized by an average latitude $\varphi = 46°N$ and average longitude $\lambda = 11°E$; the size of computational domain was $10 \times 20\,km$, with a cell resolution for computation of $100\,m$. The location of measurement and test sites used in present study is indicated in figure 2.10:

- 1: S. Michele (radiometer + test site),

- 2: Trento airport (radiometer + test site),
- 3: Ischia-Podetti, West side of the valley (sonic anemometer + test site),
- 4: valley center (test site),
- 5: East side of the valley (test site).

2.2.2. Formulation of the model

2.2.2.1. The solar path

The definition of shadowed regions and the computation of local aspect and inclination with respect to solar beams preliminarily requires the reconstruction of the solar path. The position of the sun is calculated in terms of a mean value of latitude/longitude of the domain, day of the year, time of the day, local aspect and inclination of the surface. The extraterrestrial radiation is written as

$$E = S_0 f \sin\gamma, \tag{2.25}$$

where a correction factor f is included which takes into account the variation of the sun-earth distance during the year due to orbit ellipticity. In (2.25) γ represents the angle between the solar beam and the local tilted surface and $S_0 = 1370\,W/m^2$ is the solar constant.

Spencer (1971) relationship is used to compute the factor f, which reads:

$$\begin{aligned} f &= 1.0011 + 0.034221\cos d_0 + 0.00128\sin d_0 \\ &\quad +0.000719\cos 2d_0 + 0.0000077\sin 2d_0, \end{aligned} \tag{2.26}$$

where

$$d_0 = \frac{360}{365}(d-1), \tag{2.27}$$

and d represents the Julian day.

In case of flat horizontal surface $\gamma = 90 - \xi$, where ξ is the zenith angle, which is given by (Iqbal, 1983):

$$\cos\xi = \sin\delta\sin\varphi + \cos\delta\cos\varphi\cos\omega, \tag{2.28}$$

where φ is the latitude, δ is the solar declination angle and ω is the so called hour angle,

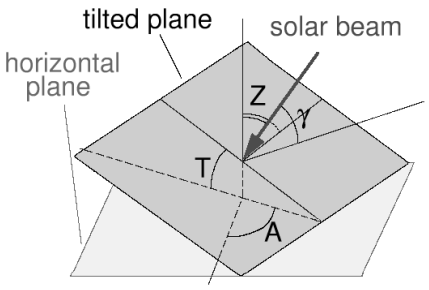

Figure 2.11.: Sketch of the defined angles and notation.

which reads:

$$\omega = \frac{180}{12}\left(t - 12 + \frac{\lambda - \lambda_{mrd}}{15}\right). \tag{2.29}$$

In equation 2.29 λ_{mrd} represents the longitude of the central meridian of the local time zone and t is time. Furthermore δ can be expressed as

$$\delta = 23.45 \sin\left[\frac{360}{365}(d - 81)\right]. \tag{2.30}$$

The correction for tilted surface is computed through the following expression (Allwine and Whiteman, 1986):

$$\begin{aligned} \sin\gamma \;=\; & \sin\delta\cos\varphi\cos\kappa\sin\upsilon - \cos\delta\sin\omega\sin\kappa\sin\upsilon \\ & + \cos\delta\cos\varphi\cos\omega\cos\upsilon + \sin\delta\sin\varphi\cos\upsilon \\ & - \cos\delta\sin\varphi\cos\omega\cos\kappa\sin\upsilon, \end{aligned} \tag{2.31}$$

where υ represents the local value of surface tilt angle ($\upsilon = 0° \rightarrow$ horizontal, $\upsilon = 90° \rightarrow$ vertical) and κ is the local surface aspect ($\kappa = 0° \rightarrow$ facing North, $\kappa = 90° \rightarrow$ facing West, $\kappa = 180° \rightarrow$ facing South, $\kappa = 270° \rightarrow$ facing East).

2.2.2.2. Shadow and sky view factor

The inclusion of the orographic factor implies the computation of local values of the sky view factor, which represents the fraction of sky visible from each point of the domain, whose value ranges between 0 (sky not visible) and 1 (the case of flat horizon on flat uniform terrain). Notice that in complex orography mountains ridges act as obstacles which cause the sky view factor to vary appreciably in space: in general, points laying inside the valleys

have a sky view factor smaller than those located on top of the mountains.

In the present model the sky view factor is locally defined as follows :

$$S_v = \frac{\int_0^{2\pi} \cos\left[\phi\left(\lambda\right)\right] d\lambda}{2\pi}, \tag{2.32}$$

where ϕ is the minimum elevation angle, measured from the horizontal plane, beyond which solar beams cannot reach the given location at the ground. It is also assumed that zones which are hidden by mountain profiles during day time are only subject to the diffuse fraction of global radiation entering the atmosphere (see below).

2.2.2.3. Global radiation

The computation of local values of global radiation requires the estimate of the clearness index K_t, which is defined as the ratio between the global radiation at the ground R_G and the extraterrestrial radiation E:

$$K_t = \frac{R_G}{E}. \tag{2.33}$$

In order to compute global radiation the procedure introduced by Erbs et al. (1981) is used. Two indexes can be defined, i_R and d_R, which represent the fraction of incident direct radiation and of diffuse radiation, respectively. They read:

$$i_R = \frac{R_I}{R_G}, \tag{2.34}$$

$$d_R = \frac{R_D}{R_G}. \tag{2.35}$$

In terms of i_R and d_R the global radiation is then written in this form:

$$R_G = R_I + R_D = R_G(i_R + d_R) = EK_t(i_R + d_R), \tag{2.36}$$

where E is the computed extraterrestrial radiation, R_I is the incident direct radiation and R_D the diffuse radiation.

Equation 2.36 is valid in case of flat uniform terrain. Under this condition the value of K_t can be estimated through (2.36), in terms of the measured value of the global radiation

R_G at a given site, according to Erbs et al. (1981) formulation:

$$i_R = 1 - \frac{p}{\cos\xi}, \tag{2.37}$$

$$d_R = \frac{p}{\cos\xi}, \tag{2.38}$$

where ξ is the zenith angle. The coefficient p depends on the clearness index K_t according to the following expressions:

$$\begin{cases} p = 1 - 0.09K_t & K_t \leq 0.22 \\ p = 0.9511 - 0.1604K_t + 4.388K_t^2 - 16.638K_t^3 + 12.336K_t^4 & 0.22 < K_t < 0.80 \\ p = 0.165 & K_t \geq 0.80 \end{cases} . \tag{2.39}$$

For complex topography it is assumed that the diffuse radiation is proportional to the local values of the sky view factor S_v; hence, a modified version of (2.36) is adopted, which takes the following form:

$$R'_G = R_I + R'_D = R_G(i_R + S_v d_R) = EK_t(i_R + S_v d_R). \tag{2.40}$$

In this case K_t is estimated in terms of the measured value of global radiation R'_G at a site through (2.40), where we set $S_v = S_{v,m}$, $S_{v,m}$ being the sky view factor of the measurement point, and we use equations 2.37, 2.38 and 2.39 to compute i_R and d_R. Furthermore, the values of i_R and d_R are assumed to be constant over the whole domain at a given time (i.e. at a given solar zenith angle). Hence, once the value of K_t has been determined, equation 2.40 can be used to compute the global radiation R'_G at a given site in terms of the local value of the sky view factor.

When the measure of K_t is not available (or not reliable), empirical formulations can be used to compute the global atmospheric trasmissivity; however, they do not account for the sky view factor, nor for the splitting between diffuse and incident radiation. An example is the following formula

$$K_t = (0.6 + 0.2\cos\xi)\,(1 - 0.5N)^3\,, \tag{2.41}$$

which can be derived from Stull (1988) relationship, in which N is the cloud coverage

fraction. Notice that in this case the global radiation at a site is simply calculated as:

$$R'_G = R_G = EK_t. \tag{2.42}$$

2.2.2.4. Sensible heat flux

The sensible heat flux represents the part of energy budget which effectively contributes to the heating of the air mass above valley floor. Its computation preliminarily requires the estimate of the net radiation Q_*. In the present model a modified expression with respect to the original formulation of Holtslag and van Ulden (1983) is used, which takes the following form:

$$Q_* = \frac{(1-a')R'_G + c_1 T^6 - \sigma T^4}{1 + c_H}. \tag{2.43}$$

Notice that equation 2.43 doesn't include the additional term proportional to cloud coverage. In fact, according to the present procedure, the filtering effect and the diffuse radiation effect of cloud cover are already included in the computation of R'_G.

In (2.43) the correction for the albedo with respect to solar elevation is accounted for, using the expression of Paltridge and Platt (1976):

$$a' = a + (1-a)\exp\left[-0.15(90-\xi) - 0.5(1-a)^2\right]; \tag{2.44}$$

furthermore σ is the Stefan-Boltzmann constant, $c_1 = 5.31 \cdot 10^{-13} W/\left(m^2 K^6\right)$ is an empirical constant and c_H ranges about 0.12; according to van Ulden and Holtslag (1985) and Hanna and Chang (1992), c_H is found to depend on soil type and moisture.

The sensible heat flux Q_H is then computed using the following formula:

$$Q_H = \frac{r_B}{1 + r_B}(1 - c_g)\, Q_*, \tag{2.45}$$

where r_B is the Bowen ratio, which mainly depends on soil moisture, and c_g is a function of the properties of the surface, for which Oke (1982) suggests a value ranging between 0.05 and 0.25 for rural areas, or between 0.25 and 0.30 for urban areas. In the present work a constant value of $c_g = 0.20$ is used for the whole domain, while the default values of the Bowen ratio suggested in the original code of CALMET are kept.

Finally, the night-time energy balance at the ground level is closed according to the original formulation of Holtslag and van Ulden (1983).

2.2.2.5. Turbulent diffusivity

In the present model the Monin Obukhov length L and the friction velocity u_* are computed iteratively from the output values of temperature, T, and wind field, u, generated by CALMET, using the following expressions (Panofsky and Dutton, 1984):

$$L_{MO} = -\frac{\rho c_p u_*^3 T}{kgQ_H}, \tag{2.46}$$

$$u_* = \frac{ku}{\ln \frac{z}{z_0} - \Psi\left(\frac{z}{L}\right) + \Psi\left(\frac{z_0}{L}\right)}. \tag{2.47}$$

where k is von Karman constant, ρ is the air density, c_p is the specific heat at constant pressure, g is gravity, z is the reference height ($z = 3\,m$ over the local surface is adopted in the present work), and z_0 is the roughness length. The similarity function Ψ is the one defined in equation 1.7. Finally, the similarity law for vertical turbulent diffusivity given in equation 1.19 is adopted:

$$K_z(z) = \frac{ku_*z}{\Phi}. \tag{2.48}$$

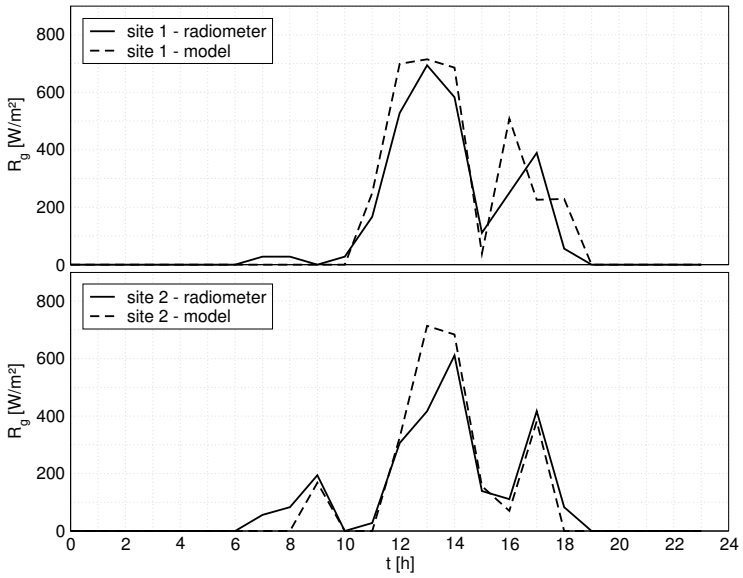

Figure 2.12.: Global solar radiation in a cloudy day: comparison between computed values and data registered by radiometers 1 and 2 (see figure 2.10).

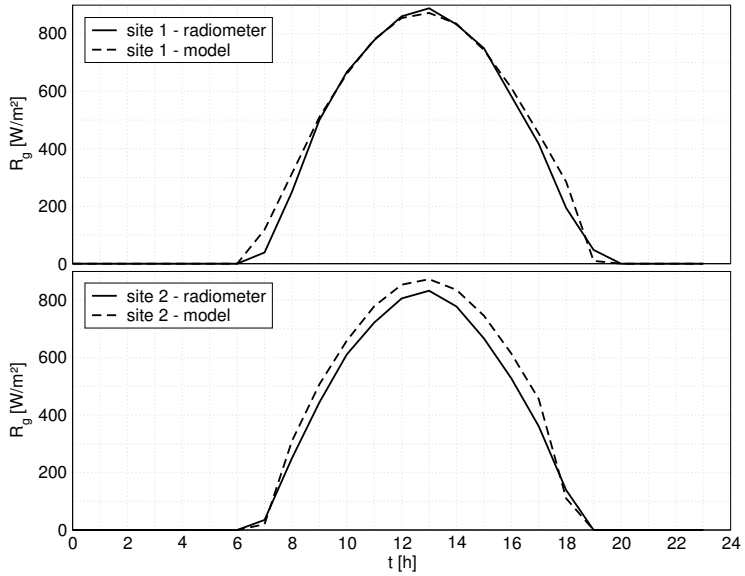

Figure 2.13.: Global solar radiation in a sunny day: comparison between computed values and data registered by radiometers 1 and 2 (see figure 2.10).

2.2.3. Results

The values of model parameters ($c_g = 0.20$, $c_H = 0.12$) have been determined through the calibration of computed global solar radiation based on the whole set of data (one year) from two radiometers in the study area (denoted as site 1 and 2 in figure 2.10). Computed values of R_G, based on the above estimates, are compared with values of global radiation registered in a cloudy day and in a sunny day in figures 2.12 and 2.13, respectively. The computed global radiation in a sunny day evaluated at different locations across the Adige Valley is shown in figure 2.14: the time shift exhibited by the daily distributions at different locations clearly reflects the effect of shadows generated by mountain profiles.

A comparison between the values of sensible heat flux and turbulent diffusivity obtained using the proposed procedure, which accounts for orographic factor, and those computed through the standard procedure is given in figures 2.15 and 2.16. Data refer to three different locations within the study area of figure 2.10. It is worth noticing that the introduction of the complex terrain correction leads to a change in the daily behavior of sensible heat flux cycle and turbulent diffusivity. When the complex terrain correction is not used, there may still be a difference in the daily evolution of sensible heat flux at different points; however this is only due to the spatial variation of soil type.

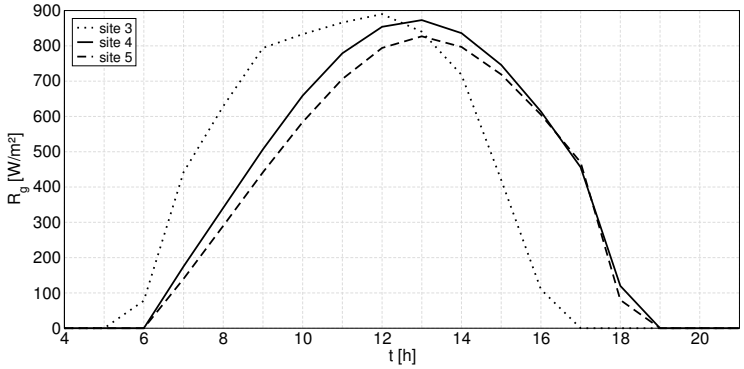

Figure 2.14.: Computed global solar radiation at different locations in a sunny day (see figure 2.10).

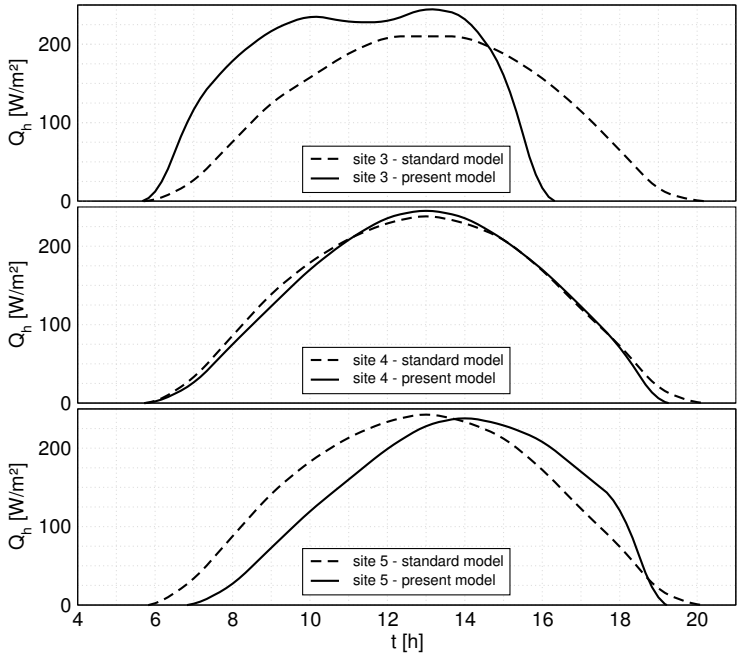

Figure 2.15.: Computed values of sensible heat flux at different sites in the study area in a sunny day.

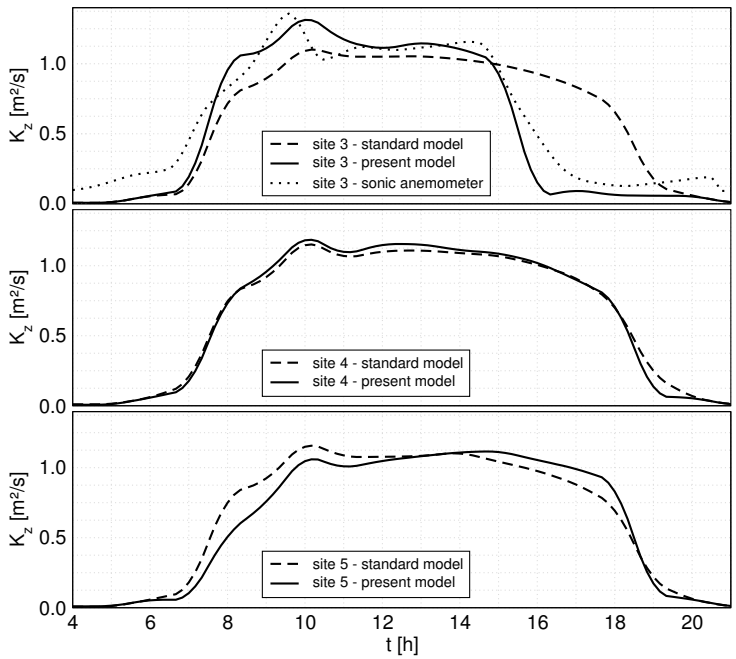

Figure 2.16.: Measured values (at site 3) and computed values (at site 3, 4 and 5) of vertical turbulent diffusivity in the study area in a sunny day.

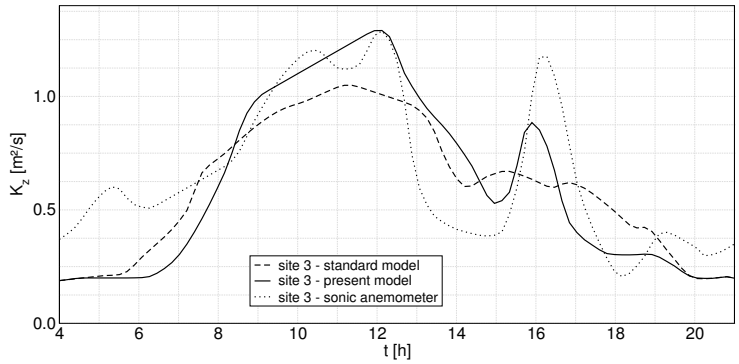

Figure 2.17.: Comparison between computed and observed values of turbulent diffusivity at the test site 3 of the study area in a cloudy day.

Predicted values of turbulent diffusivity at site 3, as obtained through the standard model and the present model, are compared with sonic anemometer data in figures 2.16 and 2.17 for the case of a sunny and cloudy day, respectively. Meteorological data have been collected during two field campaigns performed in 2002 by the Department of Civil and Environmental Engineering of the University of Trento, both in the winter and in the summer season, spanning globally over 35 days.

The comparison suggests that a better prediction of peak values of K_z can be achieved when the orographic factor is taken into account. It is worth noticing that both models are able to reproduce the decrease of K_z associated with the extinction of the direct radiation at sunset (notice that site 3 is located on the western side of the valley floor); however, the response of the standard model, which doesn't account for the orographic factor, exhibits a time delay of nearly 2 hours, while the present model seems to follow more closely the observed behaviour. This is also shown in figures 2.19a-b, where the time lag of the model response to the extinction of direct radiation with respect to the measured data is reported, for the whole range of field observations.

For a better understanding of the influence of orography on sensible heat flux and, consequently, on turbulent diffusivity, maps of computed values of K_z at ground level are included in figure 2.18. It may be observed that, with respect to the usual approach, the major changes induced by the introduction of the complex terrain module mainly occur in the morning and in the late afternoon. The effect is quite sharp in the case examined, due to the North-South orientation of the Adige Valley, which implies that the projection of the solar path at the ground is nearly perpendicular to the valley axis. Under these conditions turbulent diffusivity may attain values at the ground which are $3 \div 4$ times larger than the values predicted through standard procedures like those which are commonly used in diagnostic meteorological and dispersion models.

2.2.4. Testing the model

A clear evidence of the effect of the daily evolution of turbulence characteristics on pollutant dispersion close to the valley side is given in pictures 2.20a-b which have been taken in the surroundings of test site 5. The illustrated situation has been reproduced using the lagrangian model which will be described in chapter 3. Figures 2.21 and 2.22 show quite clearly that the dilution capacity of the air mass strongly changes when sun rises. The results obtained for a release from the site 5 are compared to those obtained when the pollutant is released in the surroundings of site 3. We may notice that when the orographic factor is not accounted for, the numerical results for site 3 and 5 would obviously show the

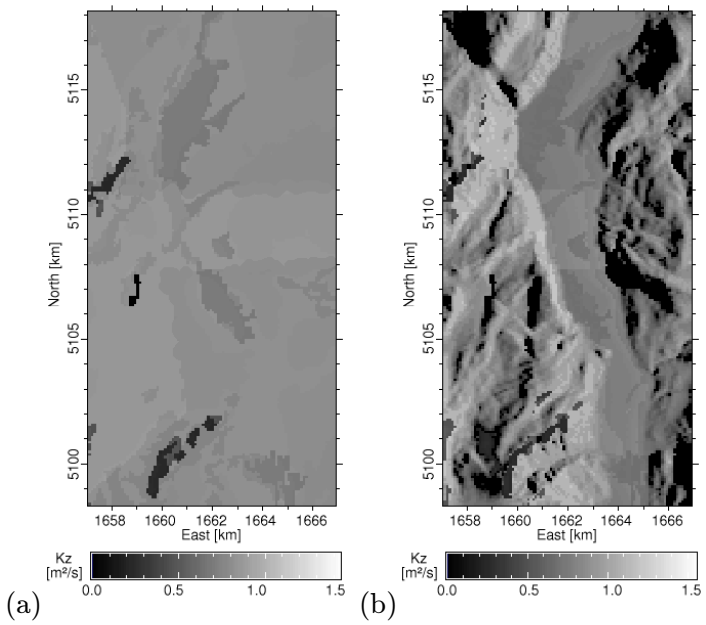

t=8 AM

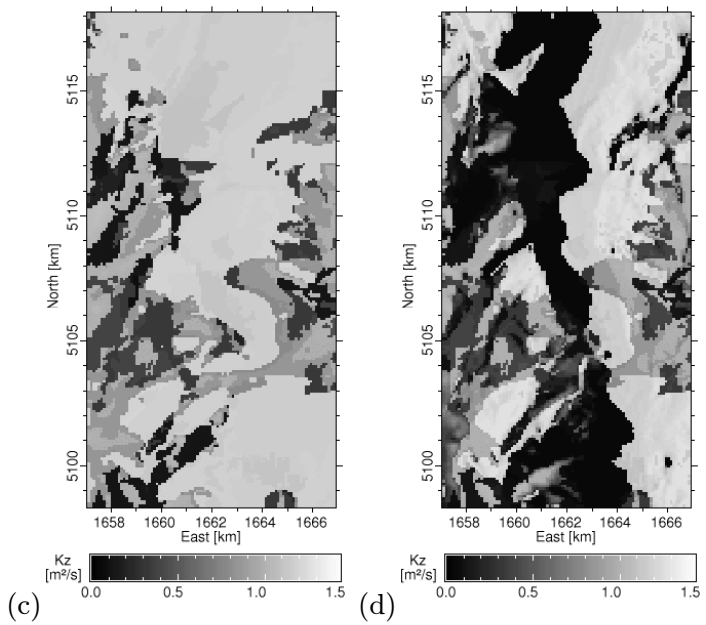

t=6 PM

Figure 2.18.: Maps of the computed K_z at ground level ($z = 3\,m$) in the morning and in the late afternoon: (a, c) standard method; (b, d) present model.

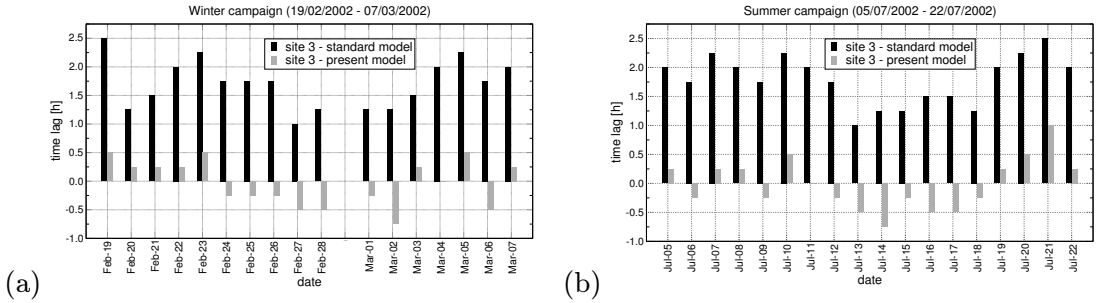

(a) (b)

Figure 2.19.: Time lag of the model response with respect to field observations of the decay of turbulent diffusivity due to the extinction of direct radiation at sunset: a) winter and b) summer measurements.

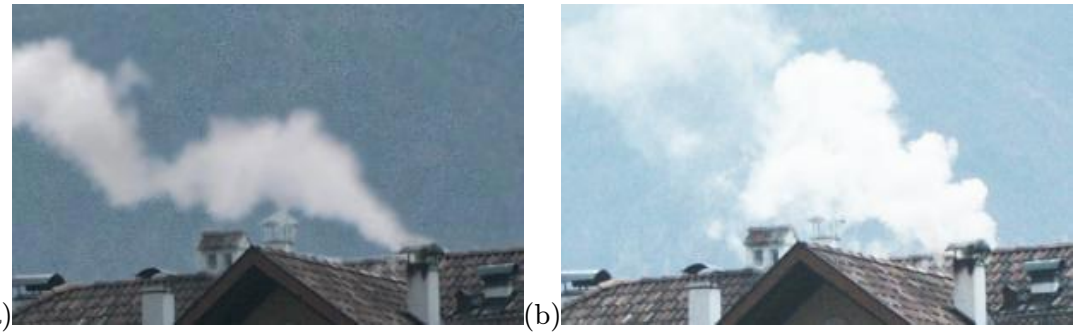

(a) (b)

Figure 2.20.: Effluent smoke from domestic heating. The stable stratification maintains a compact plume (picture a) before sunrise, while the growing turbulence spreads it more rapidly (picture b), two hours after sunrise. Both pictures are taken at the same site in low wind condition.

same behaviour.

Moreover, as also pointed out in section 1.4, stability profiles following similarity laws can be suitably applied to describe the surface layer. Hence, in this example a near-ground source was used for testing, in order to avoid significant transport of pollutant outside the surface layer. Elevated sources or strongly buoyant plumes should be therefore treated adding a different parametrization for vertical eddy diffusivity above the surface layer, like that described in the global approach (see section 2.1.1.3).

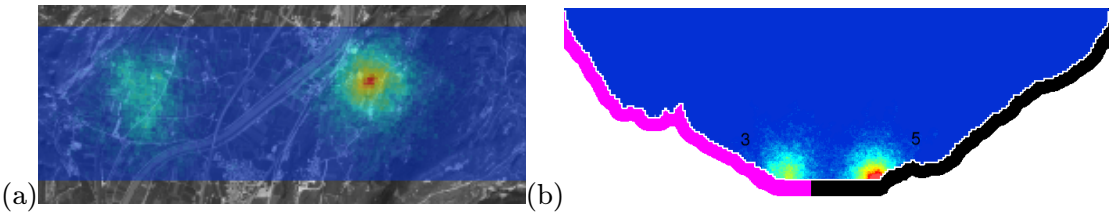

Figure 2.21.: Results of the numerical simulation, through the lagrangian model of chapter 3, of ground level emission, before sunrise, at site 5 under low wind condition: a) plan view and b) vertical section. Color scale is relative (red=maximum, blue=minimum concentration). Violet contour indicates irradiated surface, while black indicates not irradiate surface.

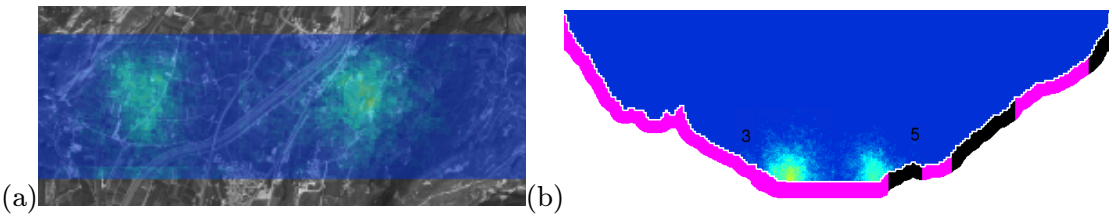

Figure 2.22.: Results of the numerical simulation, through the lagrangian model of chapter 3, of ground level emission, two hours after sunrise, at site 5 under low wind condition: a) plan view and b) vertical section. Color scale is relative (red=maximum, blue=minimum concentration). Violet contour indicates irradiated surface, while black indicates not irradiate surface.

2.3. Conclusions

The proposed local approach model accounts for the effect of shadows generated by mountain profiles. Results reported in figures 2.16, 2.17 and 2.19 suggest that the model is able to reproduce the time shift of the daily cycle of turbulent diffusivity K_z which is observed at different locations in the Adige valley. A similar behaviour is also exhibited by the other relevant quantities (the global radiation, the net radiation and the sensible heat flux). The orographic factor mainly affects the estimate of the turbulent diffusivity at the ground, where the present model predicts much larger values of K_z than those obtained with standard procedures. Hence, the described correction is likely to be more relevant for numerical simulations of the dispersion of pollutants from ground sources like roads or waste dumps. Finally, it is worth noticing that the proposed procedure is fairly general; hence, its use is not restricted to applications in connection with CALMET preprocessor.

The global approach can be suitably be adopted for compact valleys characterized by

uniform flow pattern (i.e. negligible secondary flow, no inflow or outflow due to tributary valleys, low curvature of the valley); its application is thus restricted to well defined cases and cannot be inserted in a general implementation of an air dispersion model. Therefore, in developing a lagrangian dispersion model for complex terrain (chapter 3), the local approach has been considered as preferable.

3. Lagrangian modelling

3.1. The lagrangian approach

3.1.1. Introduction

Fluid motion and any scalar function (potential temperature, concentration...) transported by fluid motion can be described within two frames of reference: a stationary frame (eulerian) and one which is moving along with the flow field (lagrangian). In the eulerian perspective, the flow and its constituents are described with respect to fixed spatial positions. The lagrangian perspective, on the contrary, follows the flow and traces the history of individual particles. Unlike in the eulerian description, spatial position is not a fixed reference but another variable of the particle.

The lagrangian modelling is nowadays applied increasingly in simulation of atmospheric dispersion of pollutants, due to its ability to catch some peculiarity of turbulent flows. In a particle dispersion model, once the statistical properties of turbulence and the mean flow are given, a large number of particle trajectory are integrated, considering their motion to be partially deterministic (due to mean flow) and partially stochastic (due to turbulence). Usually particles are considered to be passive tracer and so they are treated in this work. Nevertheless it should be remembered that not every pollutant can be modelled as a passive tracer, depending on the time scale of motion and of its reaction time.

Every particle time-integrated trajectory corresponds to a different flow realization: different particles follow different flow lines, because of turbulent fluctuations; if diffusion were not considered, particles would obviously be only subjected to a deterministic flow and thus show the same trajectory. As each particle is characterized by independent motion, the diffusion mechanism is then simulated by an ensemble mean of different flow realization (figure 3.1). A lagrangian model is able to simulate both stationary and non-stationary emission sources, simply varying the number of particles released per time unit.

Lagrangian models for transport in turbulent flows describe the trajectories of fluid particles on the basis of the eulerian properties of the flow; the motion of a set of a high number of particles is followed and the statistical properties are derived and put in rela-

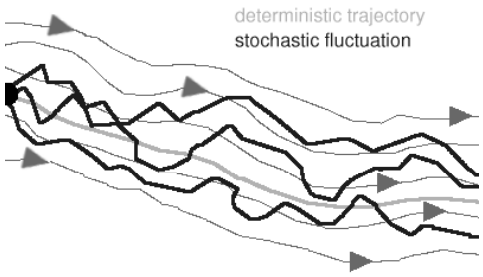

Figure 3.1.: Lagrangian scheme: deterministic and stochastic motion.

tionship with concentration. Lagrangian models are classified in "one-particle" schemes, describing absolute dispersion, and "two-particles" which reproduce relative dispersion processes (Crone, 1997). The latter approach will not be discussed here.

The criteria needed to specify the transport equations were first enunciated by Thomson (1987), who showed that only two conditions are sufficient to formulate the equations of motion for a particle: the model should be consistent with similarity laws in the inertial subrange and it should satisfy the well-mixed condition which is another formulation of the second law of thermodynamics (Sawford, 1986).

3.1.2. Theory

In the lagrangian approach pollutant is treated as an ensemble of single particles each characterized by mass, position and momentum. Their motion which is determined both by advective and diffusive processes, is followed using a moving coordinate system. Concentration is given as the average over a large number (strictly infinite) of realizations in the form:

$$\langle C(\mathrm{r},t)\rangle = \int_{-\infty}^{t}\left[\int_{V} p(\mathrm{r},t|\mathrm{r}',t')\cdot S(\mathrm{r}',t')d\mathrm{r}'\right]dt', \tag{3.1}$$

where V is the volume of the average domain, $S(\mathrm{r}',t')$ the source term and $p(\mathrm{r},t|\mathrm{r}',t')$ the probability density function (hereafter referred to as PDF) associated to a particle moving from position r' at time t' and reaching position r at time t. The main requirement is the determination of the statistical structure of p, which mainly depends on physical properties of the dispersion process (Zannetti, 1990).

The lagrangian approach avoids the problem of treating the diffusive term, which is

usually closed in the eulerian approach, using Fick's law:

$$\left\langle u_i' C' \right\rangle = -K_i \frac{\partial \left\langle C \right\rangle}{\partial x_i}. \tag{3.2}$$

It can be nevertheless shown that only for long time (far field) lagrangian solution can be reproduced using Fick's closure.

3.1.3. Extent of the puff

Let's consider a point source with a release of N particles in a homogeneous stationary turbulent flow field characterized by vanishing mean velocity. A statistical analysis can be carried out on particles position and velocity. For simplicity, the unidimensional case, defined in terms of a z coordinate system and a corresponding velocity w, is considered. Since the mean flow is absent, the barycenter in this case coincides with the release point, while the puff expands in time only due to turbulent motion; hence,

$$\left\langle z(t)^2 \right\rangle = \frac{1}{N} \sum_{i=1}^{N} z_i(t)^2. \tag{3.3}$$

The lagrangian correlation coefficient $R(\tau)$, defined as

$$R(\tau) = \frac{\langle w(t) w(t+\tau) \rangle}{\langle w^2 \rangle} \tag{3.4}$$

is introduced, which provides a measure of the speed of a particle is persistent in time.

As the particle velocity is defined as $w \equiv \frac{dz}{dt}$, it is then possible to relate $\left\langle z^2 \right\rangle$ and $\left\langle w^2 \right\rangle$. In fact, integrating (3.3) twice in time, one obtains:

$$\left\langle z(t)^2 \right\rangle = 2 \left\langle w^2 \right\rangle \int_0^t \left[\int_0^T R(\tau) d\tau \right] dt. \tag{3.5}$$

For small values of t, $R(\tau) \simeq 1$; as a consequence:

$$\left\langle z^2 \right\rangle \simeq \left\langle w^2 \right\rangle t^2, \tag{3.6}$$

or, equivalently

$$\sigma_z \simeq \sigma_w t, \tag{3.7}$$

where $\sigma_w = \sqrt{\langle w^2 \rangle}$ is the standard deviation of velocity, $\sigma_z = \sqrt{\langle z^2 \rangle}$ is a characteristic measure of the dimension of the puff, changing in time.

On the contrary, for $t \to \infty$ the correlation vanishes ($R(t) \to 0$); it is then possible to estimate the lagrangian correlation time as

$$T_L = \int_0^\infty R(\tau) d\tau. \tag{3.8}$$

In the latter case ($t \gg T_L$) equation 3.5 reduces to the following simplified form:

$$\left\langle z^2 \right\rangle \simeq 2 \left\langle w^2 \right\rangle t T_L, \tag{3.9}$$

or, using an alternative notation,

$$\sigma_z \simeq \sigma_w \sqrt{2 t T_L}. \tag{3.10}$$

An approximate version of equation 3.5 which has bee recommended for dispersion modelling by Gryning et al. (1987), takes the following form:

$$\sigma_z = \frac{\sigma_w t}{1 + \sqrt{\frac{t}{2T_L}}}, \tag{3.11}$$

where t is travel time of the released puff of pollutant. Equations 3.5 or 3.11 suggest that fluctuations of the wind velocity are the leading factors in determining the dispersion process of plumes. In practical problems, however, T_L is not an easily measurable parameter; it can be estimated using empirical relationships which depend on turbulence parametrization, as shown in section 3.1.4.

Also notice that the assumption often used in dispersion modelling, which reflects a Fick's closure, namely

$$\sigma_{x,y,z} = \sqrt{2 K_{x,y,z} t}, \tag{3.12}$$

is only valid for $t \gg T_L$, i.e. in the far field, as shown in figure 3.2.

3.1.4. Empirical formulation for T_L and K_z

Lagrangian time scale can vary within a physical domain in actual situations when the hypothesis of spatial homogeneity is not valid. An estimate of the vertical profile of lagrangian time scale, valid for every stability condition, has been proposed by Degrazia et al. (2000):

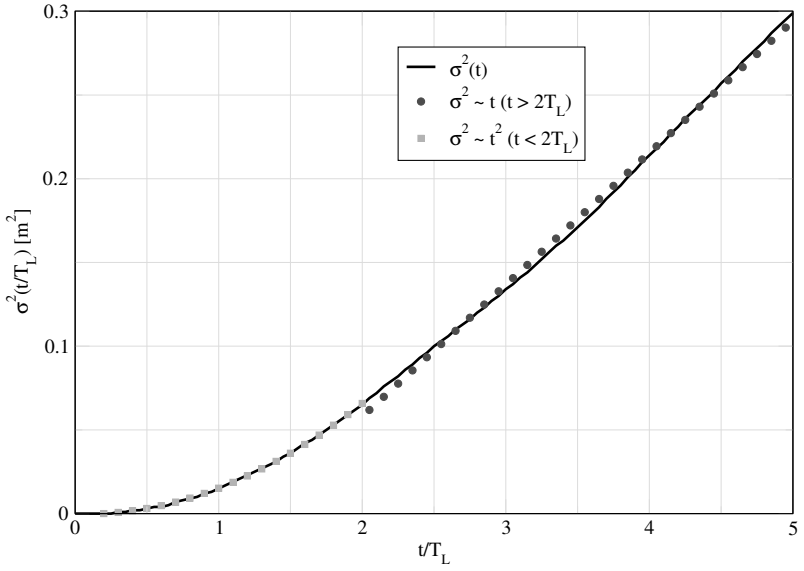

Figure 3.2.: Near field extension of the puff of particles.

$$T_L(z) = \begin{cases} \dfrac{0.19z}{u_*\left[1+3.7\frac{z}{L_{MO}}\left(1-\frac{z}{h}\right)^{-5/4}\right]\left(1-\frac{z}{h}\right)^{3/4}} & \left(\frac{z}{L_{MO}} > 0\right) \\ 0.39\frac{z_i}{w_*}\left(-0.01\frac{z}{L_{MO}}\right)^{1/2}\left[1-\exp\left(-4\frac{z}{z_i}\right)-0.0003\exp\left(8\frac{z}{z_i}\right)\right]^{4/3} & \left(\frac{z}{L_{MO}} < 0\right) \end{cases} . \tag{3.13}$$

Notice that for $z/L_{MO} = 0$ (neutral condition) and for $z = 0$ (surface level), a vanishing value of T_L results, which is not acceptable; hence, in applying the above formula a suitable minimum value for T_L has to be imposed. In the same study Degrazia et al. (2000) also provide a corresponding profile for K_z, valid for the entire ABL under any stability conditions:

$$K_z(z) = \begin{cases} \dfrac{0.4\left(1-\frac{z}{h}\right)^{3/4}u_*z}{1+3.7\frac{z}{L_{MO}}\left(1-\frac{z}{h}\right)^{-5/4}} & \left(\frac{z}{L_{MO}} > 0\right) \\ 0.16w_*z_i\left(-0.01\frac{z}{L_{MO}}\right)^{1/2}\left[1-\exp\left(-4\frac{z}{z_i}\right)-0.0003\exp\left(8\frac{z}{z_i}\right)\right]^{4/3} & \left(\frac{z}{L_{MO}} < 0\right) \end{cases} . \tag{3.14}$$

The proposed structure is very similar to that of equation 1.24 and hence is subject to the same limitations. The variance of vertical velocity, which is required for lagrangian particle tracking modelling, as shown in section 3.2.2, can be derived from (3.13) and (3.14)

in the form:

$$\sigma_W(z) = \sqrt{\frac{K_z(z)}{T_L(z)}}. \tag{3.15}$$

3.2. Langevin equation

The trajectories of particles are developed in the hypothesis of fully developed turbulence (i.e. flow characterized by high Reynolds number) and incompressible fluid. To simulate stochastic processes two different approaches are known in literature. The first one, which will be denoted as "1-equation model", is based on the explicit integration of the equation

$$\mathrm{dx} = \mathrm{u}(t, \mathrm{x})dt + \mathrm{B}(t)dr, \tag{3.16}$$

where x is the position of the particle along the lagrangian trajectory at time t (e.g. Gardiner, 1983). According to the second approach (Thomson, 1987), denoted as "2-equations model", the trajectory is determined as the solution of a couple of equations: the first is a stochastic differential equation of Ito type (explained in section 3.2.3), namely

$$\mathrm{du} = \mathrm{a}(t, \mathrm{x}, \mathrm{u})dt + \mathrm{B}(t, \mathrm{x})dr, \tag{3.17}$$

while the second consists of the deterministic integration of the trajectory in time:

$$\mathrm{dx} = \mathrm{u}dt. \tag{3.18}$$

The stochastic differential equation for the velocity is often referred to as "Langevin equation".

We may notice that in a "2-equations model" each particle is assumed to move independently: its position and speed follow a Markov process (Thomson, 1987). The method is more physically based and will be described more in detail in the following section.

Widely used "1-equation" (i.e. only position) lagrangian models are equivalent to the "constant K" eulerian assumption. In the first case the memory of the initial condition is lost gradually; in the second case particles immediately switch to the eulerian flow field velocity

3.2.1. 2-equations model

In the formulation of transport equations the trajectory is assumed to be completely determined by the turbulent flow: the velocity and position of a particle are continuous functions of time. Furthermore, it is assumed that the stochastic process defined by the particle's velocity and position is Markovian. On the basis of these assumptions, rewriting equations 3.16 and 3.17 in term of their components (the procedure can be applied for 1D, 2D or 3D simulation and subscript i denotes the coordinates), the transport of a particle can be modelled as follows (Thomson, 1987):

$$du_i = a_i\left(\mathrm{x},\mathrm{u},t\right)dt + B_{ij}\left(\mathrm{x},\mathrm{u},t\right)dr_j, \tag{3.19}$$

$$dx_i = u_i dt, \tag{3.20}$$

where dr is a random number extracted from Wiener process (i.e., a gaussian process whose increments are independent) described by a PDF with 0 mean and variance dt, such that:

$$\begin{cases} \langle dr_j \rangle = 0 \\ \langle dr_j dr_k \rangle = dt \end{cases}. \tag{3.21}$$

The vector function $\mathrm{a}\left(\mathrm{x},\mathrm{u},t\right)$ and the tensor $\mathrm{B}\left(\mathrm{x},\mathrm{u},t\right)$ can be identified as drift and diffusion terms, respectively, and must be evaluated to be consistent with the flow field. The particle's velocity u is also affected by the mean velocity of the flow, denoted by U. Notice however that this term does not affect the stochastic process.

Equations 3.19, 3.19 and 3.21 define a Markov process; the PDF $p_L\left(\mathrm{x},\mathrm{u},t|\mathrm{x}_0,\mathrm{u}_0,t_0\right)$ (i.e. the probability related to a particle starting at time t_0, position x_0 and velocity u_0 and reaching after a time dt a generic position x with speed u) of this process satisfies the Fokker-Planck equation, which reads:

$$\frac{\partial p_L}{\partial t} = -\frac{\partial p}{\partial x_i}\left(u_i p_L\right) - \frac{\partial p}{\partial u_i}\left(a_i p_L\right) + \frac{\partial^2}{\partial u_i \partial u_j}\left(B_{ij} p_L\right), \tag{3.22}$$

where B is a tensor with elements $B_{ij} = \frac{1}{2} B_{ik} B_{jk}$. The main issue at this point is to find appropriate expressions for a and B. Thomson (1987) showed that for a correct formulation it is sufficient to impose that the model satisfies two conditions. In particular:

- the model should give correct results in the inertial subrange; in other words, for time-

scales larger than the typical lifetime of the smallest turbulent eddies and smaller than the lifetime of the largest eddies, the velocity variations obey to a universal form (Monin and Yaglom, 1975):

$$\langle du_i du_j \rangle = C_0 \epsilon \delta_{ij} dt, \tag{3.23}$$

where ϵ is the mean rate of dissipation of turbulence kinetic energy and C_0 is a universal constant, whose value may range, according to different authors, between 2 and 7 (e.g. Crone, 1997); furthermore, the tensor B is found to be independent on the time-scale properties of the flow, that is:

$$B_{ij} = \delta_{ij} \frac{C_0 \epsilon}{2}; \tag{3.24}$$

the above condition also implies that all diagonal terms of B are equal;

- to determine the acceleration term a it is necessary and sufficient to impose the well-mixed condition to the PDF, which states that if particles are initially well-mixed both in velocity and position, they'll remain so; from a mathematical point of view, this condition is equivalent to affirm that the lagrangian PDF, p_L, of tracer particles coincides with the eulerian PDF, p_E, of the fluid; following Thomson (1987) it can be shown that this condition is ensured, provided that the function ϕ satisfies the following equation:

$$\frac{\partial \phi_i}{\partial u_i} = -\frac{\partial p_E}{\partial t} - \frac{\partial}{\partial x_i} \left(u_i p_E \right), \tag{3.25}$$

where $p_E \left(\mathrm{u}_0 | \mathrm{x}_0, t_0 \right)$ is the eulerian PDF related to starting position x_0, t_0; the components of a are then derived, recalling (3.24), through the following expression:

$$a_i = \frac{C_0}{2 p_E} \frac{\partial}{\partial u_i} \left(\epsilon p_E \right) + \frac{\phi_i}{p_E}. \tag{3.26}$$

3.2.2. Gaussian turbulence

In gaussian turbulence p_E can be denoted as p_G and written in the form (Thomson, 1987):

$$p_G = \frac{1}{(2\pi)^{\frac{3}{2}} \sqrt{\det \mathrm{V}}} \exp \left[-\frac{1}{2} \left(u_i - U_i \right) \left(\mathrm{V}^{-1} \right)_{ij} \left(u_j - U_j \right) \right], \tag{3.27}$$

while the term $\frac{\phi_i}{p_G}$ is given by

$$\begin{aligned}\frac{\phi_i}{p_G} &= \frac{1}{2}\frac{\partial V_{il}}{\partial x_l} + \frac{\partial U_i}{\partial t} + U_l\frac{\partial U_l}{\partial x_l} \\ &+ \left[\frac{1}{2}\left(\mathrm{V}^{-1}\right)_{lj}\left(\frac{\partial V_{il}}{\partial t} + U_m\frac{\partial V_{il}}{\partial x_m}\right) + \frac{\partial U_i}{\partial x_j}\right](u_j - U_j) \\ &+ \frac{1}{2}\left(\mathrm{V}^{-1}\right)_{lj}\frac{\partial V_{il}}{\partial x_k}(u_j - U_j)(u_k - U_k)\,, \end{aligned} \tag{3.28}$$

where

$$V_{ij} = \langle (u_i - U_i)(u_j - U_j)\rangle \tag{3.29}$$

Notice that capital letters denote eulerian quantities (i.e. flow field velocity and variance), while small letters are used for lagrangian velocity referred to each particle. Under the hypothesis of gaussian turbulence, the acceleration terms read:

$$a_i = -B_{ij}\left(\mathrm{V}^{-1}\right)_{jk}(u_k - U_k) + \frac{\phi_i}{p_G}. \tag{3.30}$$

The coefficients of the random term are closed by a simple relationship in which the lagrangian time scale appears and is related to turbulent energy content of the fluid:

$$C_0\epsilon = \frac{2\sigma^2}{T_L}; \tag{3.31}$$

substituting in (3.24) we obtain:

$$B_{ij} = \delta_{ij}\frac{\sigma_i^2}{T_L}. \tag{3.32}$$

In the unidimensional case, along the z direction, the system (3.19)-(3.19) takes the following simple form:

$$\begin{cases} dz = wdt \\ dw = adt + bdr \end{cases}, \tag{3.33}$$

where

$$a = -\frac{w - W}{T_L} + \frac{1}{2}\frac{\partial\sigma_W^2}{\partial z} + \frac{\partial W}{\partial t} + \frac{1}{2\sigma_W^2}\left(\frac{\partial\sigma_W^2}{\partial t} + W\frac{\partial\sigma_W^2}{\partial z}\right)(w - W) + \frac{1}{2\sigma_W^2}\frac{\partial\sigma_W^2}{\partial z}(w - W)^2 \tag{3.34}$$

and

$$b = \frac{\sigma_W^2}{T_L}.$$

Equation 3.33 has to be solved numerically through a simple explicit chain rule, approximating all the derivatives appearing in (3.34) with the corresponding finite differences:

$$\begin{cases} z^{n+1} = z^n + w^n \Delta t \\ w^{n+1} = w^n + a^n \Delta t + b^n dr^n \end{cases}. \tag{3.35}$$

The same explicit scheme is adopted for solving the three-dimensional formulation.

According to Thomson (1987) and Tampieri (1997), the time step Δt should be small enough to achieve an acceptable result; in order to ensure that a particle cannot change its position by a too large amount, thus loosing information on the smaller scale fluctuations, Thomson (1987) suggests the condition:

$$\Delta t \leq \min\left(\frac{1}{20}T_L, \frac{1}{10}\frac{\sigma_W}{a_W}\right). \tag{3.36}$$

Indeed, the first condition posed by (3.36) seems to be sufficient, i.e. $\Delta t \ll T_L$, which is required for the near field evolution to take into account the inertial delay in the motion of an air parcel being accelerated from the flow field. The second condition appears to be relevant only in the strongly inhomogeneous case.

Boundary conditions imposing the null flux at the border, $\frac{\partial C}{\partial n} = 0$, is simply simulated through geometric reflection at the surface, as shown in figure 3.3. In the direction of particle is reflection (for example z), the final position and velocity are corrected as follows:

$$\begin{cases} w_f = 2z_b - z_0 - w_0 dt \\ w_f = -w_0 \end{cases}, \tag{3.37}$$

where z_b is the surface level, and the subscripts 0 and f indicate the starting and final position, respectively.

Alternatively, the particle can be stopped at the surface to simulate deposition.

3.2.3. Ito's formula

In equation 3.26 some extra acceleration terms appear, which are not conventional derivatives. In this section we explain Ito's rule to differentiate an expression of the form $f(u)$, where f is a differentiable function and u a stochastic function. If u were also differentiable,

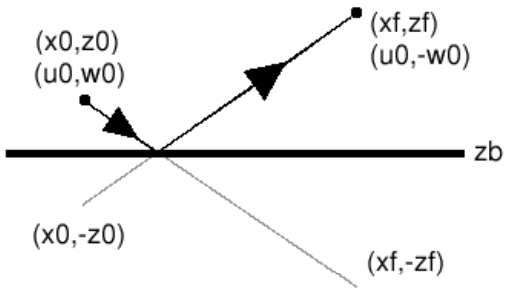

Figure 3.3.: Reflection at the boundary where null flux condition is imposed.

then the ordinary chain rule would give:

$$df = \frac{\partial f}{\partial u} du. \tag{3.38}$$

However, u is not differentiable; hence the correct formula exhibits an extra term (Arnold, 1974), and reads:

$$df = \frac{\partial f}{\partial u} du + \frac{1}{2} \frac{\partial^2 f}{\partial u^2} du^2. \tag{3.39}$$

Now suppose that $u = u(x,t)$; then also derivatives with respect to t and x appear:

$$df = \frac{\partial f}{\partial t} dt + \frac{\partial f}{\partial x} dx + \frac{\partial f}{\partial u} du + \frac{1}{2} \frac{\partial^2 f}{\partial u^2} du^2. \tag{3.40}$$

Substituting Langevin equations $du = adt + bdr$ and $dx = udt$ in (3.40) we obtain:

$$\begin{aligned} df &= \frac{\partial f}{\partial t} dt + \frac{\partial f}{\partial x} udt + \frac{\partial f}{\partial u} (adt + bdr) + \frac{1}{2} \frac{\partial^2 f}{\partial t^2} dt^2 \\ &+ \frac{1}{2} \frac{\partial^2 f}{\partial x^2} u^2 dt^2 + \frac{1}{2} \frac{\partial^2 f}{\partial u^2} \left(a^2 dt^2 + 2abdtdr + b^2 dr^2 \right). \end{aligned} \tag{3.41}$$

Since $dr \sim \sqrt{dt}$, only terms proportional to $dt^2$are negligible and thus vanish, while terms of order dr^2 must be kept.

$$df = \frac{\partial f}{\partial t} dt + \frac{\partial f}{\partial x} udt + \frac{\partial f}{\partial u} adt + \frac{\partial f}{\partial u} bdr + \frac{1}{2} \frac{\partial^2 f}{\partial u^2} b^2 dt. \tag{3.42}$$

3.2.4. Difference between 1- and 2- equation models

Using a "1-equation" lagrangian model is equivalent to converting the Markov process for the velocity and position of the particles into one for their position only. It can be showed that even this simplification has no large effects on the simulated tracer in long range applications (far field). The reason for this is that the most important process affecting the far field tracer dispersion is the evolution the flow field along the particles path. However, the error affecting the solution near the source (near field) caused by an oversimplified dispersion algorithm ("1-equation") could imply much larger errors at later times. A compromise to save computation time while maintaining sufficient accuracy would therefore be the use of short time steps close to the source, increasing the time step when the tracer is already well-mixed. Therefore, it is important to use a "2-equations" model at least in the near field.

We can use the unidimensional test case to compare the Langevin system

$$\begin{cases} dz = wdt \\ dw = adt + bdr \end{cases}, \tag{3.43}$$

with the simpler formulation

$$dz = wdt + cdr. \tag{3.44}$$

Let's consider a set of particles which are released with an initial velocity w_0 into a flow field characterized by uniform velocity $-w_G$, which may also represent the asymptotic gravitational settling speed, as shown in figure 3.4. Physically speaking one would expect the particle to loose gradually its initial velocity (according to parameter T_L) and adapt to the flow field. The "2-equations" model perfectly simulates the expected behaviour, while in the "1-equation" model particles immediately switch to the asymptotic velocity, except for turbulent fluctuations (see figure 3.5).

3.2.5. Kinematic interpretation of T_L

From a kinematic point of view, the role of T_L is equivalent to a frictional term. This can be shown in a simple way solving the Langevin equation in the unidimensional homogeneous stationary case, with null mean flow field, and neglecting turbulent term (i.e. assuming that each particle coincides with the barycenter of the puff); we then set:

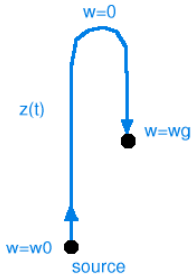

Figure 3.4.: Simple test case: initial velocity w_0 and asymptotic velocity $-w_g$.

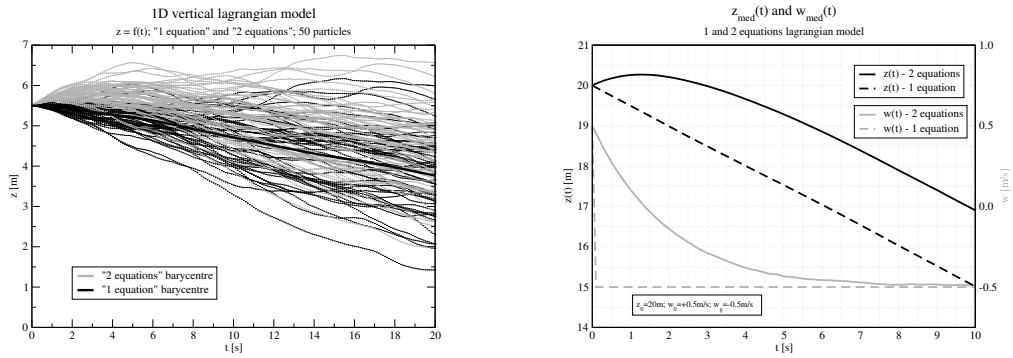

(a) (b)

Figure 3.5.: Comparison between "1-equation" and "2-equations" lagrangian models: a) barycenter trajectory and b) speed in the near field.

$$\begin{cases} dx = udt \\ du = -\frac{u}{T_L}dt \\ x(0) = x_0 \\ u(0) = u_0 \end{cases} . \tag{3.45}$$

In this case the solution can be found analytically and reads:

$$\begin{cases} x = x_0 + u_0 T_L \left[1 - \exp\left(-\frac{t}{T_L}\right)\right] \\ u = u_0 \exp\left(-\frac{t}{T_L}\right) \end{cases} . \tag{3.46}$$

From (3.46) one can derive the position reached by the particle with initial velocity u_0. Actually, the process is asymptotic, therefore the particle never comes to a stop, mathematically; in practice, one can define a relative velocity increment $\varepsilon = \frac{u_0 - u}{u_0}$ below

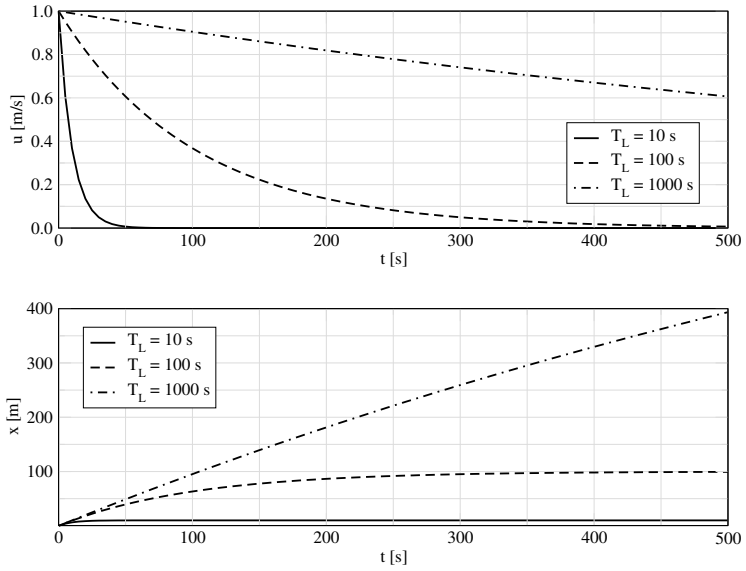

Figure 3.6.: Kinematic interpretation of the role of lagrangian time scale ($u_0 = 1\,m/s$).

which the particle is considered to be halted, at the coordinate:

$$x = x_0 + u_0 T_L \varepsilon. \tag{3.47}$$

Figure 3.6 shows dependence of the particle walk on the lagrangian time: low values of T_L mean that the particle rapidly loses memory of its initial velocity; on the contrary high values of T_L correspond to frictionless situation, i.e. the particle continues to move a longer time (and space).

3.2.6. Skewed turbulence

As explained before, unlike eulerian approach, the lagrangian one can provide the correct value of concentration also for a travel time which is comparable with the integral time scale of turbulence. Lagrangian models seem to be more suitable especially in description of strongly inhomogeneous skewed turbulent flow (Monti and Leuzzi, 1996). Although gaussian turbulence is usually assumed in lagrangian models, under convective conditions vertical tracer transport occurs primarily in updrafts and downdrafts. This phenomenon can be approximated as the sum of two gaussian distributions, one for the updrafts and the other for the downdrafts. There exist several approaches to deal with the turbulent horizontal velocities. The simplest solution is to solve an independent Langevin equation

for all the wind components; however, measurements of wind fluctuations indicate that there exist cross-correlation terms between the individual wind components (Zannetti, 1990). These cross-correlations can be very important near the source but in mesoscale applications the cross-correlations are less important.

Monti and Leuzzi (1996) point out that suitable parametrization for vertical skewed turbulence are necessary for air pollution modelling over complex terrain. Skewed turbulence structure has been therefore included in the lagrangian model developed in present work (chapter 3), in order to account for modification in dispersion processes induced by the presence of orographic obstacles, mainly occurring due to differential heating, as explained in chapter 2. In fact, during daytime atmospheric turbulence within the atmospheric boundary layer originates both from heating of the land surface and from the presence of wind shear; this fact is much more evident when the local approach for the heat balance discussed in section 2.2 is adopted. This leads to the formation of random up-draft and down-draft thermals called eddies. Up-drafts have higher velocities but occupy less area than down-drafts, leading to a skewed vertical velocity distribution (Luhar and Bitter, 1989; Luhar et al., 1996). Transport of pollutants in the atmosphere is dominated horizontally by the mean wind and vertically by turbulence. Hence, when modelling atmospheric dispersion, one often assumes homogeneous turbulence in the horizontal directions, but inhomogeneous in the vertical (depending on height). The details of the transport within the ABL are not so important since the temporal scale of vertical mixing is much shorter than the transport times.

A unique solution for the drift term a can only be given in one-dimensional inhomogeneous flows. The one-dimensional model can be used to account for the inhomogeneity in one direction in isotropic turbulence. Therefore a "2-equations" model with skewed turbulence can be only used along z direction, while the horizontal transport could even be simplified through the "1-equation" formulation (see figure 3.7).

Notice that under stable conditions the assumption of gaussian turbulence is acceptable also for the vertical term; on the other hand, under convective situation vertical turbulence is known to exhibit a skewed PDF (e.g. Baerentsen and Berkowicz, 1984; Thomson, 1987). Here a bi-gaussian distribution is adopted (see Luhar et al., 1996):

$$p_S = A \cdot p_{GA} + B \cdot p_{GB}, \tag{3.48}$$

where the skewed PDF p_S is built by means of two gaussian PDFs ,p_{GA}, for up-drafts and p_{GB}, for down-drafts, each multiplied by a coefficient dependent on the height. These distributions are defined as follows:

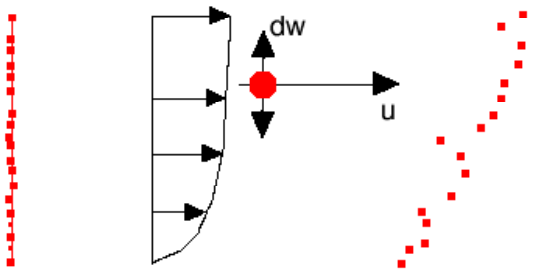

Figure 3.7.: Simplified scheme: fluctuation is accounted for in the vertical direction only.

$$\begin{cases} p_{GA} = \frac{1}{\sqrt{2\pi}\sigma_A} \exp\left[-\frac{(w-W_A)^2}{2\sigma_A^2}\right] \\ p_{GA} = \frac{1}{\sqrt{2\pi}\sigma_B} \exp\left[-\frac{(w+W_B)^2}{2\sigma_B^2}\right] \end{cases} . \tag{3.49}$$

The closures proposed by Luhar et al. (1996) for the quantities appearing in (3.49) read:

$$\begin{cases} W_A = 0.88 \left(\frac{z}{z_i}\right)^{1/3} \left(1 - \frac{z}{z_i}\right) \\ W_B = 0.61 \left(\frac{z}{z_i}\right)^{1/3} \left(1 - \frac{z}{z_i}\right) \end{cases} \tag{3.50}$$

for the mean velocity and

$$\begin{cases} \sigma_A = 1.25 \left[\frac{z}{z_i}\left(1 - \frac{z}{z_i}\right)\right]^{1/3} \\ \sigma_B = 0.61 \left[\frac{z}{z_i}\left(1 - \frac{z}{z_i}\right)\right]^{1/3} \end{cases} \tag{3.51}$$

for velocity fluctuations. Coefficients in equation 3.48 are computed as:

$$\begin{cases} A = \frac{W_B}{W_A + W_B} \\ B = \frac{W_A}{W_A + W_B} \end{cases} . \tag{3.52}$$

The above formulation guarantees a smooth transition from the skewed PDF used for convective conditions to a simple gaussian PDF for stable and neutral atmospheric flows. This avoids discontinuities, as the PDFs (3.49) tend to a gaussian behaviour as the skewness tends to 0 (i.e. $A = B = 0.5$, $W_A = -W_B$, $\sigma_A = \sigma_B$).

3.2.7. Buoyant plume rise

In order to model the rise of an exhaust gas warmer than the surrounding air, Briggs (1975) formulas are often used. These expressions were derived for plume models and it is difficult to make use of them within a lagrangian framework. Therefore, the source height is often replaced by an effective stack height for each puff. In the following, a lagrangian approach to calculate puff rise is presented and briefly discussed. The principles on which the calculation of the puff rise is based are briefly outlined. Mainly, two forces have an effect on a parcel of air: the buoyancy and the air resistance. Additionally, a parcel of air will exchange heat with the surrounding air. An initial velocity w_B, accounting for this phenomenon has to be added to particle speed, as it is done for gravitational term w_G in the opposite verse. First, the buoyancy frequency N and the buoyancy acceleration a_B are defined as follows:

$$N^2 = \beta g \frac{\partial \Theta}{\partial z}, \tag{3.53}$$

$$a_B = \beta g(\theta - \Theta), \tag{3.54}$$

where $\beta = 0.5$ is an experimental coefficient (Heinz and van Dop, 1999), Θ is the external air potential temperature (considered to be constant) and θ the effluent potential temperature (varying along the plume path). The variation with respect to time of the buoyancy force and the consequent variation in vertical velocity is then derived according from the formulation of Heinz and van Dop (1999):

$$da_B = -\frac{k_1}{4T_L} a_B dt - N^2 w dt, \tag{3.55}$$

$$dw_B = a_B dt. \tag{3.56}$$

Thus Langevin equation gains an additional term in the z direction:

$$\begin{cases} dz = wdt \\ dw = adt + a_B dt + bdr \end{cases}. \tag{3.57}$$

(3.57) is solved numerically with an explicit scheme:

$$\begin{cases} a_B^{n+1} = a_B^n - \frac{k_1}{4T_L} a_B^n \Delta t - N^2 w^n \Delta t \\ w_B^{n+1} = a_B^n \Delta t + a^n \Delta t + b^n dr^n \\ z^{n+1} = z^n + w^n \Delta t \end{cases} . \tag{3.58}$$

The initial condition is $B(0) = \beta g(\theta_s - \Theta)$ where θ_s is the temperature at the source. The coefficient k_1 in (3.55) is set equal to 0.8 (Heinz and van Dop, 1999), or to 1 to meet the plume rise formula of Briggs (1975).

According to Monti and Leuzzi (1996), when w_B becomes smaller than the local value of σ_W, the final plume rise is considered to be reached.

3.3. Kernel method

Stochastic particle models simulate the released pollutant by a large number of particles. The estimation of concentration is then obtained by multiplying the number of particles by their mass, and dividing this total mass by the size of the grid box. This way of counting the number of particles in a box is identical to calculating a threedimensional histogram. Histogram estimations in general depend, however, on the choice of the width and the center of the averaging interval, area or volume. To estimate point concentrations in the context of atmospheric dispersion modelling, there are no physical restrictions determining either the center of a numerical averaging volume, or its size. This means that when choosing large averaging volumes, important details might get lost, and the estimation of the concentration density simulated by the particles will be over-smoothed. On the other hand, when choosing small averaging volumes, there is the possibility of having random fluctuations in the number of particles per sampling volume. One would thus try to choose "reasonable" sizes and positions of the averaging volumes. The differences in the resulting concentration predictions can be significant and of the same order of magnitude of the effects which are relevant and, hence, are to be modelled. It should be stressed that this uncertainty only originates from a numerical procedure and doesn't depend on the schematization of the physical process.

As an alternative approach, the density kernel method to estimate concentrations can be adopted. It allows for a reduction of the number of simulated particles required to get the same accuracy (de Haan, 1999). The method relies on the concept of density distributions of different shape which are "added" to the particle's position; hence, the mass associated to the particle is spread out in space. Such a density distribution around the center of mass is called the density kernel and is a continuous function of space. Unlike in the choice

of box size and position, the shape of the kernel and its width as a function of the particle distribution have to be specified. The latter is chosen such that the bias and variance of the concentration estimation are jointly minimized. The number of needed particles is found to be $1 \div 2$ order of magnitude less than the box-counting method. Nevertheless, some problems arise in coping with particularly complex topography, as evidenced in section 4.3.2.

The general kernel density estimator for the concentration C of n given particles of equal mass at positions x_i is:

$$C(\mathrm{x}) = \frac{1}{nh} \sum_{i=1}^{n} K\left(\frac{\mathrm{x} - \mathrm{x}_i}{\chi}\right), \tag{3.59}$$

where χ is the width of the kernel and K is the kernel function, which fulfills the condition $K(\mathrm{x}) \geq 0$ for every x and normalized so that $\int K(\mathrm{x})d\mathrm{x} = 1$; hence C is a density distribution, such that $\int C(\mathrm{x})d\mathrm{x} = 1$. One of the most widely used kernels is the gaussian kernel, characterized by the kernel function

$$K_G = \frac{1}{(2\pi)^{d/2}} \exp\left(-\frac{\mathrm{r}_i^T \mathrm{r}_i}{2\chi^2}\right), \tag{3.60}$$

with $\mathrm{r}_i = \frac{\mathrm{x}-\mathrm{x}_i}{\chi}$ and d denoting the dimension (i.e. $d = 1$ for a 1D model, $d = 2$ for a 2D model, $d = 3$ for a 3D model). The proper choice of the bandwidth h is of greater importance than the choice of the shape of the kernel, since h plays the role of a smoothing parameter: de Haan (1999) examined different types of kernel; but in the present work only the gaussian has been tested.

Also notice that there are several procedures for determining the value of h from the data. The "optimal" bandwidth, according to de Haan (1999), can be found by using the following formulation:

$$\chi = A(K)\sigma n^{-\frac{1}{d+4}}, \tag{3.61}$$

which is valid for a particle distribution $f(\mathrm{x})$ with standard deviation σ. In this case the bandwidth χ itself turns out to depend on the distribution of the data which are to be smoothed. The function $A(K)$ is defined for a gaussian kernel as:

$$A(K_G) = \left(\frac{4}{d+2}\right)^{\frac{1}{d+4}}. \tag{3.62}$$

Therefore, in case of gaussian turbulence, (3.59) can be written in the form:

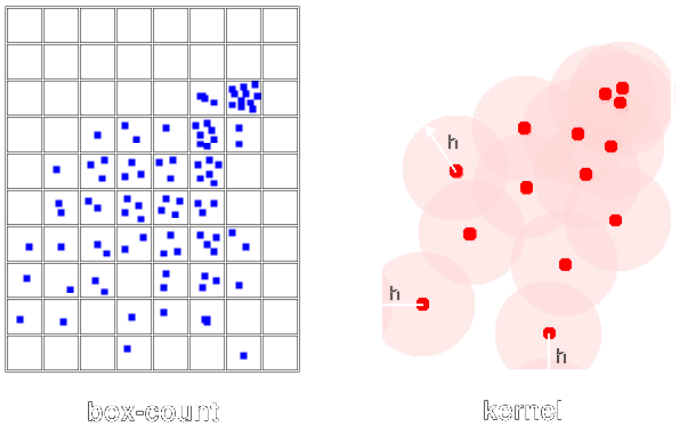

Figure 3.8.: Kernel method and box-count method.

$$C(\mathrm{x}) = \frac{1}{(2\pi)^{\frac{d}{2}} \left[\frac{4}{n(d+2)}\right]^{\frac{1}{d+4}} \sigma n} \sum_{i=1}^{n} \exp\left[-\frac{(\mathrm{x}-\mathrm{x}_i)^T (\mathrm{x}-\mathrm{x}_i)}{2\chi^2}\right]. \tag{3.63}$$

It should be noticed that equation 3.63 is unable to account for a vanishing flux at borders; moreover it uses an unique value for σ and is therefore unable to cope with anisotropic distribution of particles.

For what the first limitation is concerned it should be recalled that the lagrangian method already accounts for null flux, imposing the reflection of the particle at the walls (equation 3.37); in fact the box-count method doesn't need any further information; on the contrary the kernel method needs to "reflect" also the mass associated with the particle: this must prescribed independently from the position of the possible reflection. Equation 3.63 is then modified in present work, introducing source images in order to conserve the total mass in the following form (see figure 3.8):

$$C(\mathrm{x}) = \frac{1}{(2\pi)^{\frac{d}{2}} \left[\frac{4}{n(d+2)}\right]^{\frac{1}{d+4}} \sigma n} \sum_{i=1}^{n} \left[\prod_{k=1}^{d} f_k\left(x, x_i, L_k\right)\right], \tag{3.64}$$

with

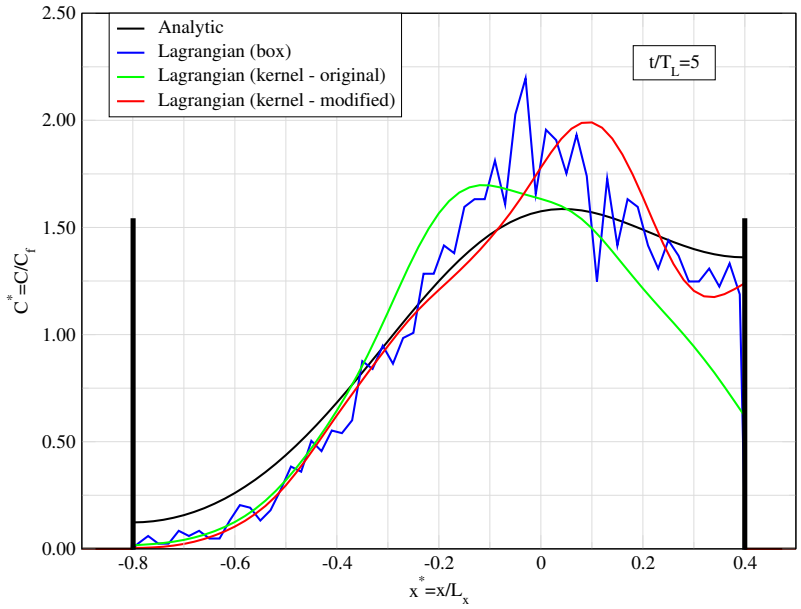

Figure 3.9.: Modified reflection for kernel method; source is located at $x^* = 0$.

$$f_k\left(x, x_i, L_i\right) = \sum_{j=-\infty}^{+\infty} \left\{ \exp\left[-\frac{\left(x_k - x_{k,i} + 2jL_i\right)^2}{2\chi^2} \right] + \exp\left[-\frac{\left(x_k + x_{k,i} + 2jL_i\right)^2}{2\chi^2} \right] \right\}. \tag{3.65}$$

where L_k are the dimensions of the domain (i.e. distance between barriers).

Figures 3.10 and 3.11 show a comparison between the analytical solution of the 1D diffusion equation

$$C(x,t) = \frac{1}{\sqrt{4Kt}} \sum_{j=-\infty}^{+\infty} \left\{ \exp\left[-\frac{\left(x - x_s + 2jL\right)^2}{4Kt} \right] + \exp\left[-\frac{\left(x + x_s + 2jL\right)^2}{4Kt} \right] \right\}, \tag{3.66}$$

and the corresponding lagrangian solutions (box-count and kernel method). Barriers are inserted to check the null flux condition. Two observations can be drawn from the comparison:

- for $t < T_L$ the gaussian solution is quite different, because an incorrect assumption of constant K is used, while for $t \gg T_L$ all the solutions tend to coincide;
- the kernel method shows a smoother solution, even using a number of particles which

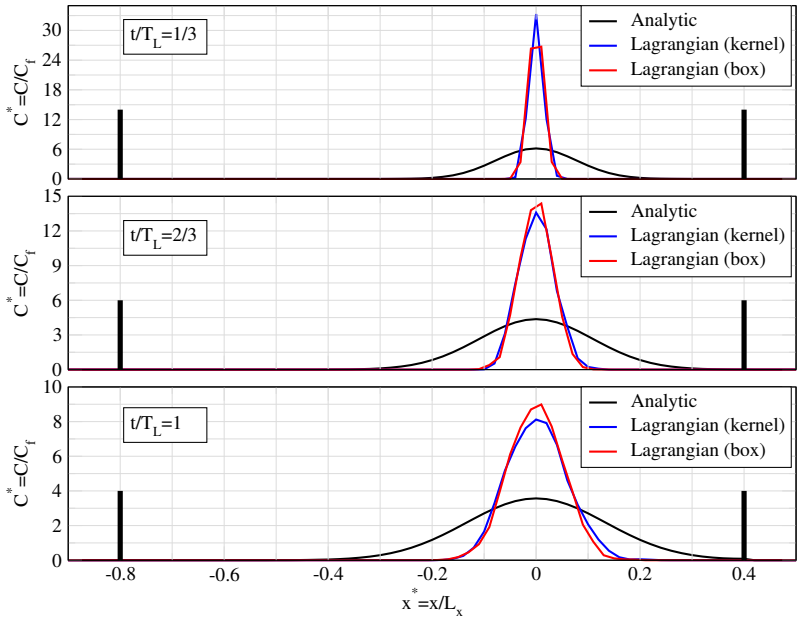

Figure 3.10.: Dispersion within a domain confined within closed boundaries: comparison between analytical solutions (box-count and kernel method) for $t < T_L$. Source is located at $x^* = 0$.

is two orders of magnitude lower than the box-count method (20 vs. 2000) with a strong reduction in computational time.

The second difficulty encountered with the use of (3.63), namely the adoption of a unique value of σ, only arises in complex situations, where the anisotropy of the problem cannot be neglected or where spatial variation of the boundary has different scale in the horizontal and vertical direction, preventing a reasonable estimate of concentration near the ground. This will be the case of the test showed in section 4.3.2.

Finally, we may notice that de Haan (1999) also proposes different bandwidth χ for horizontal and vertical directions; however, this distinction doesn't seem to be related to some physical or geometric property of the domain.

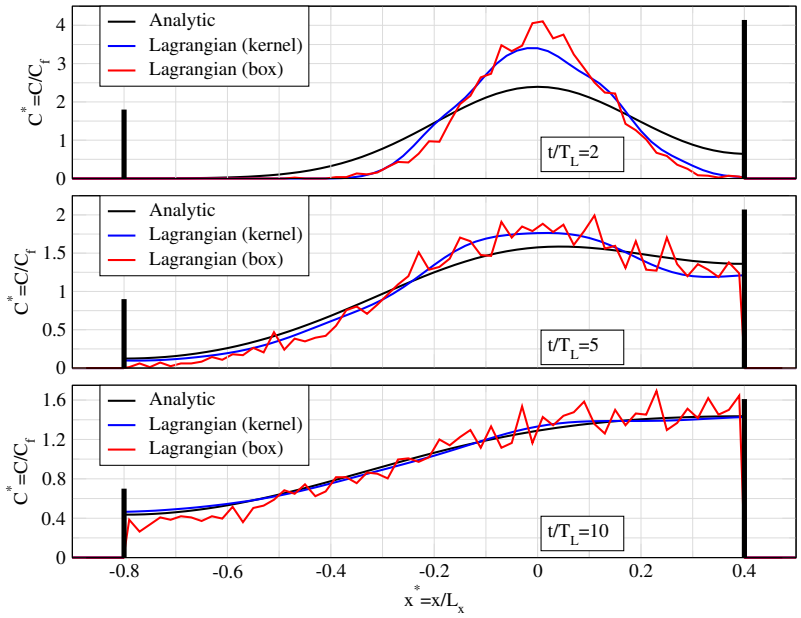

Figure 3.11.: Dispersion within a domain confined within closed boundaries: comparison between analytical solutions (box-count and kernel method) for $t > T_L$. Source is located at $x^* = 0$.

4. A 3D lagrangian model for non uniform terrain

4.1. Formulation

In this chapter a three-dimensional lagrangian model (from here on referred to as LAG3D), is presented. The model has been developed to predict dispersion over complex terrain, based on Thomson (1987) approach discussed in chapter 3. As pointed out by Luhar and Rao (1994), topographical forcing has a strong influence on tracers dispersion; hence, a suitable tool, able to accommodate for this effect, has to be chosen. In particle, like those adopted to individuate the "worst case" (i.e. maximum ground-level concentration), a lagrangian model can be suitable, provided enough meteorological data are available and suitable turbulence closure are introduced (Wilson and Sawford, 1996).

The proposed procedure is applied to an actual situation: the study of the dispersion of pollutant emitted from the incinerator of the town of Bolzano (Northern Italy) on a study area of $14 \times 11\,km$. The aim of the work is not to produce the impact assessment for the plant (therefore detailed data won't be listed), but to verify the performance of the model on a short term simulation and to carefully check its limitations.

Figure 4.1 shows the flowchart of LAG3D. First of all, operational parameters and digital elevation map are introduced (input). Then the main cycle over the hourly input meteorological data starts: flow field is read and turbulence is computed for each cell in the domain (flow and turbulence). For each particle the trajectory is integrated, interpolating eulerian values at the nodes of the cell through which the particle is passing, and accounting for the reflection at the boundary when required (cell, interpolation, walk, reflection). Afterwords concentration in each cell is computed, through box-counting or kernel method. Finally, at the end of the main cycle, output values are spooled on file and color maps of concentration are produced.

4.1.1. Flow field

The program CALMET (see section 2.2.1) is used to calculate the three-dimensional wind field and the parameters related to turbulence, which are needed as meteorological input

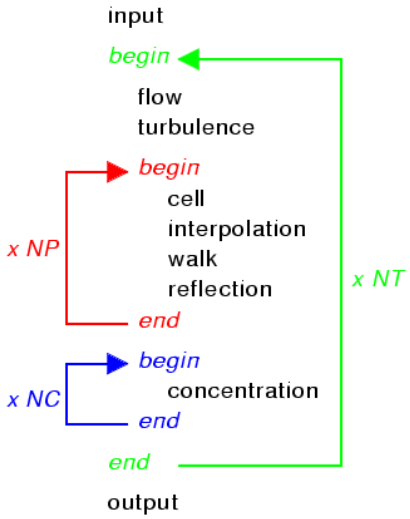

Figure 4.1.: LAG3D flow diagram: NT is the number of hourly input meteorological data, NP is the number of particles, NC is the number of cells.

for the LAG3D model. CALMET works on grid which is regular in the horizontal direction, while a terrain-following vertical coordinate system is adopted. The physical coordinates (x, y, z) are then transformed to compute the coordinates (x, y, z'). The transformed vertical coordinate (figure 4.2) is given by:

$$z' = (z - \eta)\,\frac{H_{top}}{H_{top} - \eta}, \tag{4.1}$$

where $\eta(x, y)$ is the local altitude above sea level and H_{top} is the height of the computational domain (in the present case $2500\,m$). All the quantities varying along the vertical direction are scaled accordingly. Vertical velocity is given by (Ichikawa and Sada, 2002):

$$w(z') = w(z)\frac{H_{top}}{H_{top} - \eta} - \left[\frac{\partial \eta}{\partial x}u(z) + \frac{\partial \eta}{\partial y}v(z)\right]\frac{H_{top}(H_{top} - z)}{(H_{top} - \eta)^2}, \tag{4.2}$$

or, when the local slope is negligible, by:

$$w(z') = w(z)\frac{H_{top}}{H_{top} - \eta}. \tag{4.3}$$

The same procedure is used for mixing height z_i and pressure p (the latter is only needed to compute potential temperature in the plume rise estimate, as shown in section 3.2.7):

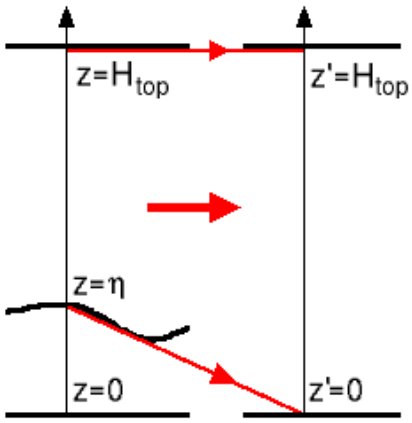

Figure 4.2.: Terrain-following coordinates transformation.

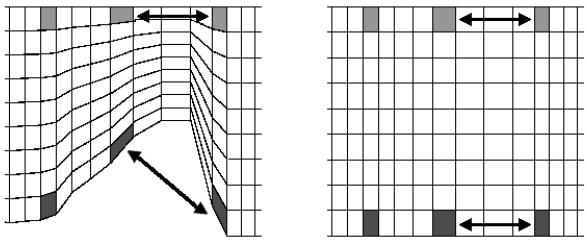

Figure 4.3.: Computed and actual cell concentration in real and vertical stretched coordinates.

$$z_i' = (z_i - \eta)\,\frac{H_{top}}{H_{top} - \eta}, \tag{4.4}$$

$$p(z') \quad = \quad p(z) - \frac{p(z) - p(\eta)}{H_{top} - \eta}\,(z - \eta)\,. \tag{4.5}$$

Furthermore, using terrain following coordinate, also the concentration must be scaled in the following form (see also figure 4.3):

$$C(x, y, z') = C(x, y, z)\frac{H_{top}}{H_{top} - \eta(x, y)}. \tag{4.6}$$

4.1.2. Turbulence parametrization and lagrangian time scale

For turbulence parametrization LAG3D adopts a local eulerian approach, estimating the values of turbulent diffusivity $K_z(x, y, z)$ from the computed profile for each column, according to the method explained in section 2.2. Notice that, using scaled profiles for K_z can improve the adaptation of turbulent diffusivity to topographic variations with respect to a puff-model scheme; in the latter approach orographic factor is only implicit in the previously computed flow field, while the puff isn't modified at each time step by explicit information. On the other hand, the local approach is based on the hypothesis of autosimilar vertical profiles and of slow variation in the horizontal plane, which may not be the case of mountains ridges or steep valleys. The local approach method is adopted in CALMET for all the 2D variables (z_i, L_{MO}, u_*, w_*, stability class) and is also retained in the implementation of LAG3D. Notice, however, that this procedure may lead to a scattered matrix of these quantity; this problem may be solved by smoothing the function with some algorithm (e.g. $1/R^2$ averaging), but this wouldn't obviously add more information with respect to the original one.

When studying dispersion from ground-level sources vertical diffusivity profile in LAG3D is given in the form:

$$K_z(z) = \frac{k u_* z}{\Phi\left(\frac{z}{L_{MO}}\right)}, \tag{4.7}$$

which is rescaled in terrain following coordinates in this form:

$$\begin{aligned} K_z(z') &= [K_z(z) - K_z(\eta)] \frac{H_{top}}{H_{top} - \eta} \cdot \frac{1}{\Phi\left(\frac{z'}{L_{MO}}\right)} \\ &= \frac{H_{top}}{H_{top} - \eta} \cdot \frac{K_z(z) - K_z(\eta)}{\Phi\left[\left(H_{top}\frac{z-\eta}{H_{top}-\eta}\right)\frac{1}{L_{MO}}\right]}. \end{aligned} \tag{4.8}$$

Alternatively equation (3.14), which is valid for the entire ABL, is adopted. K_x and K_y are supposed to be linearly related to K_z, i.e. $K_{x,y} = c_1 K_z$. The coefficient c_1 has a value ranging between $1 \div 2$ and can be used as a calibration parameter. The comparison with the results of the CALPUFF model (section 4.3.3) yields a value of about 1.5; however, this value may change on a different site.

The estimate of the lagrangian time scale is based on equation 3.13; it is then possible to derive the velocity variance as requested in Langevin equations:

$$\sigma_{U,V,W} = \sqrt{\frac{K_{x,y,z}}{T_L}}. \tag{4.9}$$

4.1.3. Operational parameters

Concentration inside each cell is computed at defined time intervals, counting the particles within a cell, through the formula

$$\bar{C} = \frac{N_P M_P}{\Delta x \Delta y \Delta z}, \tag{4.10}$$

where N_P is the number of particles inside the cell of dimension $\Delta x \Delta y \Delta z$, averaged over the time Δt_A, and M_P is the mass carried by each particle. The averaging time is $\Delta t_A = 3600\,s$: this choice also allows one to compare model results with those obtained through CALPUFF (see section 4.3.3), which are provided at hourly intervals. For medium-range transport distances, the concentration at the center of the grid cell is assumed to be representative for the entire grid cell. In order to compute statistically acceptable concentrations, a large number of particles is released in the flow field at the source location: in particular, for the kernel method the rate is of $1/30\,p/s$ (2880 particles per day) while for the box-count method it is much higher, namely $1\,p/s$ (86400 particles per day): in fact, in the latter method, the number of particles must be large enough so that the result is statistically acceptable. The short release time is chosen in order to achieve a better accuracy. In fact, when simulating a continuous release a certain number of particle have to be left into the flow field, with a time step satisfying the relationship

$$\Delta t_R = U_F \Delta x < L_P, \tag{4.11}$$

where Δx is the travel distance of the barycenter of the particles at each release step, U_F is the mean velocity of the flow field at the release point, Δt_R is the release time step and finally L_P represents the characteristic dimension of the released puff after Δt_R. Furthermore, release time Δt_R and averaging time Δt_A are in some way related: increasing the first implies an increase of the second to avoid too much scattered results for the concentration.

A variable integration time step dt is adopted, namely $T_L/20$ for $t < 5T_L$ and $T_L/5$ for larger times beyond the near range transport. Moreover, both T_L and dt are allowed to vary within upper and lower bounds to avoid numerical problems and an excessive slowing down of the algorithm; the following ranges are adopted:

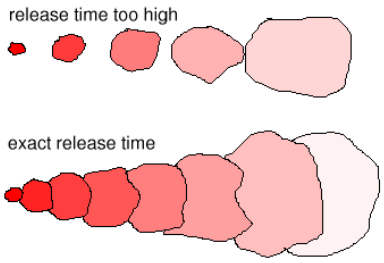

Figure 4.4.: Release interval: high lag time in release can lead to inaccurate concentration prediction.

$$5\,s < T_L < 3600\,s, \tag{4.12}$$

$$dt > 0.5\,s. \tag{4.13}$$

A non-gaussian scheme for turbulence, like that defined (3.51), is adopted. As far as the boundary conditions, each particle is assumed to be perfectly reflected at the earth's surface according to the local slope (i.e. accounting for it in the transformed coordinate system in which vertical velocity is modified); when a particle leaves the domain it is no more reinserted; this approximation can be only considered to be valid if most of the impact area is inside the computational area (as in the examples reported in section 4.3); otherwise, model prediction would probably underestimate the actual concentration due to mass loss.

4.2. Input data

Orography in the study area is characterized by mountain ridges which reach the height of $1600\,m$ above sea level, while the valley floor is nearly horizontal ($250\,m\,a.s.l$). South of Bolzano the Adige Valley is wide (see picture 4.6); on the Northern part of the town three valleys join: Val Sarentino, which is very narrow and steep, in the N direction, Val d'Adige and Val d'Isarco in the NW and NE direction, respectively (see figure 4.7). A digital elevation map with $100 \times 100\,m$ resolution over a domain of $14 \times 11\,km$ centered on the source is adopted. The extension of the domain is chosen on the basis of the spatial scale of dispersion process from a point source. In the vertical direction 17 unequally spaced layers, are used: spacing is finer near the surface and becomes coarser with height.

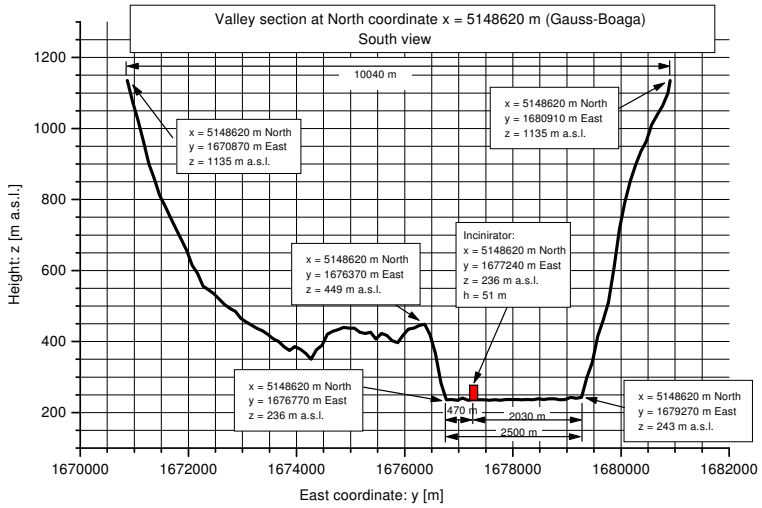

Figure 4.5.: South view of the section of the Adige Valley where the source is located.

In terrain following coordinates $z'\,[m]$ the heights of the layers extend from 0 to $2500\,m$.

Routine weather data are available for 5 stations inside the domain, operated by the local Environmental Protection Agency (APPA-Bolzano). Measured quantities are wind speed and direction, temperature, pressure, rainfall. Through the CALMET modelling system the diagnostic 3D flow field is obtained from these observations.

Particles simulating the incinerator emissions are released from a stack $51\,m$ high, with a temperature of $140°C$ and an initial vertical velocity of $5\,m/s$; the plume rise is computed according to the method explained in section 3.2.7. Tracer is considered as gaseous and passive in order to simplify cross-validation of the model. All tests are performed under the hypothesis of unitary emission ($1\,g/s$). Actual results can be then obtained scaling emission rates and concentrations accordingly.

Figure 4.6.: North view of the Adige Valley.

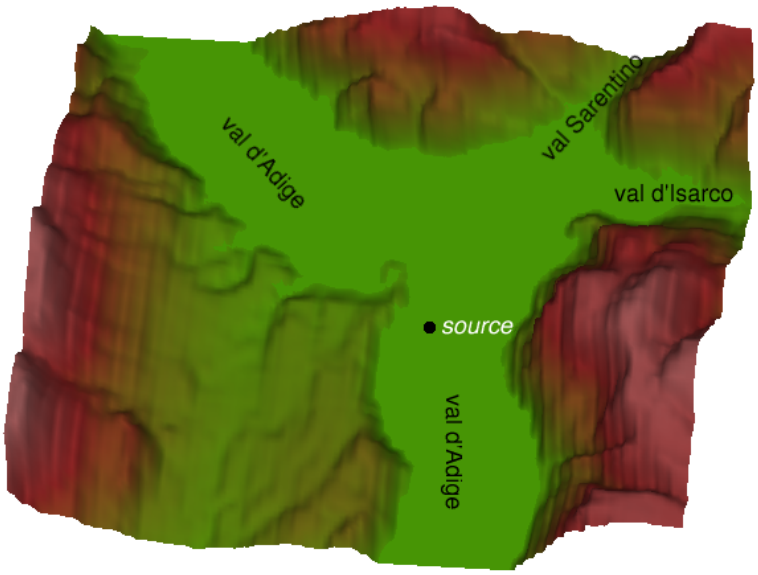

Figure 4.7.: Orography of the study area and source location.

4.3. Simulations

4.3.1. Results

Due to high CPU time consumption (simulation time roughly corresponds to the actual time for studied the domain), only a few days are simulated. Figures 4.8, 4.9 and 4.10 show the position of the emitted particles at selected times. For the sake of clarity, snapshots of a simulation with a low number of particles are shown. The plan view reported in figure 4.8 clearly indicates that due to wind rotation the tracer is channelled along different valleys. Vertical sections referring to night-time simulations show a stable stratification which confines the pollutant within a layer whose thickness is less than $200\,m$. In fact, in the stable case eddy vertical motion is limited by stratification and the eddy cannot extend over the entire ABL. On the contrary, in the morning, when solar heating starts, the mixing layer increases and pollutant is spread over a wider area (figure 4.9). This becomes even more evident in the afternoon (figure 4.10), when vertical mixing spans over the whole vertical domain and concentration decreases considerably; this is also shown in figure 4.11, where a comparison of a vertical concentration profiles under stable and unstable condition is reported.

In figures 4.12, 4.13 and 4.14 hourly ground level concentration maps of the same simulation run are given. The first plot refers to the case of high stability; hence, the plume impact area at ground is limited; the second plot highlights the modification of the impact area due to wind direction rotation; the last plot displays a more scattered pattern, which is characteristic of convective conditions: the last two snapshots entirely fall in the lower part of the color scale, meaning that ground level concentration is reduced of more than one order of magnitude with respect to the maximum (see also figure 4.11).

(a 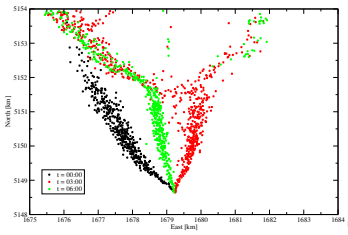
(b 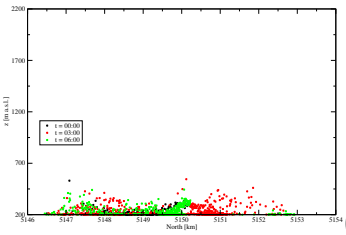
(c 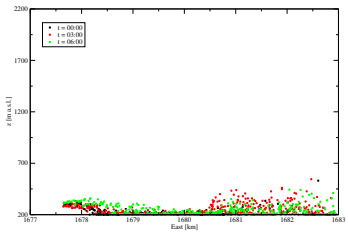

Figure 4.8.: Particle positions at $0\,AM$, $3\,AM$, $06\,A$ on 24 May 2000: a) plan view, b) East and c) South view of the vertical section to which the source belongs.

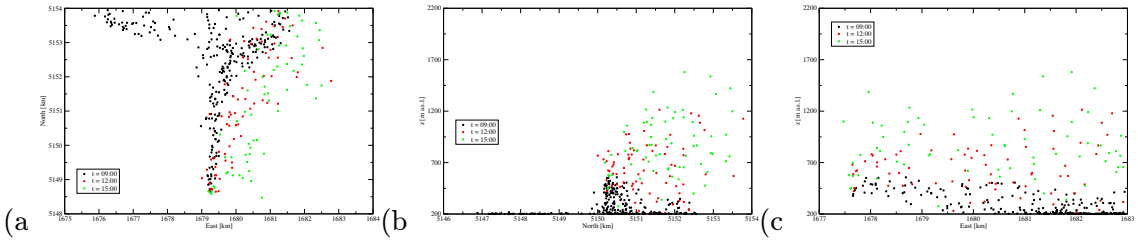

Figure 4.9.: Particle positions 9 AM, 12 AM, 3 PM on 24 May 2000: a) plan view, b) East and c) South view of the vertical section to which the source belongs.

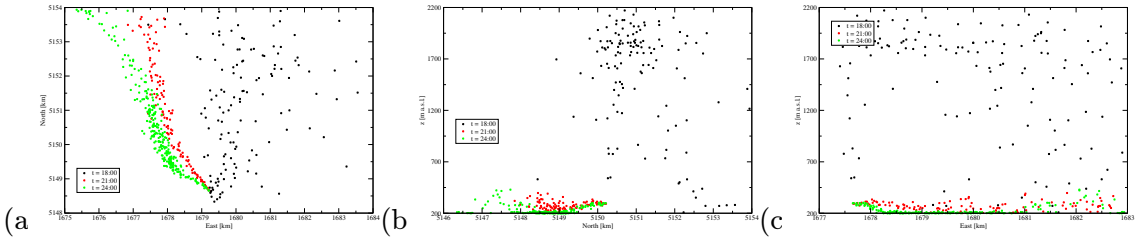

Figure 4.10.: Particle positions at 6 PM, 9 PM, 12 PM on 24 May 2000: a) plan view, b) East and c) South view of the vertical section to which the source belongs.

4.3.2. Considerations on kernel method

Kernel density estimation method (section 3.3) is used to obtain a smooth concentration distribution of tracer gases. In some cases model results obtained through the box-count method and the kernel method show a substantial disagreement. In fact, using the kernel method problems arise when wind direction rotates and air mass is channeled differently. The example reported in figure 4.15 shows non realistic behaviour of the method when using vertical terrain following coordinates. In fact when wind rotates from direction NW to N both the valleys indicated by arrows "1" and "2" are covered by tracer. However, in the transformed coordinate system there is not a barrier between cells (see also figure 4.3); hence, interpolation tends to smooth concentration field, as clearly displayed by figures 4.17a-b.

Introducing different value for the bandwidth χ (greater in the vertical direction and smaller in the horizontal one) could partially solve the above problem, but would cause the method to loose efficiency since in this case a higher number of particles is necessary to cover

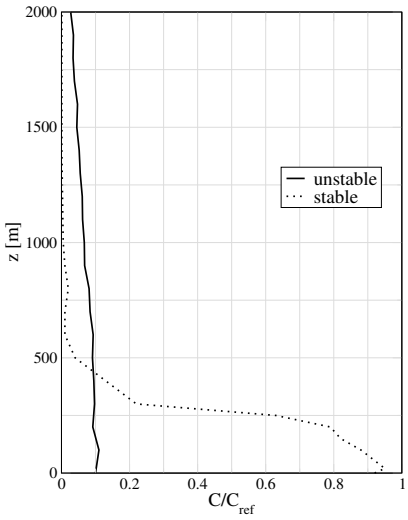

Figure 4.11.: Vertical profile under stable and unstable atmospheric conditions, about 1 km downwind of the source location.

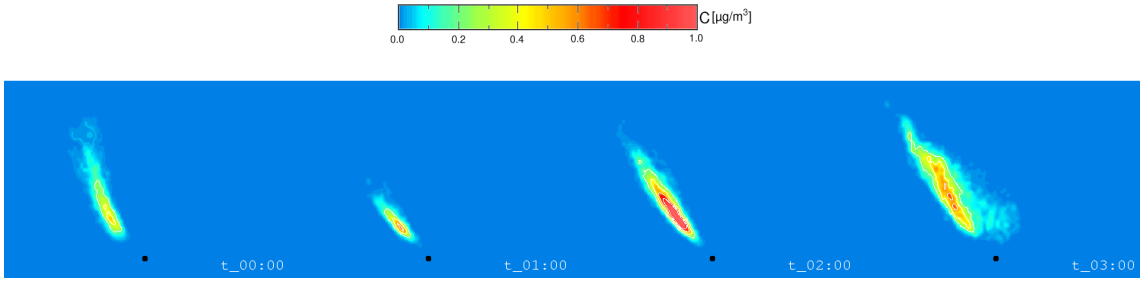

Figure 4.12.: Predicted ground level concentrations, hourly snapshots at 0, 1, 2, 3 AM, 24 May 2000.

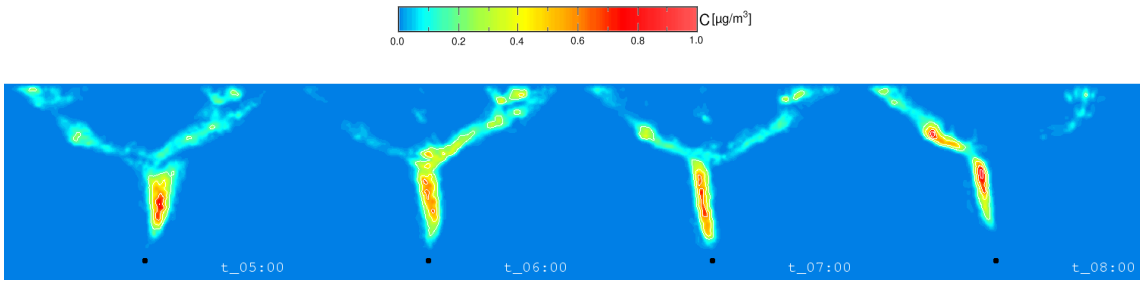

Figure 4.13.: Predicted ground level concentrations, hourly snapshots at 5, 6, 7, 8 AM, 24 May 2000.

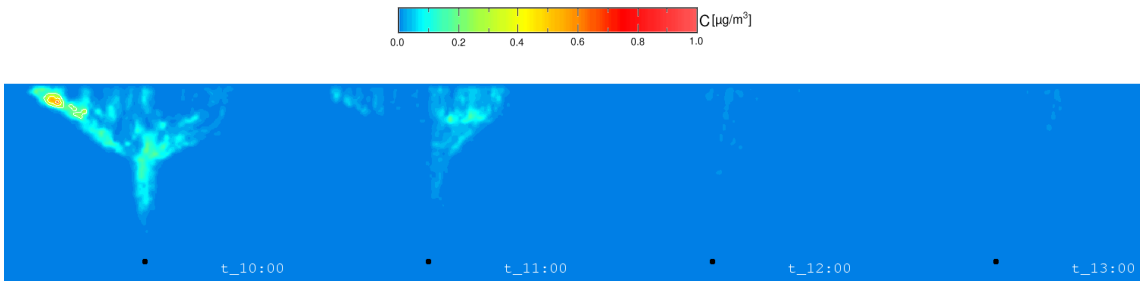

Figure 4.14.: Predicted ground level concentrations, hourly snapshots at 10, 11, 12 AM and 1 PM, 24 May 2000.

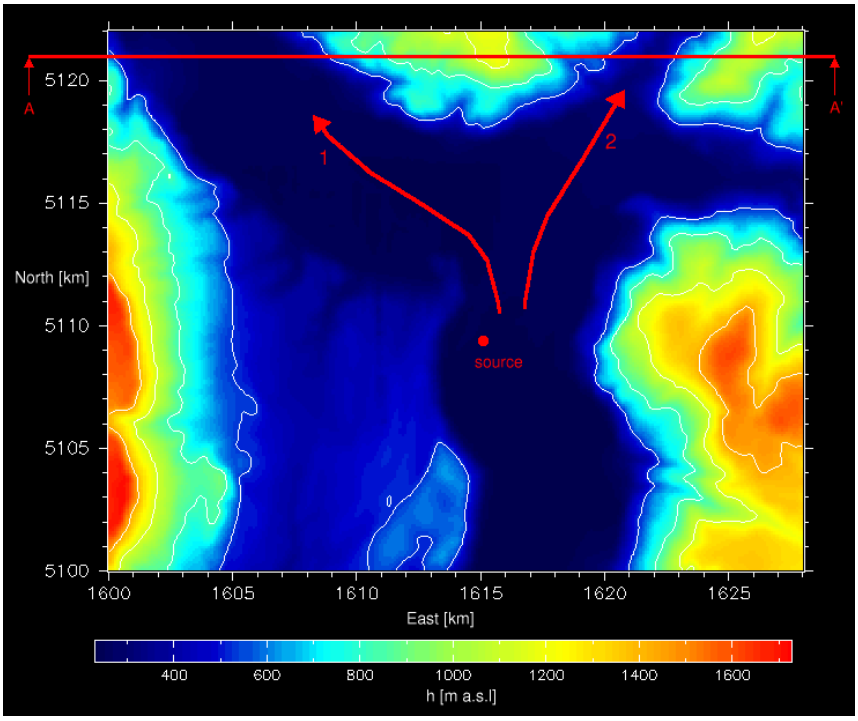

Figure 4.15.: Digital elevation map of the study area and section AA' in which kernel method is tested.

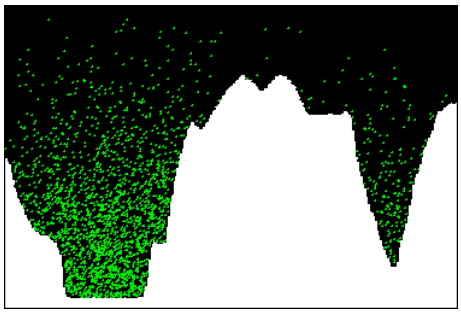

Figure 4.16.: South view of vertical section AA' reported in figure 4.15.

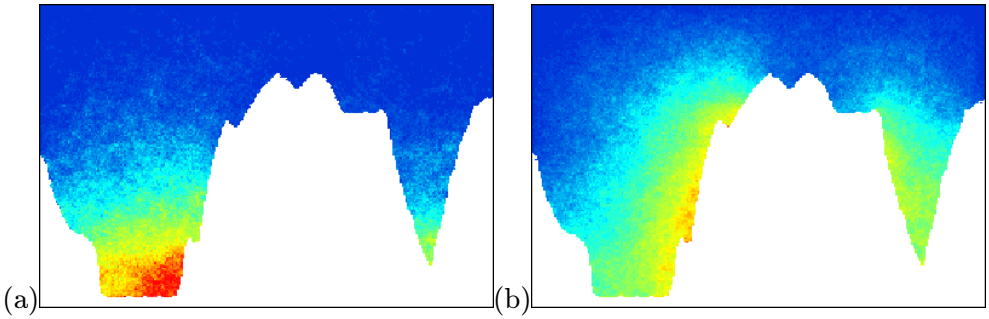

Figure 4.17.: Relative color scale concentration map (red=high, blue=low) relative to snapshot 4.16: a) box-count and b) kernel method.

the entire computational domain with an acceptable resolution. The above considerations seem to suggest that the kernel method would probably perform better in a flat uniform terrain case. As a conclusion the kernel method is not adopted in the final revision of LAG3D.

4.3.3. Comparison between CALPUFF and LAG3D

In order to test the results of LAG3D simulations, the CALPUFF (Scire et al., 2000) modelling system has been used . This software is made available by EarthTech Inc. It uses CALMET's produced hourly wind and temperature fields on a three-dimensional gridded domain from routine weather data. Further parameters as mixing height, stability class, friction velocity, from which dispersion properties needed for the CALPUFF module are derived from CALMET. CALPUFF is a non-steady-state eulero-lagrangian puff dispersion model accounting for time- and space-varying meteorological conditions. The model simulates emission of material from modeled sources, advection and diffusion, as well as removal

and chemical transformation processes (nitrogen oxides and sulfured oxides). The output from CALPUFF consist of hourly averaged concentrations and deposition fluxes. This program is applicable to complex terrain, both for long range transport distances as well as for short to intermediate distances. The user-defined grid size allows for high-resolution simulation of episodes as well as for runs of one year or more with a one-hour time step for environmental impact assessments, and studies of air quality and pollutant transport on regional scales.

Puff modelling approach represents a continuous plume as a number of packets carrying each discrete mass of pollutant material. The puff is advected starting from the source along the streamlines, evolving in size and strength (dependent on turbulence characteristics of the atmosphere in which the pollutant is released and transported); the integration of trajectory is done numerically, once the flow field is known, at given sampling steps. The total concentration at a receptor is the sum of the contributions of all nearby puffs averaged for all sampling steps within the basic time step. The basic equation for the contribution of each puff at any receptor location reads:

$$C = \frac{2M}{(2\pi)^{3/2}\sigma_x\sigma_y\sigma_z} \exp\left(-\frac{d_x^2}{2\sigma_x^2}\right) \exp\left(-\frac{d_y^2}{2\sigma_y^2}\right) \sum_{n=-\infty}^{\infty} \exp\left[-\frac{(H_e + 2nh)^2}{2\sigma_z^2}\right], \tag{4.14}$$

where C is the ground-level concentration, M is the pollutant mass in the puff, $\sigma_{x,y,z}$ are the standard deviation of the gaussian distribution in the along-wind, cross-wind and vertical direction, $d_{x,y}$ are the distances from the puff center to the receptor in the along- and cross-wind direction respectively, H_e is the effective height above the ground of the puff center, h is the mixed-layer height. The summation in the vertical term accounts for multiple reflections both at the mixing height and the ground. In general, puffs within the convective boundary layer meet this criterion within a few hours after release. Integrating over the distance of puff travel, $\Delta s = \sqrt{\Delta x^2 + \Delta y^2 + \Delta z^2}$, during the sampling step Δt yields the time average concentration at ground $\bar{C}$:

$$\bar{C} = \frac{1}{\Delta s} \int_{s_0}^{s_0+\Delta s} C(s) ds, \tag{4.15}$$

where s_0 is the position along the s coordinate which follows the streamlines, at the beginning of the sampling step. For $C(s)$ equation 4.14 is used in computing the contribution to concentration of each puff, whose barycenter is advected in a lagrangian scheme. Both distances $d_{x,y}$ and spread intensities $\sigma_{x,y,z}$ are a function of stability and vary along the s coordinate; the latter follow a law which is analogous to the classic one given in Briggs

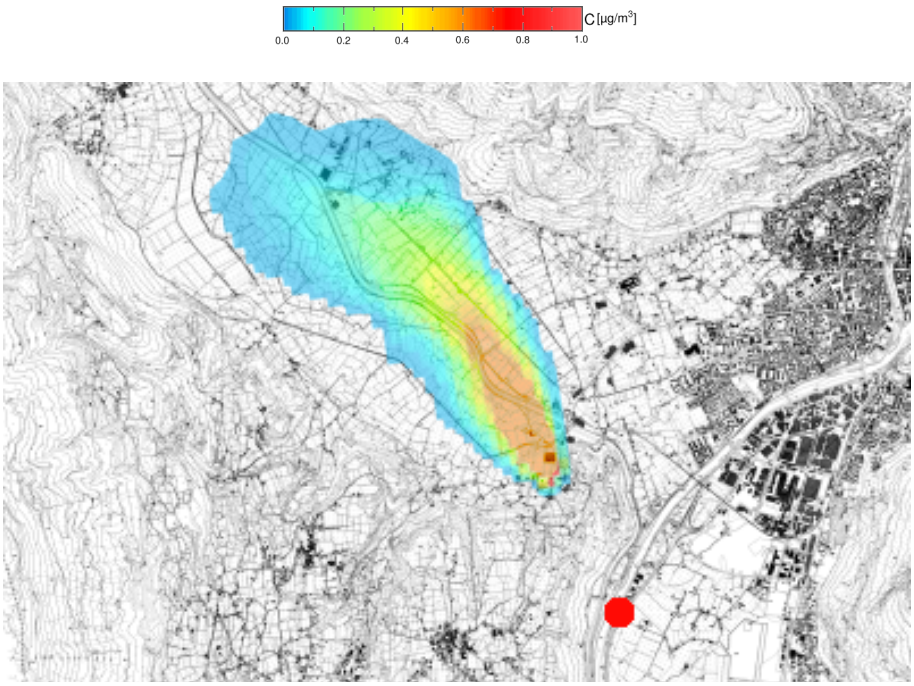

Figure 4.18.: Ground level concentration at $3\,AM$, 24 May 2000, as predicted by CALPUFF.

(1973).

The main limitation of this approach is that it only accounts indirectly for the modification of turbulence structure due to orographic factors. In fact, the only information on topographic variation is fed through the flow field produced by CALMET. In fact it doesn't compute the vertical profile of eddy diffusivity, nor the diffusive module CALPUFF does, as the latter uses a different approach in calculating pollutant dispersion. Being CALPUFF a puff eulero-lagrangian model, only the barycenter of the puff is integrated in a lagrangian (deterministic) view , while diffusion around it is simulated increasing the variance of the puff itself as a function of the downwind distance along the followed streamline. In other words, each released puff follows the streamlines modified by the presence of mountains, but its spread rate is not modified by them; in fact, $\sigma_{x,y,z}$ are computed as in the case of flat uniform terrain and therefore depend on stability classes which are quite similar over the domain at a given time (notice that a quite different procedure has been discussed in section 2.2.3). On the contrary, the present lagrangian method directly accounts for local variations of turbulent diffusivity. Indeed, difference only seems to be significant in case of very narrow valleys with strong difference in exposure to sunshine, or over very steep

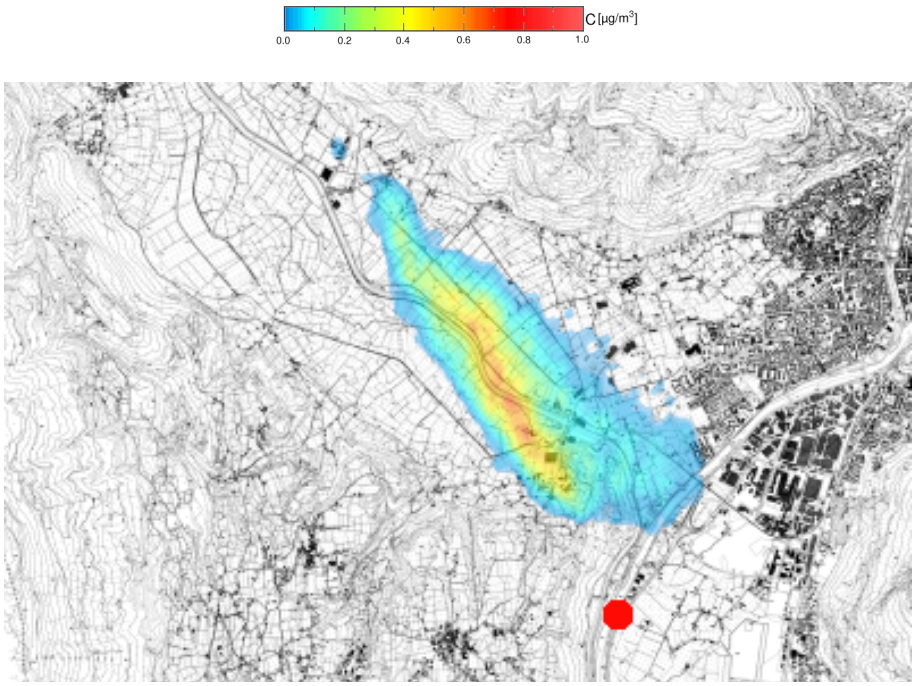

Figure 4.19.: Ground level concentration at 3 AM, 24 May 2000, as predicted by LAG3D.

slopes; notice that in this case also the flow field prediction obtained through CALMET cannot be considered as reliable.

In the test the largest discrepancies between the model results are found when the flow is channelled in the narrow valley Northern of the town of Bolzano (Val Sarentino), along the direction displayed by arrow "2" in figure 4.15. In the other cases concentration predicted by LAG3D and CALPUFF are more similar (see for example figures 4.18 and 4.19).

In figure 4.20 the location of maximum concentration values obtained with CALPUFF and LAG3D for a 1 day test simulation are reported; furthermore, in table 4.1 the corresponding concentration values are listed. While maximum positions agree quite well, concentration values show a different behaviour. Qualitatively one can deduce how LAG3D leads to slightly larger values under stable conditions (mainly during night-time), but considerably smaller values of concentration with respect to CALPUFF in convective conditions.

Table 4.1.: Ratio between hourly concentration calculated with CALPUFF (C_C) and with LAG3D (C_L) for 24 May 2000 simulation.

t	C_C/C_L	t	C_C/C_L	t	C_C/C_L	t	C_C/C_L
00	0.95	06	1.03	12	2.23	18	2.61
01	0.85	07	0.84	13	3.68	19	2.02
02	0.77	08	1.10	14	4.52	20	1.76
03	0.75	09	0.93	15	2.89	21	1.63
04	0.81	10	1.56	16	3.20	22	0.93
05	0.69	11	1.86	17	2.25	23	0.89

4.3.4. Model limitations

The major limitation of LAG3D lies in the high CPU time requirement. Simulation time for a point source over a domain of about $100\,km^2$ (local scale) nearly coincides with the actual time on a $2 \times 2\,GHz$ workstation; over such an extended domain only short term simulations are thus feasible; therefore LAG3D is only suitable, for example, for the investigation of "worst case" impact or for particular meteorological conditions in which eulerian classical method could fail (e.g. strong spatial and time gradients in turbulence field). Anyway, optimization of the algorithm would probably speed up the program.

The estimate of more efficient convective vertical mixing with respect to CALPUFF model is probably due to the fact that different exposure to sunshine in valley is taken in consideration. Moreover, the vertical profile of skewed turbulence is adapted to complex terrain, but its structure could change because of different spatial distribution of updrafts and downdrafts.

A further problem resides in the choice of cell dimension in relation to the number of particles. In fact wider cells tend to smooth the concentration field because the average is performed on a more extended volume, while finer gridding leads to scattered patterns which can only be avoided using a higher number of particles; no absolute rule can be therefore given for establishing the correct cell dimension. The kernel method would be a good solution because it isn't based on a gridded system. However, as shown in section 4.3.2, this method has some limitations and would need further development for complex terrain simulations. Moreover the near field dispersion in the vicinity of the source location should use finer grid spacing, in order to obtain the correct cell averaged concentration. Different sampling grids would ensure a more correct estimate of the cell-averaged concentration impact even for grid cells in the vicinity of the source location.

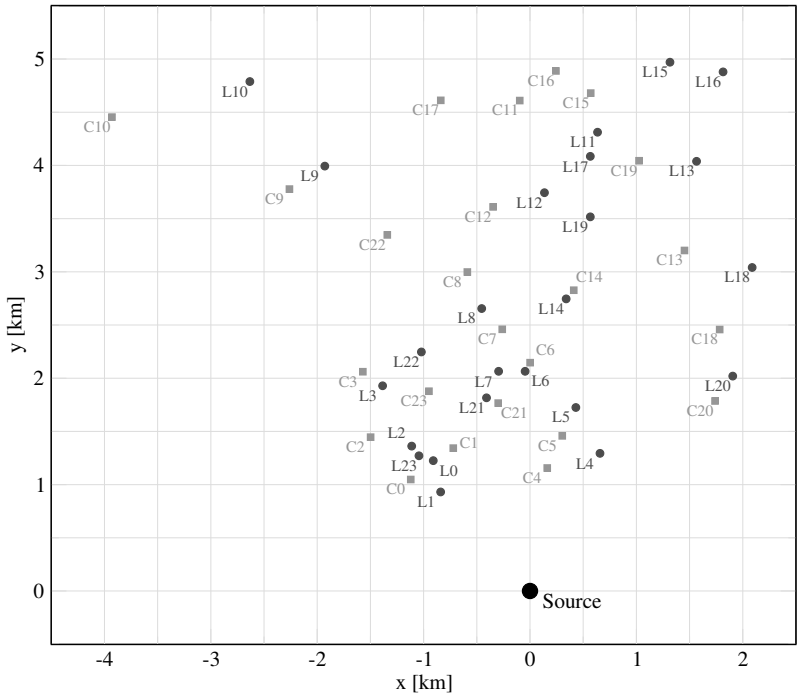

Figure 4.20.: Position of ground level maximum concentration for 24 May 2000 simulation, as obtained using CALPUFF (acronym starting with "C") and LAG3D (acronym starting with "L").

The same uncertainty in the estimate of concentration field is connected to average time Δt_A, but in this case kernel method wouldn't help so much. Obviously a longer time-average smooths the concentration values, while the use of shorter release time steps determines the occurrence of irregular spots. Anyway, the choice of Δt_A is anyway mainly imposed by the aim of the simulation, like in the case of the comparison of resulting concentration with law limits ($1 - 3 - 8 - 24\,h$ averages).

Part II.

Dispersion in urban areas

5. Theoretical framework on traffic derived pollution

5.1. Introduction

Dispersion in urban areas is an issue affecting human health and and air quality, related to industrial sites and builtup areas. In this chapter the focus will be on traffic derived pollution. Evaluation of atmospheric pollution in urban areas is defined starting from source classification (emission type and geometry) as well as from physical characteristics of the domain in which the dispersion process is acting, that is ground roughness, wind field, temperature and atmospheric stability.

Strictly speaking, the conventional methods to describe the characteristics of turbulent exchange of momentum, heat and mass, as developed for flat, smooth, homogeneous surfaces, cannot be applied to the urban boundary layer. Due to the lack of better knowledge dispersion and flow-models still apply the semi-empirical Monin-Obukhov similarity framework (see section 1.2.1) for the parameterization of the urban boundary layer. Therefore, present models' calculations are normally based on simplified methods. For modelling purposes it would be important to know the complex structure of the turbulent characteristics above and inside urban areas, also in comparison to the better known values of other surfaces types.

The properties of urban surfaces strongly affect the local atmosphere. Both aerodynamic roughness and emission of thermal energy act on the wind field. In the lower part of atmospheric boundary layer which is disturbed by built-up zones, the so called urban canopy layer, high levels of turbulence result with respect to rural areas, caused by the presence of buildings, along with thermal convection cells due to the heat island effect.

Pollution sources can be classified on the basis of their emission height, their extension and their emission rate in time. Ground sources are typically represented by vehicle emissions in roads, while elevated sources can be related to stacks or chimneys (domestic heating).

Applications in builtup areas frequently concern the behaviour of emissions from vehicles

representing low level sources, but the question of higher level sources (e.g. domestic heating emissions) can be treated with the same approach. The basic issue concerns the interaction of the obstacles (buildings) with the above boundary layer flow, as well as with the flow field induced within the buildings and, consequently, the effects on diffusion and transport processes. Numerical models can help us in the prediction of dispersion and the subsequent concentration at any location inside the domain of interest, if they are enough resolved for estimating air quality and assessing the impact for human health at a relatively small scale (Robins and MacDonald, 2001).

The dispersion process is not only dependent on source type, but also on the characteristics of turbulence. In fact, the evolution of emitted pollutants has to be related to the vortexes characterizing the air volume in which the pollutant is introduced. If the vortex dimension characterizing the emission is bigger than the one characterizing the atmosphere around, the dilution process is very rapid and efficient; on the other hand, when the vortex dimension of the emission is smaller, the advective transport is predominant over the turbulent diffusion process, thus giving higher concentration.

5.2. Characterization of urban climate

5.2.1. Time and space scales in the urban environment

The time scales of pollution events in urban areas are determined by their typical time evolution and by the geometric scale forcing. Although large-scale weather patterns govern the local conditions, the boundary layer, characteristic for local conditions, changes the micro-climate (see table 5.1). Whether the synoptic scale or the micro-scale is dominant depends mainly on synoptic flow pattern. For instance, in case of synoptic flow pattern (characterized by strong winds, clouds and/or precipitation), the large-scale weather conditions are dominant; vice versa, in calm conditions and with cloudless weather, the local conditions will prevail.

Table 5.1.: Atmospheric motion scales and their ranges after Oke (1987).

Scale	Range
Micro-scale	$10^{-2} \div 10^{3} m$
Local scale	$10^{2} \div 5 \cdot 10^{4} m$
Meso-scale	$10^{4} \div 2 \cdot 10^{5} m$
Global scale	$10^{5} \div 10^{8} m$

Atmospheric variables are influenced by many inter-connected factors. For example, the visibility is influenced at a synoptic scale by atmospheric moisture and at a local scale by precipitation and pollutant concentration. Strong interactions occur at local scale: local vertical and horizontal temperature profiles affect the wind distribution, which in turn affects transport and diffusion. The wind is the synoptic factor that has the most important influence over the local scale factors; its dispersive effect is then enhanced by the difference in structure between the urban and rural environment.

Human exposition to traffic derived pollution can be related to three diffusion scale lengths: the near field ($< 0.1\,km$), the middle field ($0.1 \div 10\,km$) and the far field ($10 \div 1000\,km$), in other words, the "street scale", the "urban scale" and the "regional scale", respectively. Direct exposition to primary pollutants has to be studied mainly in the near field and middle field. At the urban scale also secondary pollutants should be taken into account. In the far field traffic contribution to global pollution is hardly recognizable from other sources.

Determining the flow and turbulence field just inside the street is a relevant issue; many authors have dealt with this problem (see for example the review by Robins and MacDonald, 2001), coming to the conclusion that near the ground dispersion processes inside an urban fabric are more related to source strength and vehicle induced turbulence than to wind speed and atmospheric stability. At a given location, air pollution from sources at each of the scales will affect the local pollutant concentration levels. Although it is not generally possible to decompose measured concentrations into individual contributions, one can observe that concentration fluctuation time scales are generally of the order of seconds for micro-scale sources, minutes for neighbourhood scale sources and hours for urban scale sources.

On the other hand, studies in open field near motorways performed by Sedefian et al. (1981) and Eskridge and Rao (1983) reveal that dispersion in the near field is strongly related to car speed. The same conclusion is drawn by Eskridge et al. (1991) who analyzed wind speed data and turbulence data and found that atmospheric stability (i.e. turbulence induced by solar forcing) is not dominant close to the source.

5.2.2. The structure of the urban boundary layer

The interaction between this heterogeneous urban surface and the atmosphere modifies the surface layer. At the rural-urban interface, an internal boundary layer is formed, the urban boundary layer (UBL). If the considered site is far enough from this transitional region, the former rural boundary layer is completely replaced by the UBL. Within the

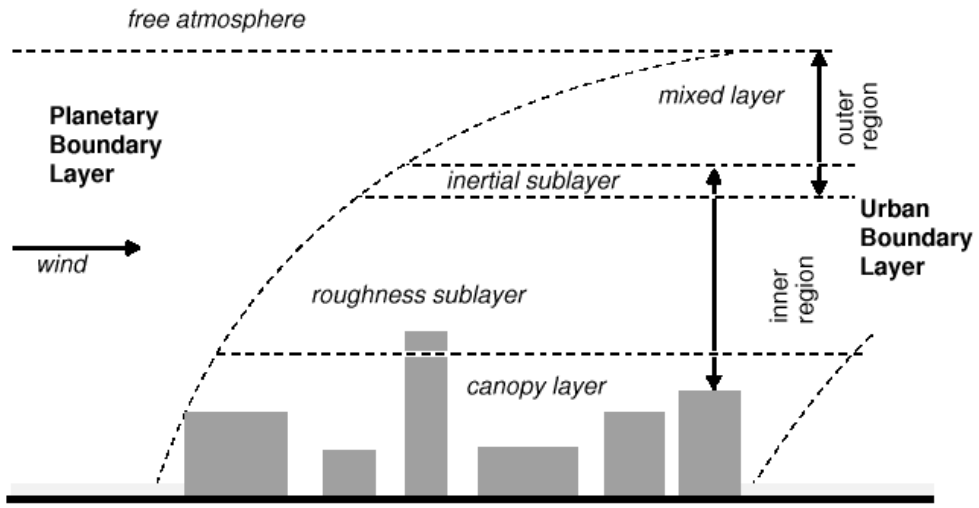

Figure 5.1.: Urban boundary layer over cities, after Oke (1987).

UBL the roughness sublayer (RS) and the canopy layer (CL) are considerably extended as compared to their rural counterparts, whereas the inertial sublayer is reduced or may even vanish. Figure 5.1 shows the vertical structure of an urban boundary layer, after Oke (1987).

Strictly speaking, the conventional methods to describe the characteristics of turbulent exchange of momentum, heat and mass, as developed for smooth, homogeneous surfaces, cannot be applied to the urban boundary layer. However, dispersion- and flow-models still apply the semi-empirical Monin-Obukhov similarity framework for the parameterization of the urban boundary layer.

The friction velocity, the scaling velocity for mean velocities and turbulence intensities are functions of the fetch from the edge of the roughness. As the UBL deepens, the friction velocity tends to the limit value corresponding to a fully developed atmospheric boundary layer above the modified surface roughness. There is a transition layer between the internal boundary layer and the external flow. Conditions in the external flow are not modified directly by the new surface, although, in general, there will be an overall displacement of the flow due to changes in the mass flux in the internal boundary layer (see section 5.3.5).

5.2.3. Atmospheric stability in urban areas

In rural zones, with fair weather conditions, a diurnal cycle of the vertical temperature gradient can be observed (see section 2.1.1), to which stability class can be associated. Nocturnal cooling induces a temperature inversion which is dissolved at sunrise. The mixing height increases from very small values to a maximum in the early afternoon. In urban areas this behaviour is modified by heat sources which change the heat balance at the surface. Industries, traffic and domestic heating act as heat sources along as thermal accumulation bodies, while the different surface type (asphalt, concrete) with respect to rural zones, alters evaporation capacity. Moreover suspended particles in the atmosphere, especially in very polluted areas, affect the incoming radiation pattern, because of scattering of solar beams and absorption phenomena.

These effects influence the temperature inversion strength and extension. In fact, inside the urban canopy layer, the overall difference of temperature ranging between $2 \div 3\,^{\circ}C$ during day time and between $5 \div 6\,^{\circ}C$ during night time determines the so-called urban heat island, which can reach the height of the "natural" thermal inversion.

5.3. Flow field in urban areas

Being an urban area characterized by elevated roughness, the flow field inside is characterized by instability and inhomogeneity. It should be pointed out that modelling of urban flow and dispersion should cope with the fact that the layer of interest (where we live) is inside the roughness and that pollution sources are located within it as well; dispersion processes are affected consequently. Inside the obstructed layer, that is the canopy layer, the flow field is determined by local topographic effects: dimension and shape of buildings, streets, vegetated or open zones.

The flow pattern around buildings is complex and depends on the geometry of the building. A simplification of the airflow pattern given by a barrier placed normal to the flow is shown in figures 5.3 and 5.4.

The flow is characterized by three zones. In the displacement zone the flow is displaced up and over the barrier. After the barrier the flow separates in a more turbulent zone, the wake zone. Behind the barrier, the cavity zone is characterized by semi-stationary lee eddy vortexes. When the building is part of an urban environment, the flow pattern depends upon the geometry, particularly on the width to height ratio (S/H, where S is the spacing along the wind direction and H is the mean building height). If the buildings are spaced enough, the flow pattern is similar to the case of single obstacles. When the

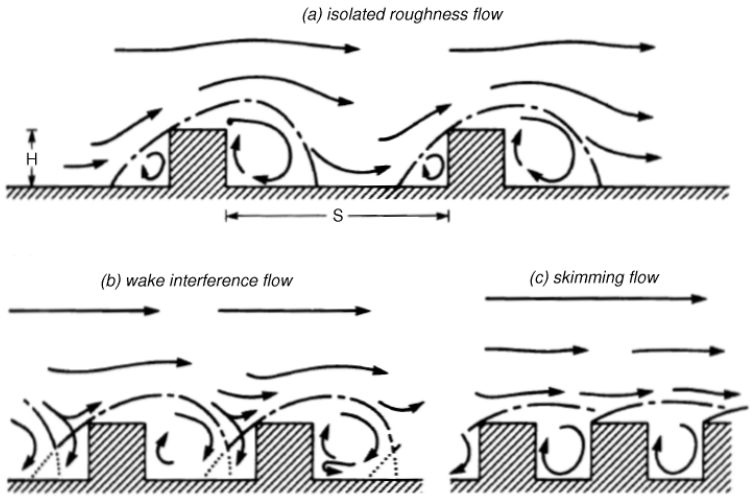

Figure 5.2.: Flow patterns characteristic for different urban geometries: a) widely spaced ($S/H > 0.4$ for cubic and $S/H > 0.3$ for arrays of buildings); b) closer spacing ($S/H > 0.7$ for cubes and $S/H > 0.65$ for arrays of buildings); c) cavities (as streets) (Oke, 1987).

buildings are closer one to the other, the characteristic zones interfere. These flow patterns are found when the wind direction is perpendicular to the longitudinal axis of the street. If the wind is oriented at some other angle, the vortex presents a more complex motion with a component along the street (section 5.3.4). If the flow is parallel to the street, the shelter effect is not present and channeling effect may, on the other hand, cause greater velocities than in the case of open domain.

The value of wind speed measured above the buildings or in urban areas turns out to differ considerably from the value measured at an urban monitoring site, within the buildings. As the roughness is greater in an urban area than in the surrounding countryside, the wind speed at any height is lower in the urban area, and much lower within the obstructed area.

5.3.1. Isolated buildings

Air flow around isolated buildings is characterized by an eddy vortex caused by the flow down the windward facade, while behind the obstacle there is a lee eddy drawn into the cavity of low pressure due to flow separation from the edges of the building top and sides; further downstream the building wake is characterized by increased turbulence but lower horizontal speeds than the undisturbed flow.

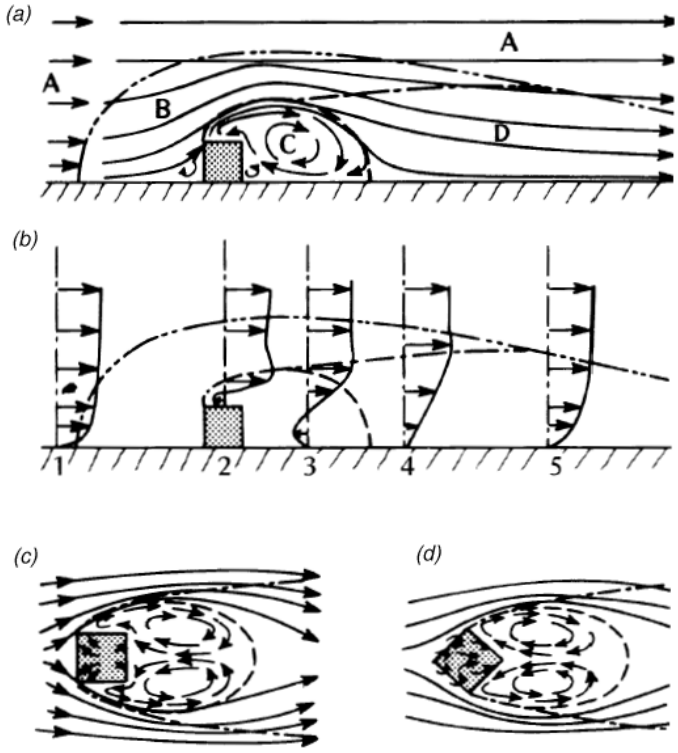

Figure 5.3.: Flow pattern around an isolated flat-roof building: a) side view of streamlines and flow zones; b) vertical velocity profiles and flow zones; plan view of streamlines around buildings oriented c) normally and d) diagonally to the flow (Oke, 1987).

When impinging an isolated building, the flow separates over the roof and reattaches behind the obstacle determining a very unsteady recirculating flow region. This region does not exhibit a closed boundary and material passes in and out both by turbulent and mean flow transport. The size of the recirculating region depends on building geometry and orientation and on approach flow conditions (Robins and MacDonald, 2001).

In some regions of the flow field, the persistent secondary flows transport external fluid towards the surface; as a result, zones of local mean velocity excess may occur. Both momentum deficit and vortex wake components are found in many circumstances. Indeed, a most complex combination may exist downwind of a group of buildings due to the interactions between individual wake components. The flow over a flat roof may or may not reattach, depending on geometry and ambient turbulence levels.

The boundaries of the roof flow regimes have been derived by Röckle (1990). The far-

wake velocity deficit is assumed to occur inside an ellipsoidal volume (called "wake zone"). The downwind recirculating cavity length, B_D is defined as:

$$\frac{B_D}{H} = \frac{1.8\frac{L}{H}}{\left(\frac{L}{H}\right)^{0.3}\left(1+0.24\frac{L}{H}\right)}. \tag{5.1}$$

The upstream recirculating zone is defined through an ellipsoid with a boundary set where the velocities are supposed to be zero (see for example Kaplan and Dinar, 1996). The following parameterization is used for the upwind cavity length B_U:

$$\frac{B_U}{H} = \frac{2\frac{L}{H}}{1+0.8\frac{L}{H}}. \tag{5.2}$$

In equations 5.1 and 5.2 L is the length of the obstacle in the cross-wind direction. Recirculating cavities according to this scheme are represented in figure 5.5.

Bottema (1997) proposes an analogous model, in which B_D and B_U individuate a triangular zone whose height is $\frac{2}{3}H$; the length of the cavity is given by the following relationships:

$$\frac{B_D}{H} = \frac{6\frac{L}{H}}{1+\frac{L}{H}}, \tag{5.3}$$

$$\frac{B_U}{H} = \frac{2\frac{L}{H}}{1+\frac{L}{H}}, \tag{5.4}$$

whose structure is very similar to (5.1) and (5.2).

The shape of recirculating cavities is roughly confirmed by measurement performed by Barlow et al. (2003).

The boundary between reattached and separated flow acts as a non-physical barrier which tends to trap pollutants, cutting-off the supply of clean air into the vortex. The changes in roof flow conditions will influence elevated emissions through streamline displacement and entrainment processes. As a consequence, pollutant dispersion near buildings reflects the complexity of the flow fields.

Plume shape and position and, as a consequence, dilution are clearly strongly dependent on source position and wind direction. The situation becomes even more complicated if the building shape is more complex, or additional buildings are involved. Even small geometric features close to the source may play an important role: figure 5.6 schematically illustrates how a different shape of the obstacle may force most of the emitted material to pass to one side of it, thus breaking the symmetry that would otherwise exist (see

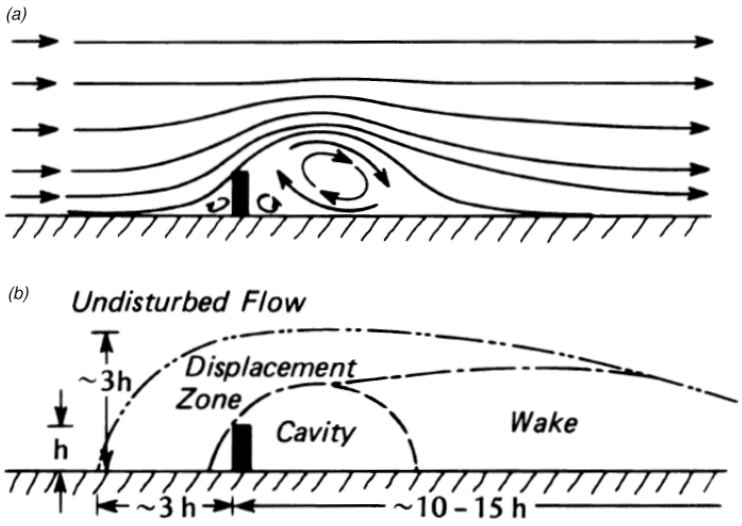

Figure 5.4.: Flow modification caused by a solid barrier: a) streamlines and b) flow zones (Oke, 1987).

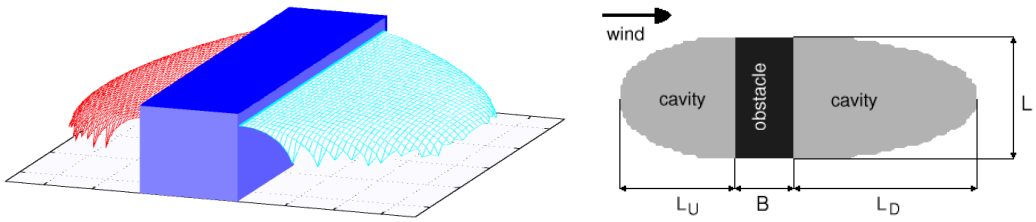

Figure 5.5.: Upwind and downwind recirculating cavities according to Röckle (1990); Bagal et al. (2002); Pardyjak et al. (2002).

Robins and MacDonald, 2001 for details). The first implication is that the effects of source position and wind direction are likely to dominate over other factors (first of all atmospheric stability), at least in the neighbourhood of the buildings, where the mean flow is significantly changed. A similar behaviour applies to material which is entrained from an elevated emission into the recirculation region and is re-emitted from that region as a diffuse, groundbased plume. The concentration field downwind of the near wake can be considered as the sum of two components. One is the diffuse, ground-based plume and the other the remains of the elevated plume, at a reduced height because of streamline deflection and of reduced strength because part of the original emission is entrained into the recirculation region.

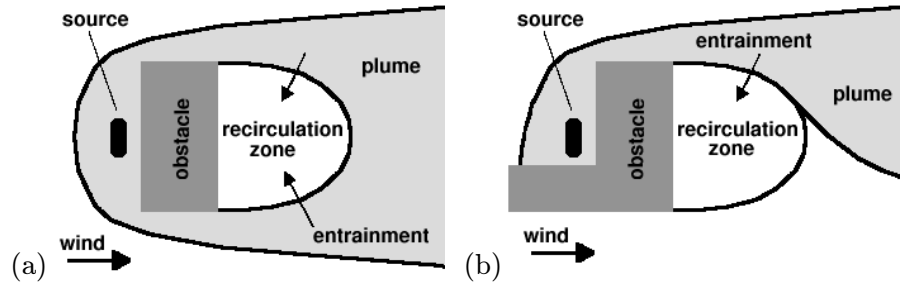

Figure 5.6.: Dispersion patterns for two different type of obstacle (plan view): a) symmetric and b) asymmetric with respect to wind direction.

On the other hand, unlike in the case of ground-level release, ambient conditions have a stronger influence on dispersion processes for elevated emissions (i.e. the case where the plume is not constrained in the obstructed zone).

5.3.2. Groups of buildings

The above distinctive features which characterize the flow around a single isolated building are also displayed in the case of a group of buildings, although their relative and absolute importance is affected by interactions within the group of obstacles. As a first approximation we can consider a group of buildings as a set of isolated buildings; the cumulative effects of the group can be treated by linear addition of the effects due to each element. This is appropriate when the spacing is so large, typically greater than $10 \div 20$ building heights, that each element effectively experiences undisturbed boundary layer conditions. For smaller spacing, the flow conditions at downwind buildings are perturbed by the upstream obstacles; however, to a sufficiently small extent the linear superposition remains acceptable (Santamouris and Dascalaki, 2003). As shown in figure 5.2, three different regimes characterize the flow in and above the urban canopy, first described by Oke (1987).

Of course, mean flow through the array of buildings still occurs along longitudinal channels. Exchange between the recirculation region and the external flow occurs through turbulent diffusion, with some external flow penetrating into the region at its downstream end. The average roughness of the array is relatively low and decreases as the spacing S between buildings decreases. At the other extreme lies the isolated obstacle regime, where the nearwake flows associated with individual buildings are only weakly perturbed by surrounding buildings. In this case the flow can be described as a superposition of many independent building wake flows. Again, the apparent aerodynamic roughness of the array

is relatively low, but now decreases as the spacing S between buildings increases. The roughness length is greatest in the wake interference regime, which is transitional between the so-called "skimming" and "isolated" obstacle regimes (see section 5.3.3). A variety of complex and rather unsteady flows can now occupy the spaces between buildings, with recirculation zones and regions where the external flow penetrates to the ground. The displacement height z_d (i.e. the effective zero velocity height in the log-law wind profile of the external flow) tends to zero as the relative spacing S/H becomes large, and increases monotonically as the spacing decreases, tending to H as S/H tends to zero.

5.3.3. Air flow in urban canyons

Urban canyons are characterized by three main characteristic dimensions: the mean height of the buildings in the canyon H, the canyon width S, and the canyon length L . Given these values, two dimensionless parameters can be derived: the building density H/S (that is the inverse of the relative spacing) and the aspect ratio L/H. Most of existing studies deal with the problem of the determination of the pollution characteristics within the canyon, with specific emphasis to the case of an ambient flow perpendicular to the canyon longitudinal axis; notice that highest values of pollution occur inside the canyon under this condition.

When the predominant direction of the airflow is approximately perpendicular with respect to the street axis (i.e. $\pm 20°$), three types of air flow regimes are observed, as explained in section 5.3. When the buildings are well apart ($H/S < 0.05$), their flow fields do not interact. At closer spacing the wakes are disturbed, the flow regime is known as "isolated roughness flow" and the problem is treated as explained in previous section. When the height and spacing of the array combine to disturb the downwind cavity eddies, the regime changes to that referred to as "wake interference flow". This regime is characterized by secondary flows in the canyon space where the downward flow of the cavity eddy is reinforced by deflection down the windward face of the next building downstream. At larger values ratio H/S, a stable circulating vortex arises in the canyon because of the transfer of momentum across a shear layer of roof height, and transition to the so called "skimming flow" regime occurs where the bulk of the flow does not enter the canyon. The transitions between these three regimes can be set in terms of the dimensionless parameters H/S and L/S.

According to Oke (1987) two threshold lines can be individuated, as shown in figure 5.7. Many industrial and urban building configurations lie in the skimming regime (i.e. high H/S ratios). In this case, when the crosswind area of the buildings is sufficiently extended,

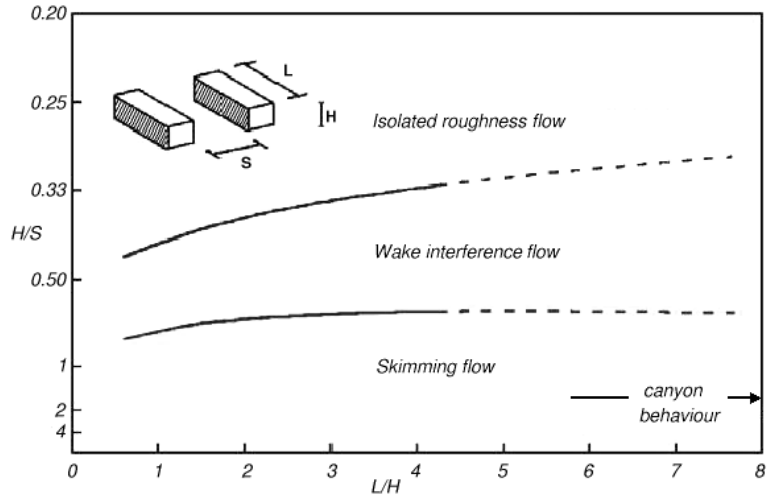

Figure 5.7.: Threshold lines dividing flow into three regimes as functions of the building (L/H) and canyon (H/S) geometry (Oke, 1987).

the so-called "urban street canyon flow" establishes. However, an effective canyon effect arises only over a threshold value of the roof-level wind speed (Santamouris and Dascalaki, 2003). Many authors (e.g. Nakamura and Oke, 1989) report a threshold wind speed nearly equal to $2\,m/s$, according to experimental studies. Higher wind speeds have been found to produce a stable vortex circulation within the canyon. For lower wind speeds thermal as well as mechanical influences may play an important role in the canyon circulation. Further details will be given in section 6.4.1, while an example of flow field computation inside the canyon through the method of Hotchkiss and Harlow (1973) is reported in figure 6.17.

As far the relationship between the wind speed outside the canyon and the corresponding vortex velocity, for wind speeds higher than the threshold value, Hotchkiss and Harlow (1973) have found that the speed of the vortex increases with the speed of the cross canyon flow. Since the vortex is driven by a downward transfer of momentum across the roof-level shear zone, a flow normal to the canyon axis will induce, with a air flow near the ground in the opposite direction with respect to the wind outside the canyon.

Also the finite length of a canyon plays an important role on the air flow distribution (Yamartino and Wiegand, 1986). We may notice that a further motivation for the study of circulation at the street canyon scale is that air pollution impact of emissions from most transport systems in urban areas involves source-receptor distances that are very short and

pollutant concentrations that can be very high. Such local effects cannot be resolved by largescale urban models. The simplest street canyon model is cast as a box-model, which accounts for the conservation of pollutant flux between the cavity (source point) and urban canopy layer above (diffusion).

However, a number of important issues are still studied and are not yet understood completely:

- determination of the roof-level wind from standard meteorological data;
- evaluation of the street-level wind from the rooflevel winds;
- effects of atmospheric stability and local building surface heating and cooling;
- geometrical configurations that can be treated with a canyon model.

The last problem will be addressed more deeply in chapter 6.

5.3.4. Air flow along urban canyons

As in the case of perpendicular winds, the air flow in the canyon has to be seen as a secondary circulation feature driven by the above roof imposed flow (Santamouris and Dascalaki, 2003). If the wind speed out of the canyon is below some threshold value the coupling between the upper and secondary flow is lost, and the relation between wind speeds above the roof and within the roof is characterized by a considerable scatter (Nakamura and Oke, 1989). As far the relationship between the free stream wind speed U and the along-canyon velocity V_a, Yamartino and Wiegand (1986) report that the along canyon wind component in the canyon is directly proportional to the above-roof along canyon component. Furthermore, as a first order approximation, they find that $V_a = U \cos\alpha$ at least to first order, where α is the incidence angle. Nakamura and Oke (1989) report that for wind speeds up to $5\,m/s$ the general relation between the two wind speeds appears to be linear, that is $V_a = c \cdot U$.

Also when the free stream wind travels along only a limited section of the canyon, the relation between the two wind speeds is almost linear. A composition of the vertical wind speed and of the along canyon free stream wind is found for winds that penetrate a longer canyon section, reaching an equilibrium with the frictional effect on the walls and floor. In this case deceleration is reduced as well as the vertical outflow which occurs at the the canyon top.

5.3.5. Roughness height and displacement height

When working at the urban scale it is often required to parametrize the roughness produced by the presence of obstacles in order to obtain averaged values for wind and eddy turbulence profiles: to this aim the quantities z_0 and z_d are introduced.

The roughness length z_0 describes the hypothetical height at which wind speed logarithmic profile equals to zero.

Where the obstacles are dense, the "effective ground level" is not located near the ground but it falls roughly at the middle of the urban canopy because the wind flow is displaced upward. The presence of building introduces an additional roughness (with respect to rural areas), which displaces the wind profile vertically so that a hypothetical surface is developed at the height of about two thirds of obstacles height (Oke, 1987). This imaginary surface is called the "zero plane displacement height" or simply "displacement height", denoted with z_d. The logarithmic (neutral) wind profile $U(z) = \frac{u_*}{k} \ln \frac{z}{z_0}$ has to be modified accordingly (Arya, 1999):

$$U(z) = \frac{u_*}{k} \ln \frac{z - z_d}{z_0}. \tag{5.5}$$

All the vertical profiles of parameters which are somehow related to turbulence (i.e. K_z, Φ, Ψ) vary accordingly, displacing their reference height by the quantity z_d. In any case it should be underlined that z_d doesn't correspond to a physical interface and hence is only used as a way for parameterizing the geometry without accounting for it explicitly. Therefore, once the displacement height has been computed, the formulation derived for uniform terrain are adopted.

As pointed out by Tennekes (1973), all methods used to determine z_0 and z_d make use of the logarithmic wind profile, relating wind speed at a certain level to the friction velocity; hence, they implicitly assume a neutral stratification; otherwise equation 5.5 should be corrected using similarity functions:

$$U(z) = \frac{u_*}{k} \left[\ln \left(\frac{z - z_d}{z_0} \right) - \Psi \left(\frac{z - z_d}{L_{MO}} \right) \right], \tag{5.6}$$

where Ψ is the stability function as defined in section 1.2.1.

Below the level z_d the turbulence is strongly reduced, whereas above the hypothetical z_d level the air is actively turbulent. Theoretically the level at z_d is an equivalent height for zero wind speed, and it also represent the height at which momentum is transmitted from the production zone to the dissipation zone. The zone below is characterized by production

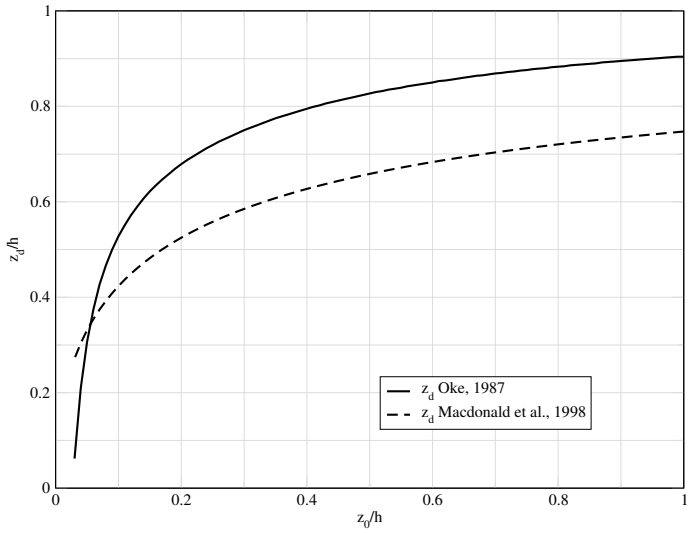

Figure 5.8.: Relationship between displacement height and roughness height..

of mechanical turbulent energy (shear stress). Indeed, for $z < z_d$ one may still observe $u \neq 0$: turbulent eddies with a length scale which is less than z_d are generated, but the average speed is zero: $\int_0^{z_d} u(z) = 0$. Furthermore, a micro-roughness located "inside" a macro-roughness is subject to a sheltering effect; in this case z_d is controlled by the biggest obstacles. An interesting case, but very difficult to deal with, is represented by a domain spanning two spatial scales in roughness definition (e.g. working at the scale of an urban canyon): the straightforward procedure should consist in the computation of the "internal" wind profile, using the corresponding roughness, and the subsequent match of the profile with the "external" profile at the larger scale.

Equation 5.6 describes the vertical wind profile above the roughness sublayer, when the air flow is in equilibrium with a level homogeneous surface. Besides other consequences, this would imply that measurements should be taken above the roughness sublayer so that they are not disturbed by turbulence generation at the interface. Furthermore, in order to consider the terrain as uniform, the horizontal fetch should be long enough.

The reference heights z_d and z_0 in equation 5.5 (or 5.6) can be estimated with a wind profile measured at several levels, or, alternatively they can theoretically be calculated from at least two levels of wind data. If wind speed measurements, U_1 and U_2 are available respectively at height z_1 and z_2, the equations can be solved in terms of z_0 and z_d to give:

$$\begin{cases} z_d = z_1 - \frac{z_2 - z_1}{\exp\left[\frac{k}{u_*}(U_2 - U_1)\right] - 1} \\ z_0 = \frac{z_2 - z_1}{\exp\left(\frac{k}{u_*}U_2\right) - \exp\left(\frac{k}{u_*}U_1\right)} \end{cases} . \tag{5.7}$$

However, it should be pointed out that velocity values are available at two levels over the roof-level; this method is therefore hardly applicable.

For this reason the simple empirical formulation proposed by Lettau (1969), which relates the surface roughness z_0 of a group of obstacles of mean height H to its frontal area density λ_F, is often used:

$$\frac{z_0}{H} = 0.5\lambda_F. \tag{5.8}$$

The frontal area density λ_F is defined as the ratio $A_F/A_{F,tot}$, where A_F represents the total silhouette area of all obstacles in the area $A_{F,tot}$, measured in vertical-crosswind plane. Equation 5.8 works well for low obstacle densities, but fails when λ_F increases beyond about 0.2. Furthermore, the simple analytical model developed by Macdonald et al. (1998), based on physical assumptions, shows that Lettau's model can be generalized by incorporating the effect of obstacle density on the displacement height, using the empirical expression 5.8; the resulting expression for the ratio z_d/H as a function of the plan area density $\lambda_P = A_P/A_{P,tot}$ of the array reads:

$$\frac{z_d}{H} = 1 + c^{-\lambda_P}\left(\lambda_P - 1\right), \tag{5.9}$$

where the empirical parameter c is approximately equal to 4. The expression for z_0 takes the following form:

$$\frac{z_0}{H} = \left(1 - \frac{z_d}{H}\right)\exp\left[-\frac{1}{\sqrt{\frac{\lambda_F C_{dh}}{2k^2}\left(1 - \frac{z_d}{H}\right)}}\right], \tag{5.10}$$

where k is the von Karman constant and C_{dh} the drag coefficient, set equal to 1.2 according to Macdonald et al. (1998).

Taking advantage of equation , an alternative solution for z_d has been proposed by Oke (1987):

$$z_d = H - z_0(x - 1), \tag{5.11}$$

with x given through the implicit formula $x\ln(x) = 0.1(H/z_0)^2$; furthermore, (5.9) can be approximated through the following expression

Table 5.2.: Typical values of roughness length (Oke, 1987).

Terrain	$z_0\,[m]$
Scattered settlement	$0.2 \div 0.6$
Suburban low density	$0.4 \div 1.2$
Suburban high density	$0.8 \div 1.8$
Urban high density	$1.5 \div 2.5$
Urban very high density	$2.5 \div 10.$

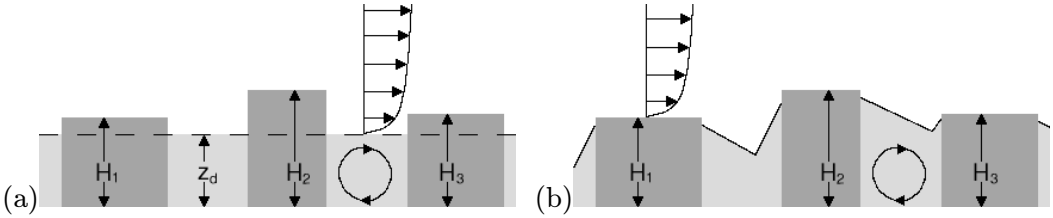

Figure 5.9.: Scheme of recirculation zones using a) z_d as a reference height (global approach) and b) calculating their approximate shape (local approach).

$$\frac{z_d}{H} = 110 - 170\left(\frac{z_0}{H}\right)^{-0.467}, \tag{5.12}$$

valid for $z_0 > 0.03H$ (see figure 5.8). Figure 5.9 schematically shows how recirculating zones are individuated, using z_d as a reference height and calculating their approximate shape, as explained in section 5.3.1.

Notice that perturbations in the vertical direction due to buildings die out at a height of about three building heights; the outer layer is therefore conventionally positioned at a height of about $z_d + 3H$.

Typical values of z_0 are given by Oke (1987) and reported in table 5.2:

5.4. Urban dispersion modelling

The prediction of pollutant dispersion in urban areas can rarely account for all the details described in the preceding section; hence, some drastic simplifications are normally applied, such as treating a large built-up area as if it were constituted of a set of isolated obstacles, or modelling the whole group as an equivalent, homogeneous array.

When adopting very simplified models, which have the advantage of a simple calibration, one should anyway keep in mind that strong differences in terms of pollutant concentration

are in reality observed inside the urban areas. Poorly ventilated regions, such as tightly enclosed courtyards, are characterized by weak mixing with the external flow and hence long residence time for locally emitted pollutants; on the other hand, buoyant discharges may rise relatively rapidly because of the quiescent ambient state. In other sections of the array ventilation may be very efficient, driven by mean flow advection as well as turbulent diffusion. The mechanisms involved include direct penetration of the external wind into open areas and streets aligned with the wind and upward mean flow in the wakes of the larger obstacles within the array.

A wide range of urban air quality models exists, reflecting the abundance of end requirements as, for example, air quality standards. A sort of gaussian plume model is frequently used in operational models, with special algorithms added to treat specific circumstances such as street canyons and highways. Atmospheric chemistry is commonly included because of its importance in determining levels of pollutants.

5.4.1. Gaussian formulation

Gaussian plume models are used in a wide variety of urban dispersion models because of their relative simplicity and the ease with which additional effects due to source buoyancy, stability, deposition, surface roughness and averaging time, may be included (e.g. Turner, 1994). The general form of the equation, valid for a uniform stationary case, reads:

$$\begin{aligned} C(x,y,z) &= \frac{\dot{M}}{2\pi U \sigma_y \sigma_z} \exp\left(-\frac{y^2}{2\sigma_y^2}\right) \\ &\cdot \sum_{n=-\infty}^{+\infty} \left\{ \exp\left[-\frac{(z - z_s + 2nz_{top})^2}{2\sigma_z^2}\right] \exp\left[-\frac{(z + z_s + 2nz_{top})^2}{2\sigma_z^2}\right] \right\} \end{aligned} \quad (5.13)$$

In (5.13) z_s is the effective height of the source and z_{top} the height of the calculus domain (physically the inversion height where a sudden decrease in the eddy diffusivity occurs); σ_y and σ_z depend on the downwind travel distance x. More refined models accounts for non-constant profile for wind and eddy diffusivity as well as for continuous line sources (see e.g. Demuth, 1978; Huang, 1979).

In any case these models are generally limited to time-averaged concentrations over at least 15 minutes or more (usually 1 hour is used), over terrain for which the meteorological and surface features remain constant. Moreover, using this simple approach, the evolution in time of the field of concentration can only be approximated as a sequence of stationary states, which cannot account for the background concentration resulting from the release

at previous time. Models using equation 5.13 (or modified versions) have been developed to cope with simple problems (open areas, homogeneous and stationary situations), but are nevertheless used, with some adjustment for calculating pollutant dispersion over complex topography, due to the ease to calibrate them. In particular, in urban areas equations like 5.13 are adopted, shifting the vertical coordinate at level z_d, while the source is typically located inside the roughness itself ($z < z_d$).

A popular method for dealing with plume dispersion when the source is located inside the roughness is to make use of virtual source modelling. The assumption is that both lateral and vertical plume spread is increased of a constant value σ_0 (to be estimated, e.g. Santomauro, 1975; Zannetti, 1990):

$$\sigma'(x) = \sigma_0 + \sigma(x). \tag{5.14}$$

These models are in general used to predict concentrations from plumes whose size is much greater than the roughness elements, and may even be approaching the height of the mixing layer. The longer-range urban models do not generally possess the ability to resolve the concentration field to a high degree. Specific adjustments are usually made to account for significant local sources such as major motorways or street canyons where pollutant levels are enhanced over the spatially averaged values. Typically, clusters of groundlevel sources are combined into area sources.

Values for σ_y and σ_z are well consolidated (Briggs, 1973; Gifford, 1957b,a, 1959); for urban areas one should pay more attention because they can be strongly inhomogeneous, thus implying variations on z_0 and u_*, and consequently on dispersion parameters. Moreover it should be stressed that gaussian models assume far field hypothesis, while maximum ground level concentration are in the near field. A commonly used approximation is to simulate the increased turbulence in an urban area by first estimating the standard Pasquill stability class from the solar radiation data and wind speed (see table 5.3 and figures 5.10 and 5.11), and then shifting to the next more unstable class. Variations in surface roughness may also be accounted for, by adjusting the value of σ_z, characterizing the plume spread in the vertical direction, valid for a reference surface roughness z_0, to another roughness length. In particular the relationship proposed by Zannetti (1990) reads:

$$\sigma_{z,urban} = \sigma_{z,rural} \left(\frac{z_{0,urban}}{z_{0,rural}} \right)^{0.2}. \tag{5.15}$$

Dispersion in urban areas can be schematically classified in three regimes, on the basis of the distance from the source.

Table 5.3.: Urban dispersion coefficients according to Pasquill stability class according to Briggs (1973); all distances are expressed in meters.

Stability	$\sigma_y(x)$	$\sigma_z(x)$
$A-B$	$0.32x\,(1+0.0004x)^{-\frac{1}{2}}$	$0.24x\,(1+0.0010x)^{\frac{1}{2}}$
C	$0.22x\,(1+0.0004x)^{-\frac{1}{2}}$	$0.2x$
D	$0.16x\,(1+0.0004x)^{-\frac{1}{2}}$	$0.14x\,(1+0.0003x)^{-\frac{1}{2}}$
$E-F$	$0.11x\,(1+0.0004x)^{-\frac{1}{2}}$	$0.08x\,(1+0.0015x)^{-\frac{1}{2}}$

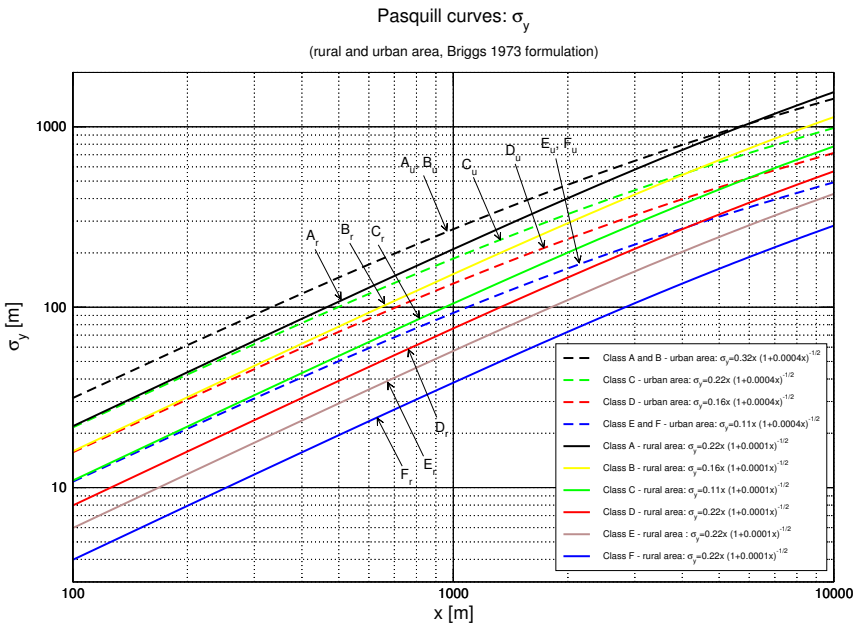

Figure 5.10.: Briggs (1973) formulation of Pasquill classification for lateral dispersion parameter σ_y.

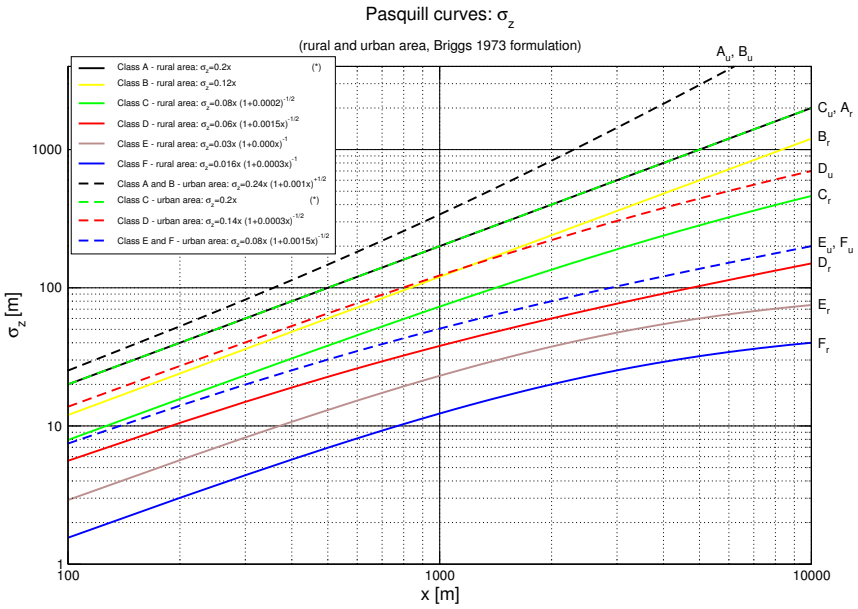

Figure 5.11.: Briggs (1973) formulation of Pasquill classification for vertical dispersion parameter σ_z.

The near field is the region closer to the release point, where the plume dimension is smaller than the individual obstacles, typically $\sigma_y < L/4$ and $\sigma_z < H/3$. In this regime the local aerodynamic effects around individual obstacles dominate the plume path and very high levels of spatial and temporal variation exist. Dispersion patterns tend to be site dependent and hardly generalizable. In this regime there can be large variations in the dispersion characteristics due to the multiplicity of possible obstacle shapes and orientations, and the relative position of source and receiver.

In the intermediate or neighbourhood field the plume reaches the order of magnitude of the obstacles, with values of $\sigma_y = L/4 \div L$ and $\sigma_z = H/3 \div H$. A large portion of the plume is still within the urban canopy. Although there is less spatial and temporal variation in this regime, the dispersion rate is still strongly influenced by the details and layout of the obstacles. The lateral concentration profile is nearly gaussian, while in the vertical direction it shows a more complex profile.

Far enough from the source (far field), the plume extends above the urban canopy and the concentration within the canopy is relatively uniform over its depth. The plume dimensions are larger than those of the obstacles ($\sigma_y > L$ and $\sigma_z > H$) such that the details of the individual obstacles and their layout pattern are no longer important. Here the surface features can be modelled as a uniform roughness. This is the regime of conventional urban

dispersion modelling, where the urban surface affects the dispersion through the high level of mechanical turbulence generated by the surface drag of the buildings. Unlike in the first two regimes, in the far field conventional gaussian plume models could be used.

5.5. Chemistry and deposition

Pollutant is removed from atmosphere through deposition or through chemical transformation. Theoretical description which follows helps to understand why air pollution models sometimes fail to predict concentration of pollutants on small spatial scale processes, as results of section 6.3.4 show. Deposition mechanism can be "dry" or "wet"; these two mechanisms are quite different; they are described briefly in the following section and are both considered in the model proposed in section 6.3.

5.5.1. Deposition

Dry deposition modifies the airborne concentration in two ways: reduction in plume strength and adjustment of the vertical profile due to removal, which is assumed to occur only at the surface. The rate of dry deposition is assumed to be proportional to the near-surface concentration, that is:

$$D_D = v_e \, C|_{z=0} \,, \tag{5.16}$$

where D $\left[g/\left(m^2 s\right)\right]$ is the rate of deposition, C $\left[g/m^3\right]$ is the air concentration at ground level and v_e is the deposition velocity. This velocity contains a diffusive part v_d (also denoted as deposition velocity), and an element due to the gravitational settling v_s (or terminal gravitational velocity). According to (Apsley et al., 2003), the overall deposition velocity v_e reads:

$$v_e = \frac{v_s}{1 - \exp\left(-\frac{v_s}{v_d}\right)}. \tag{5.17}$$

Both v_d and v_s may be estimated on the basis of gas type, or particle size and density. v_d is expressed as the combined effect of three resistances, namely:

$$v_d = \frac{1}{r_a + r_b + r_s}, \tag{5.18}$$

where r_a is the aerodynamic resistance, r_b is the sublayer resistance and r_s is the surface layer resistance. These resistances depend on the pollutant species, nature of the surface

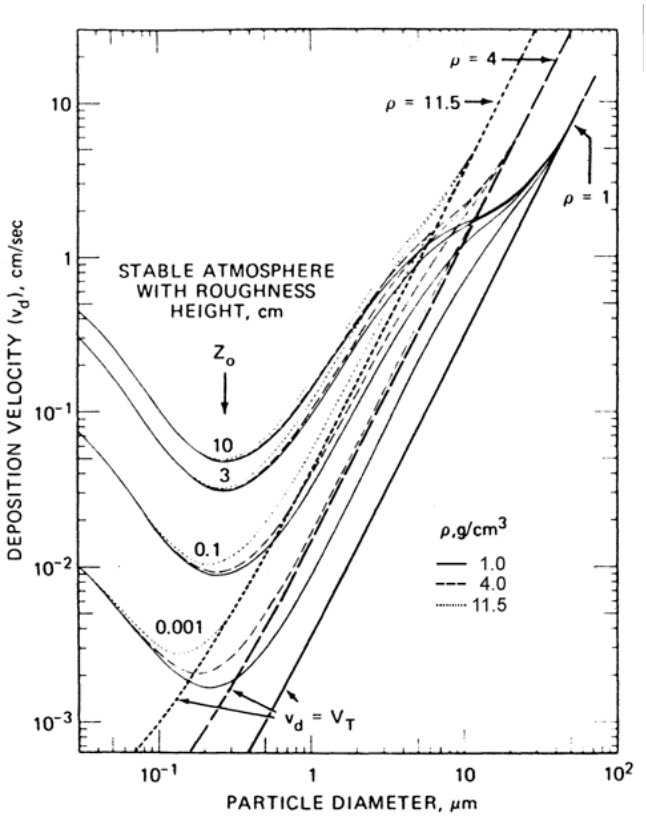

Figure 5.12.: Settling velocity for friction velocity $u_* = 0.5\,m/s$ and particle density $\rho = 1$, 4, $11\,g/cm^3$ (Sehmel, 1980).

and the wind speed. For particles r_s is null, while it ranges about $30\,s/m$ for reactive gases (for example SO_2), $1000\,s/m$, far weakly reactive gases (e.g. O_2) and tending to infinite for inert gases, for example N_2 (see Sehmel, 1980 and Apsley et al., 2003).

In the case particulate v_s results to be greater than v_d so that $v_e \simeq v_s$; the latter is well approximated using Stokes formulation:

$$v_s = \frac{d^2}{18}\frac{\rho_s g}{\mu_a}, \tag{5.19}$$

with ρ_s particle density, d average diameter and μ_a air dynamic viscosity. Stokes law is only valid for $\mathrm{Re} \leq 1$, where:

$$\mathrm{Re} = \frac{v_s \rho_a d}{\mu_a}. \tag{5.20}$$

Table 5.4.: Overall deposition velocity v_e for some gases(Sehmel, 1980); a huge variability, also for the same chemical compound, can be noted.

Gas	$v_e\,[cm/s]$	Gas	$v_e\,[cm/s]$
SO_2	$0.04 \div 7.5$	NO_2	1.9
Cl_2	$1.8 \div 2.1$	NO	< 0.9
O_3	$0.002 \div 2$	CO_2	0.3

Assuming typical values of $d = 10^{-5}m$, $\rho_s = 5000\,kg/m^3$ for suspended particulate, the resulting value of Reynolds number is of order 1; however, decreasing the diameter, attraction and repulsion forces among particles gain importance; in this case Stokes law no longer applies, and empirical formulations such the one reported in figure 5.12 should be used instead.

For what gas is concerned, the terms v_s and v_d are of the same order of magnitude; deposition mainly acts through diffusive processes at the interface between fluid and surface (where the term r_s becomes important). In the literature one can typically find values of v_e (Sehmel, 1980), which allow one to define an equivalent deposition flux.

Notice however that v_e for some compounds varies of some orders of magnitude depending on surface nature (see table 5.4); therefore, a reference value isn't always very significant.

Wet deposition is usually modelled through a washout coefficient $k_W\ [1/h]$. It depends on the nature of the pollutant and on its concentration in air and raindrops. The following simplifications are usually adopted: rain does not lead to a redistribution of material in the plume, no distinction is made between incloud scavenging (rainout) or below-cloud scavenging (washout). Under these conditions the source strength decays exponentially with the time of travel in the rain and concentration decays accordingly: hence, it can be expressed as (Apsley et al., 2000):

$$C = C_0 \exp\left(-k_W T_R\right), \tag{5.21}$$

where $T_R\ [h]$ is the duration of the rainfall and C_0 the original concentration (in absence of rainfall). Deposition flux $D_W\ [g/(m^2 s)]$ at ground, integrated over a vertical column of height h, is given by

$$D_W = \frac{1}{T_R}\left[\int_0^h C_0 dz - \int_0^h C dz\right], \tag{5.22}$$

where C and C_0 represent the local airborne concentration with and without rain.

The washout coefficient is related to the precipitation rate through a monomial formula $k_W = aJ^b$, where $J\,[mm/h]$ is the rainfall rate and a and b are parameters depending on the type of pollutant. The order of magnitude of k_W is about $10^{-4}\,h^{-1}$.

5.5.2. Chemistry and photochemical pollution

Secondary particulate (mainly sulphate and nitrate formed by chemical reactions in the atmosphere) and coarse suspended particulate (dust, biological particles) should be added to primary particulate concentration, otherwise model are likely to underestimate PM_{10} concentration, as shown in section 5.3.4.

5.5.2.1. Nitrogen oxides and ozone

As the composition of urban areas contains many pollutant species, photochemical reactions are usually more important than in rural areas. The so-called "photochemical smog" is created mainly due to nitrogen compounds, which are denoted as NO_x. Nitrogen monoxide NO is created through atmospheric nitrogen N_2 oxidation, while nitrogen dioxide is in turn generated by oxidation of the first species, in a set of reactions which create ozone O_3 as a by-product:

$$\begin{aligned} NO_2 + h\nu|_{\nu<430nm} &\rightarrow O + NO \\ O + O_2 + M &\rightarrow O_3 + M \\ NO + O_3 &\rightarrow NO_2 + O_2. \end{aligned} \tag{5.23}$$

Nitrogen dioxide gives again monoxide through photo-dissociation, acting in this way as a reaction catalyzer. The ratio $\frac{[NO][O_3]}{[NO_2]}$ varies during the day depending upon solar radiation; under constant irradiation increasing of O_3 concentration implies a reduction of the ratio NO/NO_2 and vice versa. Also hydrocarbons play a role in nitrogen monoxide oxidation: the example with the simplest hydrocarbon (CH_4) reads:

$$CH_4 + 2O_2 + 2NO \rightarrow H_2O + HCHO + 2NO_2. \tag{5.24}$$

Indeed methane is the less reactive among the hydrocarbons: the reaction is only reported as an example: the aim of this brief description isn't to give a complete description of the complex reaction which occur in polluted atmosphere, but to point out that passive

tracer hypothesis cannot be applied to some pollutants, unless the time evolution scales are completely different from the dispersion time scale. Indeed chemical reaction time scales for NO_x and O_3 are of the order of few hours, so chemical reaction should be taken into account at least in the near and intermediate field. Calibration of numerical models for passive transport should thus be performed using a non-reacting o slowly reacting chemical compound: in this work calibration was done by using carbon monoxide (CO) concentration from routine measurements of air quality stations. Fine particulate matter is subject to more complex mechanism, which is better described in the following paragraph.

5.5.2.2. Airborne particulate

Airborne particulate matter is a poorly sorted material in terms of its physical and chemical properties and there are many sources which contribute to atmospheric concentrations.

Airborne suspended particulate matter may be either primary or secondary in its origin. Primary particles are those directly emitted into the atmosphere from sources such as road traffic, coal and oil burning, industry, windblown soil and dust and sea spray. On the other hand, secondary particles are formed within the atmosphere by chemical reaction or condensation of gases, and the major contributors are sulphate and nitrate salts formed from the oxidation of sulphur dioxide and nitrogen oxides respectively.

These low volatility species are initially present as gaseous species but ultimately, some distance downwind, become particles or become attached to particles. If they transform into secondary particles by the nucleation of new particles and grow by coalescence, then they are said to have been formed by homogeneous nucleation. However, more often the low volatility species attach themselves to pre-existing aerosol species in which case the process is called heterogeneous nucleation.

The formation of secondary particulate matter through the generation of entirely new particles by homogeneous nucleation, appears to occur by the photochemical oxidation of sulphur dioxide SO_2. This chemical compound is present in ambient air due to emission from coal and oil burning engines and power plants and industries. Photochemical oxidation of sulphur dioxide is initiated through the following sequence of reactions (Airborne Particle Expert Group, 1999):

$$\begin{aligned} OH + SO_2 + M &\rightarrow OH - SO_2 + M \\ OH - SO_2 + O_2 &\rightarrow OH - O + SO_3 \\ SO_3 + H_2O &\rightarrow H_2SO_4 \end{aligned} \tag{5.25}$$

where M represents an atmospheric nitrogen or oxygen molecule, and OH is the hydroxyl free radical.

The sulphuric acid H_2SO_4 in vapour form nucleates to form sulphuric acid droplets and, by simultaneously condensing water vapour, grows rapidly out of the nanometer size range. These initial nuclei continue growing rapidly by condensing and by coalescing with pre-existing aerosol particles. Ultimately the particles increase in size producing a relatively stable distribution of particles sizes in the nucleation and accumulation modes, covering the range spanning from $0.01\,\mu m$ to $1\,\mu m$ size. The highly acidic aerosol droplets can also take up ammonia, NH_3, from the gas phase forming droplets of ammonium sulphate, leading also to a growth in aerosol mass per unit volume, through the reactions:

$$\begin{aligned} NH_3 + H_2SO_4 &\rightarrow NH_4HSO_4 \\ NH_3 + NH_4HSO_4 &\rightarrow (NH_4)_2\, SO_4 \end{aligned} \tag{5.26}$$

The main sources of NH_3 are agricultural in origin through the storage, disposal and application to soils of animal wastes and industrial fertilizers. The timescale for the nucleation and accumulation processes involving sulphuric acid is generally rapid if compared to the timescale of the SO_2 oxidation processes. The photochemical production of sulphuric acid particles therefore occurs on the spatial scale of the SO_2 oxidation, which in turn depends on the hydroxyl radical OH concentration. SO_2 oxidation rate by this reaction occurs at the rate of about a few per cent per hour. This gives a timescale of $1.5 \div 2$ days and a horizontal spatial scale of more than $100\,km$, which exceeds the urban scale, but falls completely within the regional transport scale. Photochemical oxidation of SO_2 is driven by sunlight and occurs to a greater or lesser extent at different times of the year.

Figure 5.13 shows the distribution of particle sizes typically found in urban environments. Particles can be classified as occurring in three modes: the nuclei, accumulation, and coarse particle modes. The particles in each mode have typically different sources and chemical compositions. The nuclei and accumulation modes together constitute fine particles, or fine particulate matter (i.e. $PM_{2.5}$, $d \leq 2.5\,\mu m$). The shape of the particle size distribution is multimodal, displaying three peaks. The nuclei mode consists primarily of combustion particles emitted directly into the atmosphere from motor vehicles, especially diesel vehicles, as well as particles formed in the atmosphere by gas-to-particle conversion. Significant concentrations of particles in the nuclei mode are not always present, but are usually found near highways or road characterized by high speed. These very fine particles

attach rapidly to particles in the accumulation mode. The accumulation mode includes combustion and photochemical smog particles and attached nuclei mode particles. Removal mechanisms, such as settling, deposition to surfaces, or adhesion to rain droplets, are weak for this size range. The coarse-particle mode (i.e. PM_{10}, $d \leq 10\,\mu m$) consists of windblown dust, salt particles from sea spray, and mechanically generated particles like those from construction sites. These large particles settle out relatively quickly and so their lifetime in the atmosphere is of the order of hours.

While the coarse fraction settles relatively quickly (i.e. $0.5 \div 5\,cm/s$), the finer fraction deposits more slowly ($0.05 \div 0.5\,cm/s$). The difference is obviously due to the fact that larger particles have a higher gravitational settling velocity than small particles. Fine and coarse particles have therefore different lifetimes in the atmosphere, and there is a negligible mass exchanged between these two modes (see also figure 5.13). Industrial sources may lead to locally elevated concentrations of PM_{10}. Within urban areas, however, the influence of road traffic is far more marked. The contribution of secondary particles is more uniform as these are formed relatively slowly in the atmosphere and have a long atmospheric lifetime. Moreover, as evidenced by Hinds (2001), road traffic contributes to secondary particle formation through emissions of NO_x.

The major contributor to PM_{10} in urban air is road traffic, which also indirectly creates secondary particles dominated by the $PM_{2.5}$ fraction which is potentially more important in relation to health impacts. The sources of primary particles in the $2.5 \div 10\,\mu m$ range are less clearly defined, but resuspended street dusts, windblown soils and sea spray particles are major contributors.

Estimates of emissions from diffuse and natural sources such as dust suspended from road surfaces by wind and traffic-induced turbulence are subject to very great uncertainties, also due to climatological factors: in winter the major contributor to episodes of high particulate concentration is exhaust emission from road transport; in summer, on the contrary, secondary sulphate and nitrate particles formed from atmospheric oxidation of sulphur and nitrogen oxides appear to be the primary cause of episodes of high PM_{10} concentration, although the contribution of coarse particles, largely resuspended surface dusts, is also important.

Resuspended dust sources are usually ground-level, namely linear or areal sources. The fraction of emissions which is transported for long distances from emission sources can be determined from a combination of the following counteracting processes:

- Deposition rate: the rate at which particulate matter is deposited at the ground surface depends upon the size and density of the particles; the characteristics of the

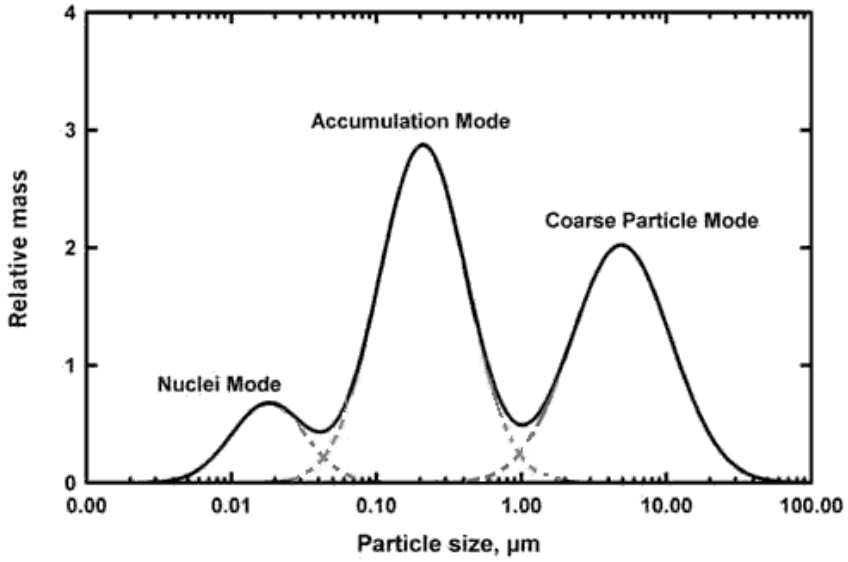

Figure 5.13.: Typical urban particulate distribution (Hinds, 2001)

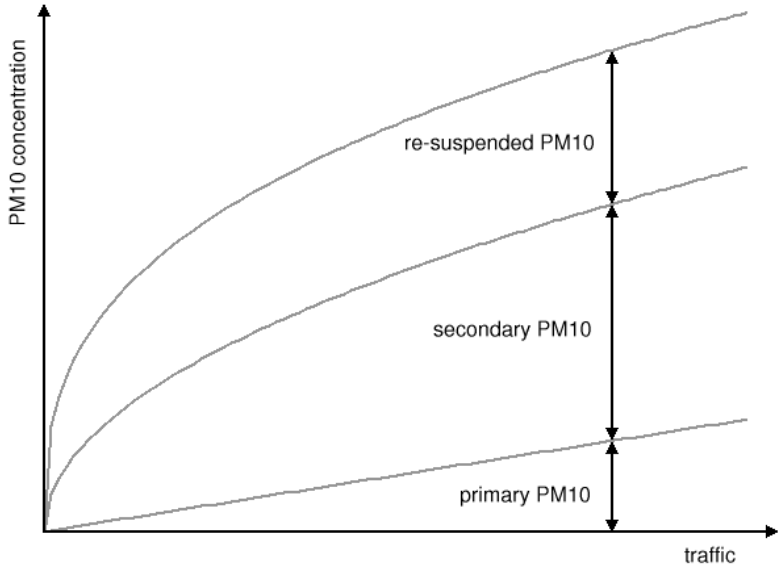

Figure 5.14.: Contribution to traffic-derived PM_{10} (qualitative sketch).

earth's surface play a major role, due to chemical absorption: for example, the rate of deposition in forests is greater than in open fields, deserts, and urban areas.

- Vertical mixing: depending upon atmospheric conditions and advective transport time, the vertical mixing spatial scale can range from few meters to thousands of meters; deposition is of course more rapid if the particulate matter plume is shallow and at ground level.

Resuspension of road dust can make a significant contribution to the local PM_{10} concentration, as shown by the roadside measurements issued by the Airborne Particle Expert Group (1999). Resuspended particles belong to a coarser size range than exhaust emissions.

As a conclusion, from considerations derived from Singles and McHugh (2003); Apsley et al. (2000, 2003); Eskridge et al. (1991); Airborne Particle Expert Group (1999); Ntziachristos and Samaras (2000); Hinds (2001) it can be assumed that PM_{10} derived from traffic doesn't increase linearly, but their contribution varies depending on traffic intensity and background concentrations of other chemically reacting pollutants. Figure 5.14 shows an hypothetical partitioning among primary, secondary and resuspended contributions to total PM_{10} concentration. While primary fraction can be reasonably assumed to increase linearly with traffic (superposition effect), this hypothesis is no longer valid for the resuspended part. In fact, dust resuspension due to vehicle transit is present also at low traffic intensity; moreover, high traffic in an urban area probably implies lower vehicles speed, leading to a variation in the ratio between primary and resuspended particulate. On the other hand, secondary produced particulate matter is related to concentration of other compounds produced not only by traffic (thus not proportional to traffic intensity); moreover emission factors of these compounds vary with vehicle speed. The partitioning of PM_{10} concentration in terms of the above contributions is in any case still poorly understood and would need further study. Figure 5.14 should therefore be intended as a qualitative sketch.

6. Numerical modelling

6.1. The case of Trento

Comprehensive studies referring to urban areas characterized by mixed canyon and non-canyon behaviour, like in the case of the town of Trento (Northern Italy), are presently not available. An attempt is pursued herein to solve the above problem, combining the peculiar features associated with urban areas with those related to roads in open field. In particular, the wake turbulence due to vehicles movements and that related to vertical thermal eddies will be treated separately, through the introduction of two different turbulent diffusion coefficients.

The case study of Trento is presented herein. The extension of the computational domain is about $1 \times 2\,km$ and covers the center of the town; we may notice that in part of it traffic is prevented, while some streets carry a high traffic load, which is characterized, as usual in urban areas, by a well-defined daily cycle. A detailed digital elevation map (with $1\,m$ horizontal resolution) is used to describe the domain, along with distributed traffic data, from which emission factors for each street link can be derived.

Air quality data are used for the validation of such a model; in turn the model can help in understanding whether monitored data are adequately distributed in space. In fact, "large area" models, simulating traffic emission as diffused area sources, although very useful for regulatory purposes, are not able to catch small scale spatial variation in concentration, which could nevertheless be quite strong. As we will see, even working at an "urban scale", the resolution could be not enough to characterize the secondary flow occurring within the urban structure, so that a "street scale" model has to be applied.

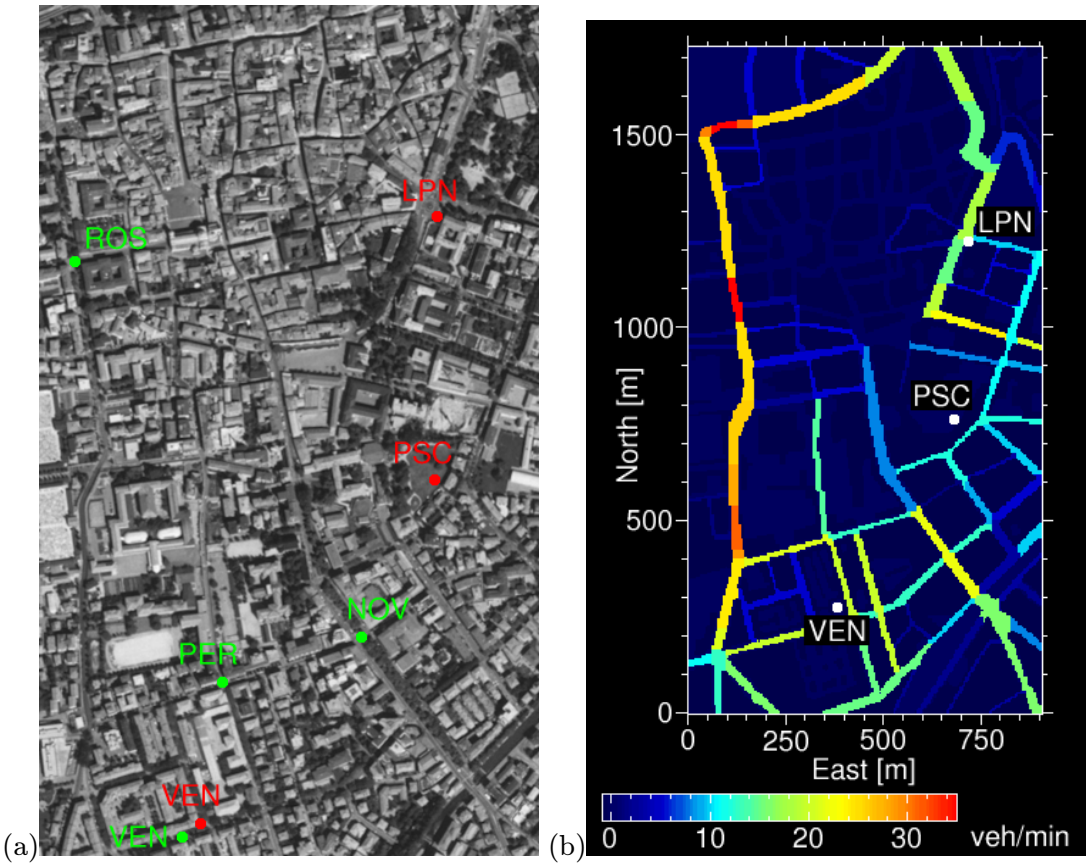

Figure 6.1.: a) Orthoimage with air quality stations operated by the local Environmental Protection Agency (APPA-Trento) in the locations named Parco Santa Chiara (PSC), Via Vittorio Veneto (VEN), Largo Porta Nuova (LPN); four examples of traffic monitoring sites, for which graphics are provided in figures (6.2) and (6.3), are reported in green: Corso III Novembre (NOV), Via Perini (PER), Via Vittorio Veneto (VEN), Via Rosmini (ROS).
b) *CO* emission factors for the street of the studied domain; the central area is a "no-traffic zone" and has therefore null values.

6.2. Traffic flow and emission factors

A set of traffic data measured on tenth of streets in the town of Trento has been made available by the local authorities (for details see Zanoni, 2002). On the whole set of traffic data, October and November 2001, the COPERT III procedure proposed by Ntziachristos and Samaras (2000) has been applied in order to derive the strength of emission sources. The COPERT III procedure, adopted by the European Environmental Agency estimates, on the basis of fuel consumption, the emissions of all regulated air pollutants (CO, NO_x, VOC, PM_{10}, CH_4, SO_2, C_6H_6) produced by different vehicle categories: passenger cars, light duty vehicles, heavy duty vehicles, mopeds and motorcycles.

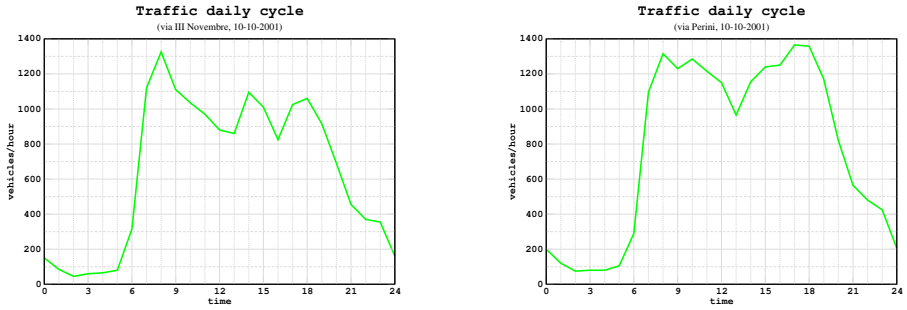

(a) (b)

Figure 6.2.: Traffic daily cycle at a) NOV and b) PER monitoring site (location is reported in figure 6.1).

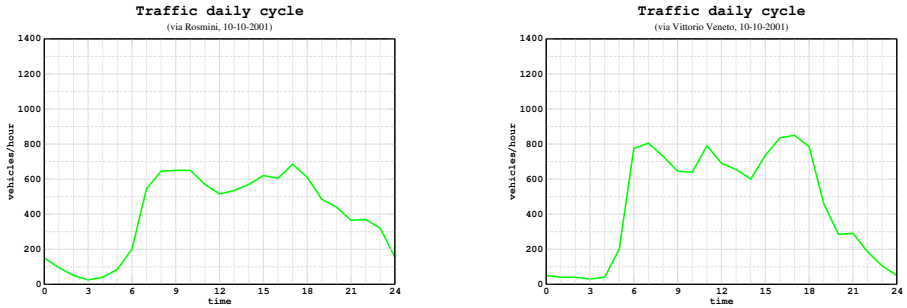

(a) (b)

Figure 6.3.: Traffic daily cycle at a) ROS and b) VEN monitoring site (location is reported in figure 6.1).

Estimated emissions are divided in three source types:

- hot emissions = produced during thermally stabilized engine operation;
- cold emissions = occurring during engine start (cold-start and warming-up effects);
- evaporation = NMVOC (non-methane volatile organic compounds) emissions due to fuel evaporation.

Total emissions are then calculated as the product of activity data and speed-dependent emission. The emission factor is generically defined for every street and vehicle type as:

$$EF_{ij} = f(road, vehicle), \tag{6.1}$$

where i represents the vehicle class and j the road class. For every street an average emission factor can be defined weighting the pollutant emissions on the N classes of the vehicle composition:

$$EF_j = \sum_{i=1}^{N} EF_{ij} p_i. \tag{6.2}$$

In figure 6.4 the flow diagram of the procedure is schematically reported, while the diagram of figure 6.5 shows the vehicles fleet composition (data provided by ACI Trento) and the computed emission factors for the regulated pollutants. As one can easily understand, some compounds are mainly related to a definite vehicle type. For instance PM_{10} and NO_x are mainly released by (diesel) heavy duty vehicles, although their number in the urban area is quite small; on the contrary passengers cars, both diesel and unleaded benzine fed vehicles, are the principle responsible for VOC and CH_4 emissions. Considering that tracks covered by car in urban area are usually short, 70% of emissions have been considered to occur in cold emission regime, as warming-up effects may last up to 15 minutes.

The emissions provided from the COPERT procedure $[g/(km \cdot h)]$ are finally converted to emission per unit length $[g/(m \cdot s)]$, thus characterizing each street link (figure 6.1).

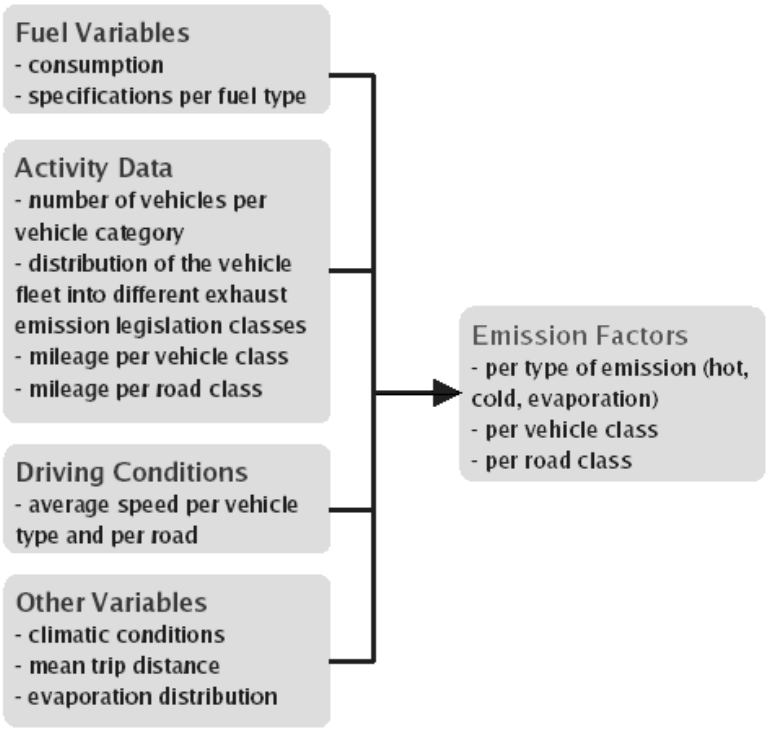

Figure 6.4.: COPERT III procedure scheme.

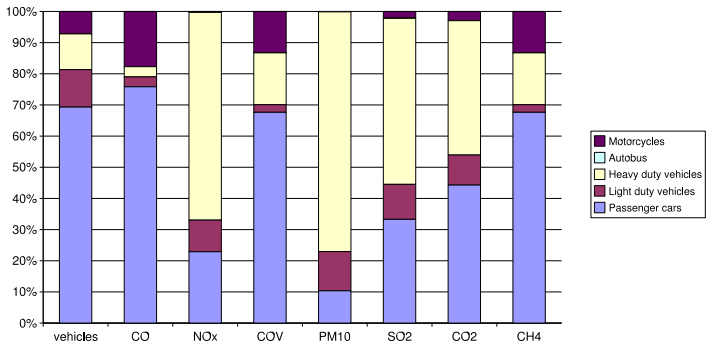

Figure 6.5.: Vehicle fleet composition in Trento and related averaged emission factors in urban areas (speed $V \leq 50\,km/h$).

6.3. A 3D eulerian model

A dispersion model has been developed, which is suitable for the estimate of traffic-derived air pollution; it is based on a high resolution map which provides information on the height of buildings within the urban area and on traffic data continuously monitored in several points. In the present case concentration data of several pollutants measured through air quality stations located within the urban area of Trento are available.The calculus domain along the vertical direction is divided in two parts: in the lower layer the pollutant is assumed to spread only due to diffusion, while in the upper layer, whose lower limit is fixed by the average height of the buildings, advection is also taken into account. The average wind speed above the buildings level is supposed to be uniform in space. The diffusion coefficient in the lower layer results from two contributions: the first is related to atmospheric stability, the second is the mechanical turbulence induced by the transit of motorvehicles.

A finite difference module is applied at the urban scale, explicitly resolving the roughness accounting for linear sources. The dispersion equation is solved by means of a finite differences explicit scheme, described in section 6.3.1. As far meteorological data, the wind velocity at reference point is collected by measurements stations outside the studied urban site (in rural area, at Trento airport), and reported to this context with the modified z_0 value and shifting the profile of the quantity z_d:

$$U_{urb}\left(z + z_d\right) = U_{rur}\left(z\right), \tag{6.3}$$

where $U_{rur}\left(z\right)$ has the form (1.10).

Wind direction is considered not to change over the roof level in the considered area. On the other side, turbulent diffusivity data are not available and this parameter has to be estimated indirectly.

As the dispersion in an urban area like the town of Trento is in a mixed wake- and skimming flow regime, dispersion should be computed accounting both for vehicle-induced turbulence and recirculation inside the streets. The portion of the plume within the obstacle canopy can be expected to be well mixed, because of the low advection velocity and the high turbulence intensity in the recirculating secondary flows.

The proposed procedure splits the vertical column in two zones where K_z is computed (figure 6.6): inside the roughness, that is $z < h$, K_z is supposed to coincide to mechanical induced turbulence. This hypothesis can be retained as valid, at least under low wind conditions, as the vehicle movement creates additional turbulence and, possibly, mean flows

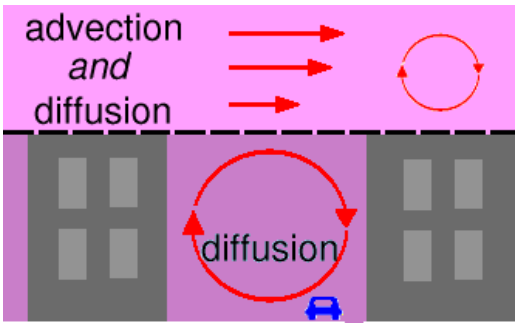

Figure 6.6.: The domain is divided into two layers: in the lower only diffusion is accounted for; in the upper one both advective and diffusive transport are considered.

that become important with respect to thermal turbulence. Hence, K_z can be written as:

$$K_z = T_L \sigma^2_{W,traffic}, \tag{6.4}$$

where $\sigma_{W,traffic}$ is proportional to vehicles speed and density and $T_L = 200\,s$; the procedure adopted to derive the above quantities is described more in detail in section 6.4.1.

On the other hand, in the upper layer, the mixing capacity follows a similarity law, according to classic theory, and the profile is displaced of the quantity z_d, as for wind speed. The horizontal dispersion coefficient is linearly related to vertical one as in section 4.1.2:

$$K_{x,y}(z) = c_1 \cdot K_z(z). \tag{6.5}$$

c_1 is an order 1 coefficient, which is used as calibration parameter. For simplicity, only diffusion is considered within the lower layer; the model is therefore suitable only for low wind conditions ($U < 2\,m/s$ at roof level).

Over a domain of about $2\,km^2$ a regular grid is generated starting from the digital elevation map (an example is displayed in figure 6.7); cells are classified in three types, distinguished in figure 6.8 by the following colors:

- yellow: domain cells where source term is positive (streets);
- green: domain cell where source term is null (sidewalks, parks, parking areas, streets with no traffic);
- black: cells not belonging to computational domain (buildings).

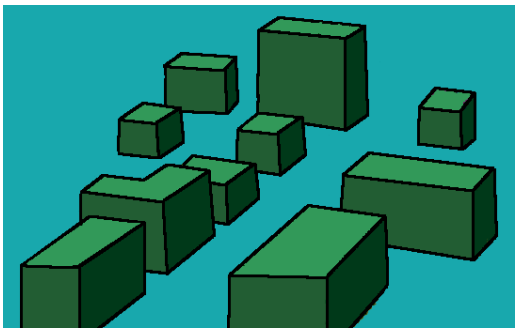

Figure 6.7.: High resolution digital elevation map.

As diffusion in source cells is supposed to be strongly related to mechanical turbulence induced by vehicles, these cells are considered to be completely mixed at emission time. A grid size of $\Delta x = \Delta y = 5\,m$ and $\Delta z = 3\,m$ is chosen, while the the time step Δt is variable, according to numerical stability condition (equation 6.16). Emissions per unit length are divided by the local width of the street (sidewalks not included) in order to derive the area emission for each cell $[g/(m^2 s)]$.

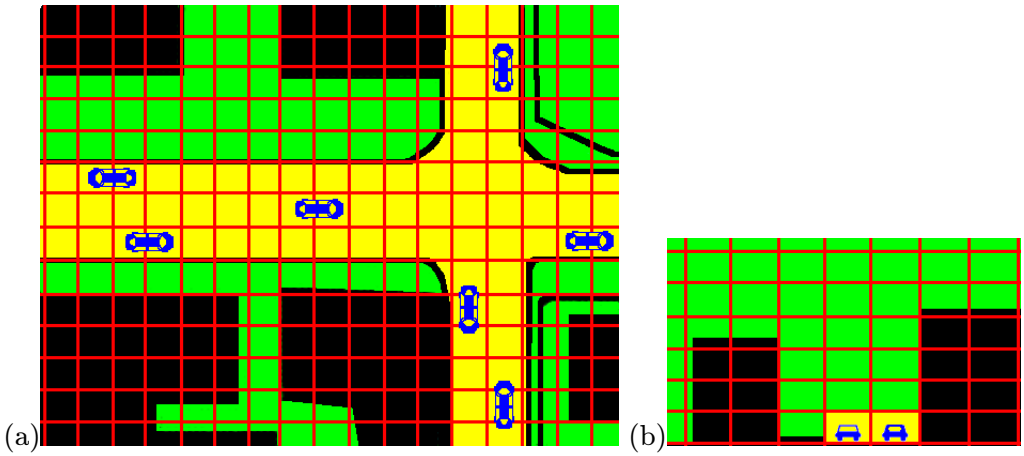

Figure 6.8.: Schematic grid discretization: a) plan view and b) vertical section.

6.3.1. Mathematical formulation

A finite volume formulation is adopted; the physical space is split up into volumes of suitable dimension and the partial differential equations integrated over each of these volumes. As the variables are approximated by their average values in each volume, and the fluxes

through the surfaces of each volume are approximated as function of the variables in neighbouring volumes, both the dimension of the cell and the elaboration time must be carefully evaluated, in order to achieve a sufficient resolved result in a reasonable time.

The dispersion is solved by means of a finite differences explicit scheme; the equation is written with $2D$ advection terms (in the horizontal plane) and $3D$ diffusion:

$$\frac{\partial C}{\partial t} + u\frac{\partial C}{\partial x} + v\frac{\partial C}{\partial y} = K_x\frac{\partial^2 C}{\partial x^2} + K_y\frac{\partial^2 C}{\partial y^2} + \frac{\partial}{\partial z}\left(K_z\frac{\partial C}{\partial z}\right) + S'. \tag{6.6}$$

An explicit method is used for discretization:

$$C_{ijk}^n = C_{ijk}^{n-1} + \underbrace{\Delta t\left(Ax_{ijk}^{n-1} + Ay_{ijk}^{n-1}\right)}_{advection\,term} + \underbrace{\Delta t\left(Dx_{ijk}^{n-1} + Dy_{ijk}^{n-1} + Dz_{ijk}^{n-1}\right)}_{diffusion\,term} + \underbrace{\Delta S_{ijk}^{n-1}}_{source\,term}. \tag{6.7}$$

The eddy diffusivity is supposed to vary only along the z direction; the diffusion terms assume therefore the following form:

$$\begin{cases} Dx_{ijk} = \frac{K_{x,k}}{\Delta x^2}\left(C_{i-1jk} - 2C_{ijk} + C_{i+1jk}\right) \\ Dx_{ijk} = \frac{K_{x,k}}{\Delta x^2}\left(C_{i-1jk} - 2C_{ijk} + C_{i+1jk}\right) \\ Dz_{ijk} = \frac{1}{\Delta z^2}\frac{K_{z,k-1}+K_{z,k}}{2}\left(C_{ijk-1} - C_{ijk}\right) + \frac{K_{z,k+1}+K_{z,k}}{2}\left(C_{ijk+1} - C_{ijk}\right) \end{cases}. \tag{6.8}$$

Parameterizations depending on air stability are used for vertical diffusivity coefficient K_Z. Horizontal diffusivity coefficients K_x and K_y are assumed to be proportional to K_z (Sozzi et al., 2002):

$$\begin{cases} K_z(z) = \frac{ku_* z}{\Phi\left(\frac{z-z_d}{L_{MO}}\right)} \\ K_{x,y}(z) = c_1 K_z(z) \end{cases}. \tag{6.9}$$

For the advection term the Lax-Wendroff method is adopted, in the form proposed by Leveque (1996), which achieves better accuracy and strongly inhibits numerical diffusion; this numerical scheme is explicit, conservative and second order accurate in space. In fact, in the numerical explicit solution of the advection-diffusion equation a crucial problem is the numerical diffusion which is introduced in discretizing the advection term. In order to reduce this error as much as possible, the Lax-Wendroff method introduces an "anti-diffusive" term. For example, in the x direction, the original advection term in the cell i at time n

$$u_i^n \left.\frac{\partial C}{\partial x}\right|_i^n \tag{6.10}$$

becomes:

$$u_i^n \left.\frac{\partial C}{\partial x}\right|_i^n - \left.\frac{\partial^2 C}{\partial x^2}\right|_i^n \left[(u_i^n)^2 \frac{\Delta t}{2} - u_i^n \frac{\Delta x}{2}\right]. \tag{6.11}$$

The advective term is thus composed by extra terms with respect to a standard upwind method:

$$\begin{cases} Ax_{ijk} = & -\frac{|\mathrm{Co}_{x,ijk}|}{\Delta t}\left(C_{ijk} - C_{Ljk}\right) \\ & -\frac{|\mathrm{Co}_{x,ijk}|\Lambda_{x2,ijk}}{2\Delta t}\left(1 - |\mathrm{Co}_{x,ijk}|\right)\left(C_{Mjk} - C_{ijk}\right) \\ & +\frac{|\mathrm{Co}_{x,ijk}|\Lambda_{x1,ijk}}{2\Delta t}\left(1 - |\mathrm{Co}_{x,ijk}|\right)\left(C_{ijk} - C_{Ljk}\right), \\ Ay_{ijk} = & -\frac{|\mathrm{Co}_{y,ijk}|}{\Delta t}\left(C_{ijk} - C_{iPk}\right) \\ & -\frac{|\mathrm{Co}_{y,ijk}|\Lambda_{y2,ijk}}{2\Delta t}\left(1 - |\mathrm{Co}_{y,ijk}|\right)\left(C_{iQk} - C_{ijk}\right) \\ & +\frac{|\mathrm{Co}_{y,ijk}|\Lambda_{y1,ijk}}{2\Delta t}\left(1 - |\mathrm{Co}_{y,ijk}|\right)\left(C_{ijk} - C_{iPk}\right), \end{cases} \tag{6.12}$$

where $\mathrm{Co}_{x,y}$ are the Courant numbers in the two horizontal directions:

$$\begin{cases} \mathrm{Co}_{x,ijk} = u_{ijk}\frac{\Delta t}{\Delta x} \\ \mathrm{Co}_{y,ijk} = v_{ijk}\frac{\Delta t}{\Delta y} \end{cases}, \tag{6.13}$$

and Λ is the "minmod" limiter as defined by Leveque (1996):

$$\begin{cases} \Lambda_{x1,ijk} = \max\left[0, \min\left(1, \frac{C_{Ljk} - C_{Njk}}{C_{ijk} - C_{Ljk}}\right)\right] \\ \Lambda_{x2,ijk} = \max\left[0, \min\left(1, \frac{C_{ijk} - C_{Ljk}}{C_{Mjk} - C_{ijk}}\right)\right] \\ \Lambda_{y1,ijk} = \max\left[0, \min\left(1, \frac{C_{iPk} - C_{iRk}}{C_{ijk} - C_{iPk}}\right)\right] \\ \Lambda_{x2,ijk} = \max\left[0, \min\left(1, \frac{C_{ijk} - C_{iPk}}{C_{iQk} - C_{ijk}}\right)\right] \end{cases}. \tag{6.14}$$

The indexes L, M, N and P, Q, R are defined as:

$$\begin{cases} L = i - \mathrm{sgn}(u) \\ M = i + \mathrm{sgn}(u) \\ N = i - 2\,\mathrm{sgn}(u) \\ P = j - \mathrm{sgn}(v) \\ Q = j + \mathrm{sgn}(v) \\ R = j - 2\,\mathrm{sgn}(v) \end{cases}. \tag{6.15}$$

As the described numerical scheme is explicit, a stability condition Co ≤ 1 is required; the maximum time step Δt_{max} for a regular-spaced grid is therefore derived:

$$\Delta t_{max} \leq \frac{1}{\frac{u}{\Delta x} + \frac{v}{\Delta y} + 2\frac{K_x}{\Delta x^2} + 2\frac{K_y}{\Delta y^2} + 2\frac{K_z}{\Delta z^2}}. \tag{6.16}$$

6.3.2. Deposition

An additional deposition term should be added to the advection term in (6.6) for simulating gravitational settling, namely:

$$- w_G \frac{\partial C}{\partial z}. \tag{6.17}$$

Indeed, these terms only play a role when simulating suspended particles transport, as one can deduce from figure 5.12. Deposition mechanisms, both "dry" and "wet", are taken into consideration to determine the vertical term in (6.17), as described in section 5.5.1.

For gaseous pollutants, on the contrary, at least in the inferior level, diffusive vertical transport turns out to be dominant, i.e.:

$$\left| \frac{\partial}{\partial z} \left(K_z \frac{\partial C}{\partial z} \right) \right| \gg \left| w_G \frac{\partial C}{\partial z} \right|. \tag{6.18}$$

Hence, the deposition term can be neglected in this case. For calibration purposes we have considered gaseous pollutants, as explained below. PM_{10}, which is probably the only pollutant for which settling velocity is important in this context, is not used in the calibration of the model, as it shows a more complex behaviour (section 5.5.2.2).

6.3.3. Calibration and simulations

Among the various pollutants emitted by vehicles, CO is chosen as tracer for calibration; in fact, NO_x and PM_{10} are also secondary pollutants: this would therefore add uncertainty to the validation, while sulphur dioxide is in general related to diesel engine vehicles and gasoline domestic heating. In any case the aim is that of calibrating the model in terms of a pollutant which is mostly related to traffic emission. For CO the influence of industries is probably negligible in the area of the town of Trento; on the contrary, domestic heating could give a considerable contribute. However, the days used for calibration (10 and 11 October 2001) were quite warm; therefore domestic heating is supposed not to contribute to CO emission.

Further reasons for the choice of the above days are that low wind speed was observed for the entire period and that quite complete dataset of vehicle transit is available.

Simulations have been carried out with an integration time step of $\sim 10\,s$, as required by numerical stability condition; in order to compare results with measured concentrations, hourly averaged values are derived. Figures 6.9, 6.10 and 6.11 show some examples of CO concentration maps at ground level ($z = 1.5\,m$ in the middle of the first cell layer) and just above the mean roof level, at $z = 22.5\,m$.

6.3.4. Discussion

For such a kind of analysis, which refers to low level emission sources, concentration at ground level within urban network strongly depends on traffic conditions; however, highly unstable atmospheric conditions can reduce significantly the values of concentration. In fact stronger concentration are observed at $6\,AM$, under stable atmospheric condition; on the contrary, at $12\,AM$, when traffic emission is more intense by a factor of $2 \div 8$ (depending on the site, see figures 6.2 and 6.3), CO values tend to decrease and concentration pattern appear more smoothed, especially in the upper layer. Meteorological conditions mainly affect the pollutant concentration in the far field and determine the direction toward which the pollutant is transported in the middle range, as one can deduce comparing the time evolution of wind direction reported in figure 6.12 and the CO concentration patterns in the upper layer.

Some differences can be expected between the behaviour of streets located in open areas and street canyons. For example, the worst agreement between predicted and observed CO concentration is found at PSC monitoring station (figure 6.14), which is inside a park, whose mixing behaviour is for sure different from a typical urban context.

In fact, concentration gradients in the urban canopy decrease after the plume has encountered a few rows of obstacles. Moreover, traffic-induced mixing tends to reduce the very high concentrations that would otherwise result from street level emissions in calm conditions. Although concentration values are in the case of PSC lower (there is no emission right there) than in VEN and LPN stations, which instead correspond to streets carrying a heavy load of vehicles, relative errors have the same order of magnitude of the predicted values. On the other hand it is quite easy to calibrate the model for stations situated exactly on high traffic streets (VEN and LPN), where mixing conditions are less relevant. Unfortunately no concentration data are available for the "no-traffic" zone, which would better validate the proposed scheme.

On the other hand, figure 6.16 shows that the predicted behaviour for PM_{10} completely disagrees with respect to observed data; a possible explanation is that suspended particulate is in part resuspended and part of the total amount consists of secondary pho-

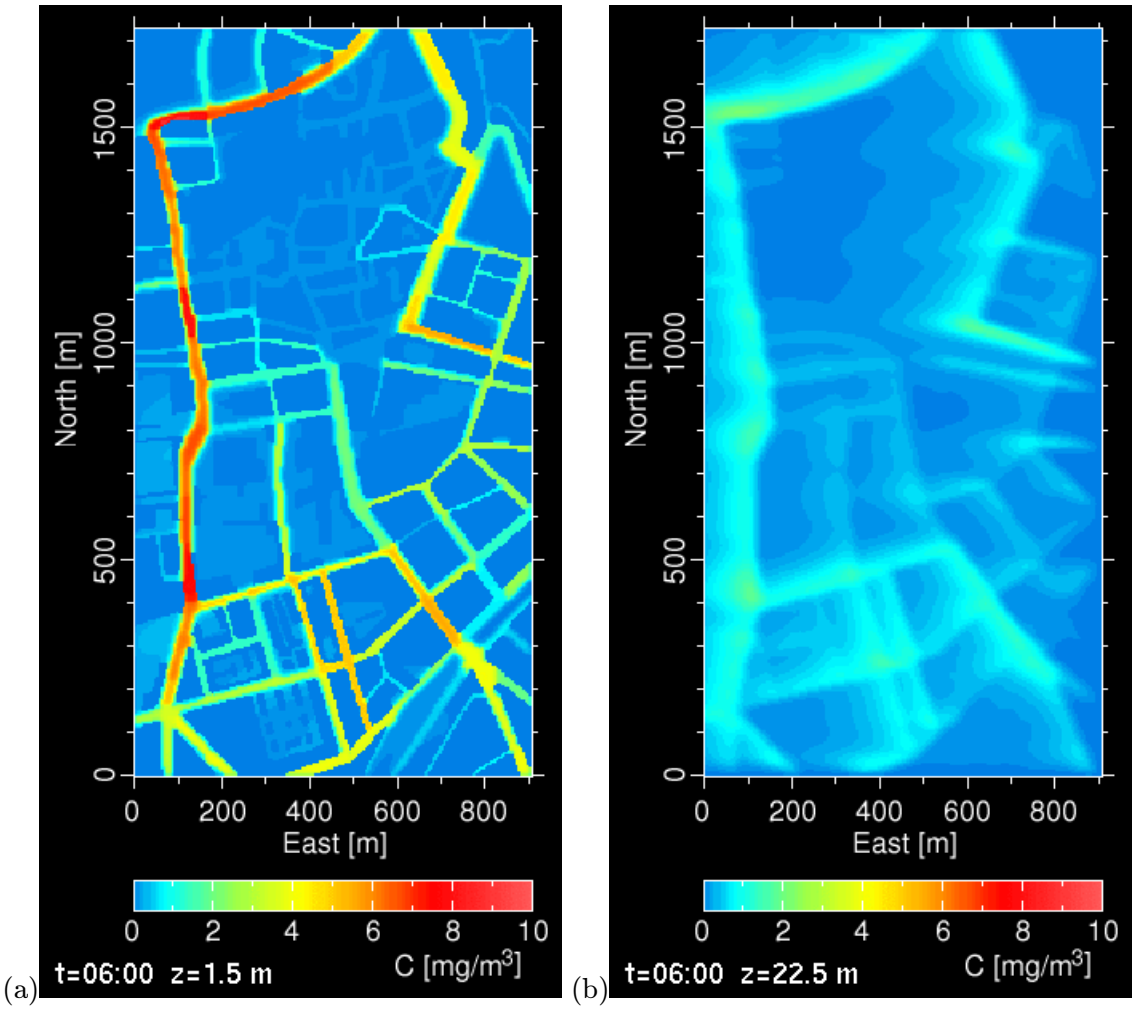

Figure 6.9.: Predicted CO concentration values on 10 October 2001, 6 AM at a) $z = 1.5\,m$ and b) $z = 22.5\,m$.

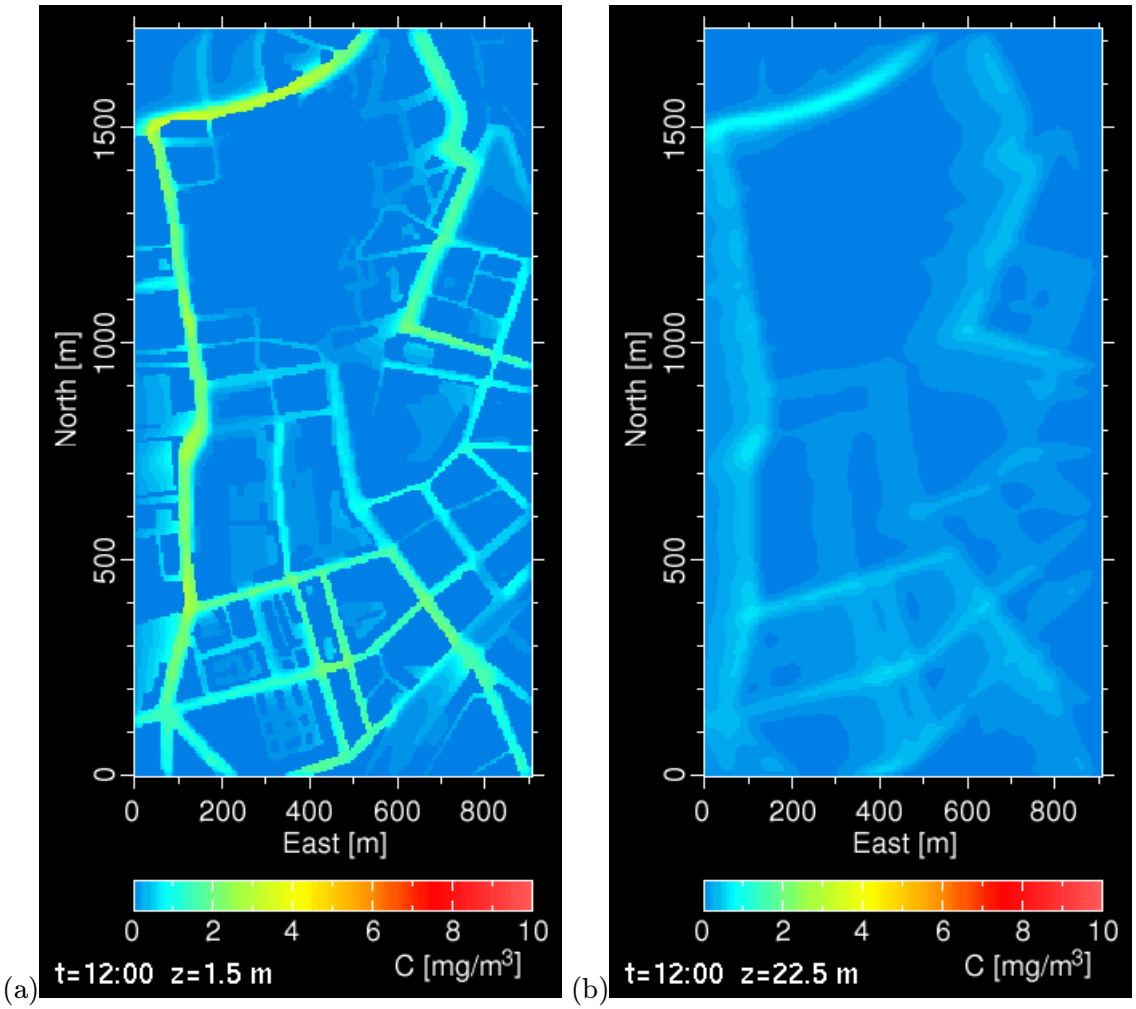

Figure 6.10.: Predicted CO concentration values on 10 October 2001, 12 AM at a) $z = 1.5\,m$ and b) $z = 22.5\,m$.

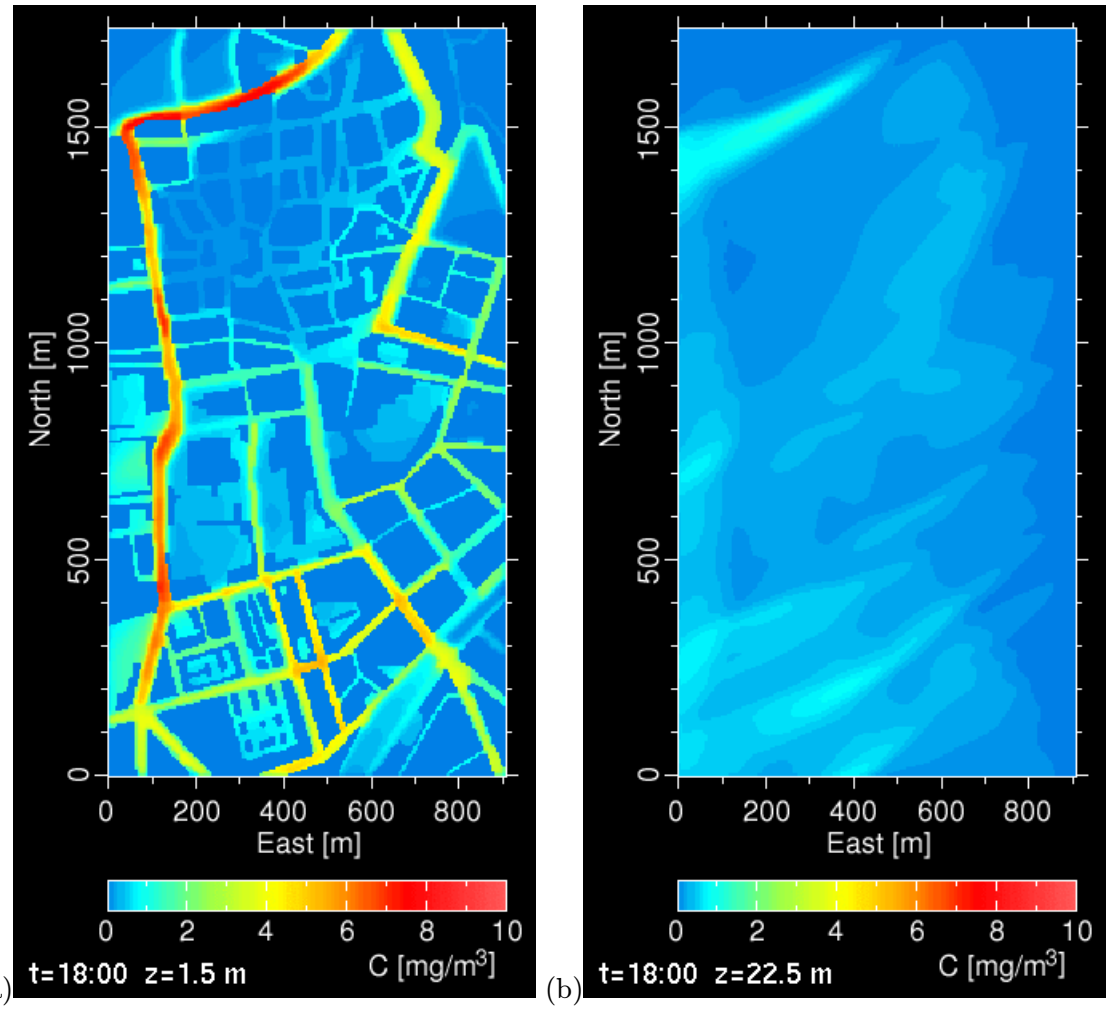

Figure 6.11.: Predicted CO concentration values on 10 October 2001, 6 PM at a) $z = 1.5\,m$ and b) $z = 22.5\,m$.

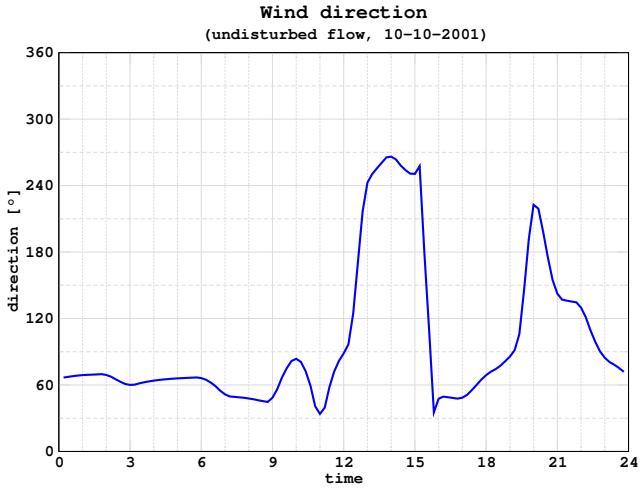

Figure 6.12.: Measured wind direction over the domain, on 10 October 2001.

tochemically produced compound, as explained in section 5.5.2. As a matter of fact, the larger deviation is found during night-time, with a lag time which is probably related to the chemical transformation time scale.

On the vertical direction, as can be derived from the comparison between CO color maps at ground level and at roof level, a strong variation in concentration should be expected. A direct comparison with a classic gaussian model is for this reason quite hard to perform, as in the latter approach the roughness is parametrized and the 0-level is not actually at street surface but at z_d level, that is approximatively at roof's height.

Finally, it should be remembered that it is reasonable to apply a high resolution model, like the one proposed herein, when a large amount of data describing traffic and streets layout is available. Moreover, the model seems to produce reliable results only for quite compact urban structure and when the wind speed is low enough so that advection is not dominant along the street paths.

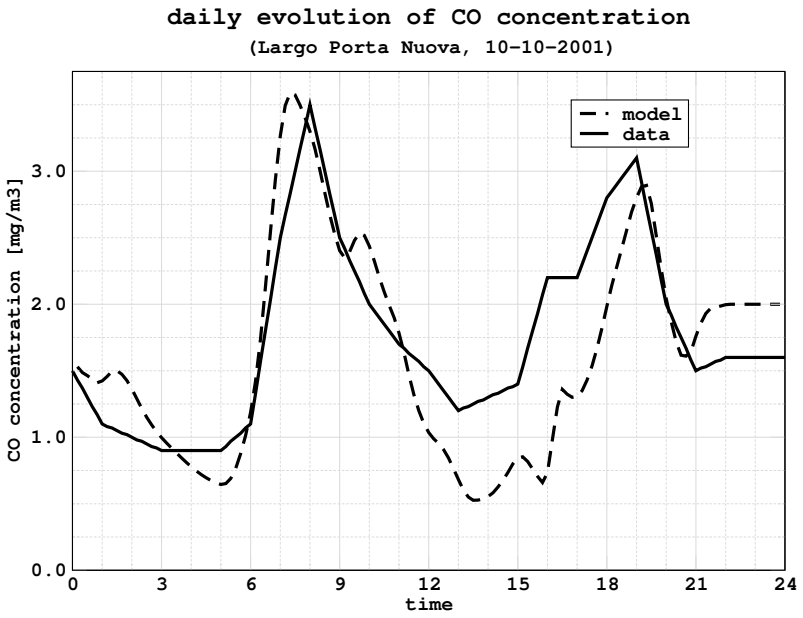

Figure 6.13.: Measured and modelled *CO* concentration at LPN air quality station, on 10 October 2001.

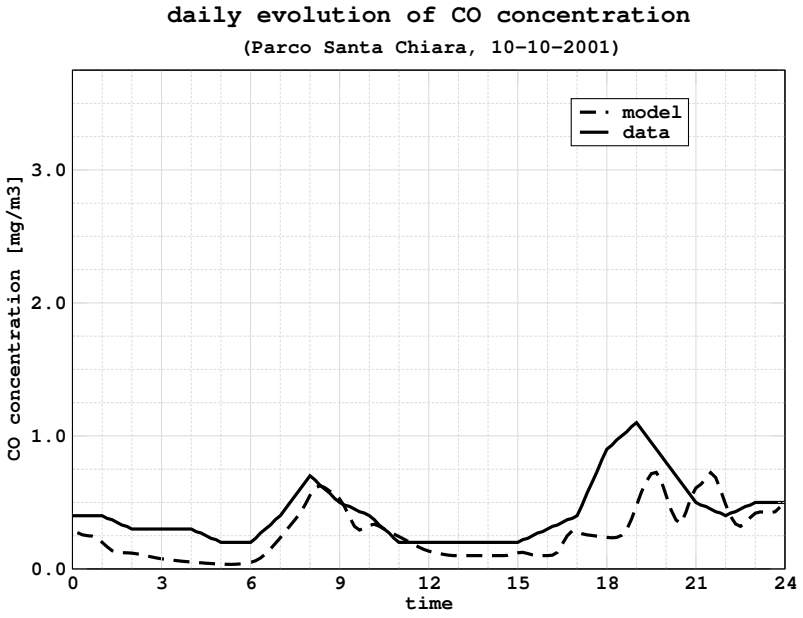

Figure 6.14.: Measured and modelled *CO* concentration at PSC air quality station, on 10 October 2001.

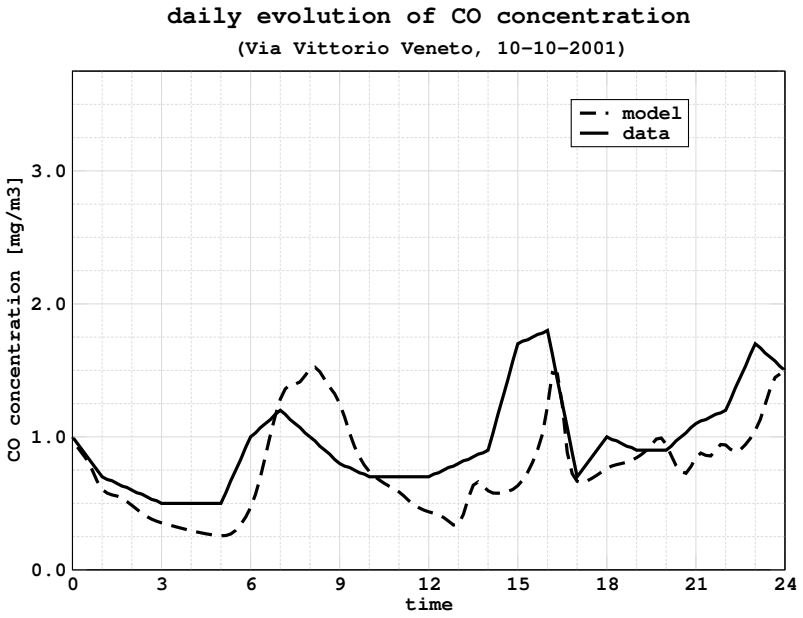

Figure 6.15.: Measured and modelled CO concentration at VEN air quality station, on 10 October 2001.

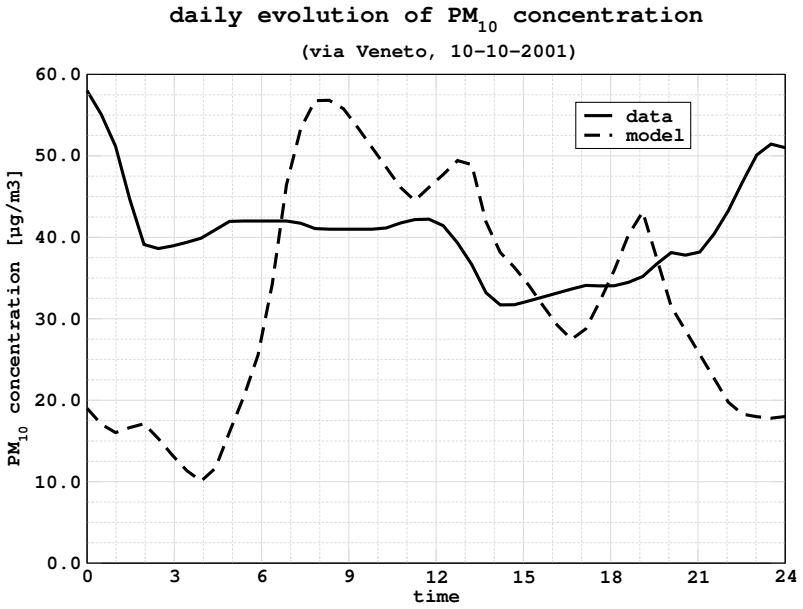

Figure 6.16.: Measured and modelled PM_{10} concentration at LPN air quality station, on 10 October 2001.

6.4. 2D lagrangian model

6.4.1. Formulation of the model

In order to investigate more in detail the mixing behaviour at the "street scale", a two-dimensional $x - z$ particle-tracking lagrangian dispersion model has been developed. This approach turns out to be necessary for near field dispersion, when the emission source is located inside the roughness and the impact area entirely falls inside the near field.

The proposed numerical model is applied on a fairly homogeneous urban structure. The procedure consists of three steps:

- approximated calculation of mean flow field;
- turbulence parametrization;
- lagrangian particle tracking modelling.

The model is suitable for the calculation of atmospheric pollution within non homogeneous urban fabric. The $2D$ flow is estimated imposing an undisturbed vertical wind profile which is modified by the presence of buildings, according to their distance, height and form. The flow perpendicular to street axis is considered, in order to investigate the canyoning effects and the short range diffusion (Kaplan and Dinar, 1996).

The calculus domain along the vertical direction is divided in two parts: in the upper layer, whose lower limit is fixed by the height of the buildings, the flow field is given by the wind profile modified to account for the effect of buildings; in the lower layer, canyoning effects and recirculation are considered, using Bottema (1997) model which allows one to determine the areas of influence of each building where vorticity is generated. Inside these zones the simple model of Hotchkiss and Harlow (1973) is adopted to calculate, as a first approximation, the recirculating flow. The flow field is then adjusted by minimizing divergence over the whole computational domain (both upper and lower layer). The wind speed, as well as the turbulent diffusivity, are supposed not to be uniform in time. The diffusion coefficient in the lower layer results from two contributions: the first is the turbulence induced by solar forcing, the second is the mechanical turbulence induced by the transit of motor-vehicles.

The lagrangian model allows one to simulate accurately the spatial variation of turbulent diffusivity. Numerical simulations require the tracking of a large number of particles which represent the emissions arising from single point sources (motor-vehicles).

6.4.1.1. Mean flow field

Air flow around buildings is characterized by an eddy vortex due to flow down the windward facade, while behind it a lee eddy establishes drawn into the cavity of low pressure due to flow separation from the sharp edges of the building top and sides, and further downstream the building wake develops, characterized by increased turbulence but lower horizontal speeds than the undisturbed flow (Röckle, 1990; Santamouris and Dascalaki, 2003). As mentioned in section 5.3, knowledge of the air flow characteristics in urban canyons is necessary for all studies related to natural ventilation of buildings and pollution studies. Urban canyons are characterized by three main parameters, the mean height of the buildings in the canyon, the canyon width and the canyon length. In the present study the third is neglected as the study is restricted to the bidimensional case.

As shown before (figure 5.9) two approaches can be used to distinguish the two layer of recirculating flow ("inner") and of nearly potential flow ("outer").

All methods using z_0, z_d and the logarithmic wind profile

$$U(z) = \frac{u_*}{k}\left[\ln\left(\frac{z - z_d}{z_0}\right) - \Psi\left(\frac{z - z_d}{L_{MO}}\right)\right] \tag{6.19}$$

describe the vertical wind profile above the roughness sublayer, as if the air flow were in equilibrium with a level homogeneous surface. Among other consequence, this leads to the consideration that measurements should be taken above the roughness sublayer, and that derived quantities should be considered as not disturbed by turbulence generation at the interface (with respect to a hypothetical uniform surface displaced at the height z_d).

A local approach (figure 5.9b) is in the present case preferable and has been therefore adopted, as it accounts explicitly for the obstacles; this is quite relevant, because this model is designed to handle near field diffusion, which mainly occurs inside the roughness.

In the present work Bottema (1997) model is used to estimate the extension of the recirculation zones, depending on the mean flow and the geometric characteristics of the buildings (see section 5.3.1):

$$\frac{B_R}{H} = c\frac{L}{L + 2H}; \tag{6.20}$$

the parameter c ranges about 1 for upwind recirculation cavity and equals 3 for downwind cavity (see also Pardyjak et al., 2002; Bagal et al., 2002).

A "first trial" flow field is computed using the undisturbed wind profile shown in (6.19), or alternatively through the formula

$$u = u_{mis}\left(\frac{z}{z_{mis}}\right)^{n}, \tag{6.21}$$

where the exponent n depends on atmospheric stability; furthermore, on each vertical column, outside the recirculation zones, the conservation of the mass is imposed:

$$\int_{z_{inf}}^{z_{top}} U(x,z)dz = const, \tag{6.22}$$

where z_{top} is the height of the computational domain, which is set at least 5 times the buildings height. The U, W field is then estimated inside the canyon on the basis of geometric parameters and of previously estimated velocity U_0 above the canyon; the drag effect on the air mass below induces a circulation. The model proposed by Hotchkiss and Harlow (1973) is adopted: it considers incompressible flow, absence of sources or sinks of vorticity within the canyon, and boundary conditions given by $2D$ rectangular cavity of depth H and width S. The used expression for horizontal and vertical wind speed components are (figure 6.17):

$$\begin{cases} U(x,z) = \frac{U_0 \sin(kx)}{1-\beta}\left[\gamma(1+k\gamma) - \beta\frac{1-k\gamma}{\gamma}\right] \\ W(x,z) = \frac{U_0 \cos(kx)}{1-\beta}(z-H)k\left(\frac{\beta}{\gamma} - \gamma\right) \end{cases}, \tag{6.23}$$

where $k = \frac{\pi}{S}$, $\beta = \exp(-2kH)$and $\gamma = \exp\left[k(z-H)\right]$, U_0 is the previously estimated velocity above the canyon at the point $x = \frac{B}{2}$ and $z = H$. The U, W mean flow field is then adjusted minimizing divergence on the whole domain, also in order to satisfy continuity at the interface between the two zones.

6.4.1.2. Turbulence parametrization

The assumption that turbulence inside the canyon is mainly induced by vehicle transit is adopted, assuming that it is dominant over the thermal turbulence induced by solar forcing; this approach is presented in the Operational Street Pollution Model (OSPM), described in Berkowicz et al. (1997).

A simplified parametrization for both the wind- and the traffic-induced turbulence has been adopted (Berkowicz, 2000):

$$\sigma_{W,traffic} = c\sqrt{V_v N_v \frac{A_v}{S}}, \tag{6.24}$$

where $V_v\,[m/s]$ is the average vehicle speed; c [-] is a constant factor related to the

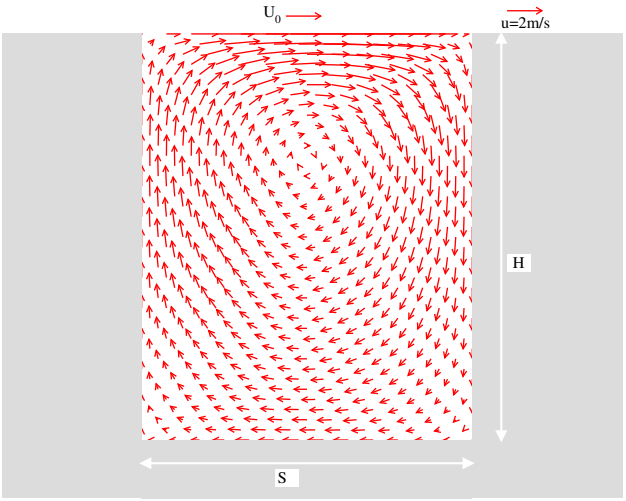

Figure 6.17.: Flow field in an urban canyon computed according to Hotchkiss and Harlow (1973).

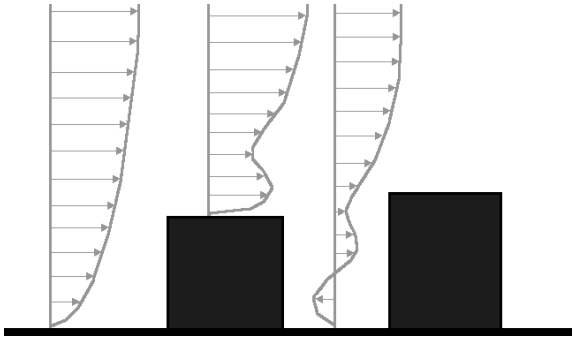

Figure 6.18.: Vertical wind profile modified by the presence of obstacles.

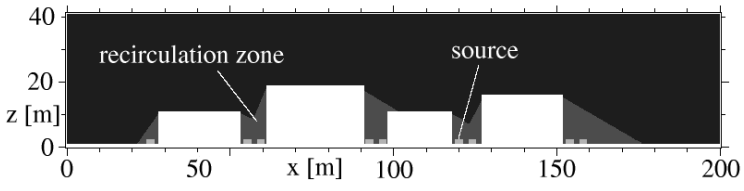

Figure 6.19.: Schematic recirculation zones according to Bottema (1997).

aerodynamic drag coefficient (according to Berkowicz, 2000 $c = 0.3$); $N_v\,[veh/s]$ is the number of vehicles passing in the street per time unit; $A_v\,[m^2/veh]$ is the plan area occupied by the single vehicle; $S\,[m]$ is the width of the street canyon. In absence of more detailed description of vehicle-induced turbulence, $\sigma_{U,traffic}$ is assumed as equal to the vertical component (equation 6.24).

On the other hand, over the roof level, wind induced turbulence is related to friction velocity, according to Gryning et al. (1987) and Stull (1988). Under stable conditions vertical and horizontal σ profiles are given by:

$$\begin{cases} \sigma_W = u_* \sqrt{1.7 \left(1 - \frac{z}{z_i}\right)^{3/2}} \\ \sigma_U = u_* \sqrt{6 \left(1 - \sqrt{\frac{z}{z_i}}\right)} \end{cases}, \tag{6.25}$$

while in the neutral and unstable cases read:

$$\begin{cases} \sigma_W = \sqrt{1.5 w_*^2 \left(\frac{z}{z_i}\right)^{2/3} \exp\left(-2\frac{z}{z_i}\right) + u_*^2 \left(1.7 - \frac{z}{z_i}\right)} \\ \sigma_U = \sqrt{0.35 w_*^2 + u_*^2 \left(2 - \frac{z}{z_i}\right)} \end{cases}. \tag{6.26}$$

In (6.25) and (6.26) u_* is the friction velocity, w_* is the vertical convective velocity scale, and z_i is the mixing depth.

6.4.1.3. Lagrangian model

As already discussed in chapter 3, lagrangian particle models are able to simulate both stationary and non-stationary emission sources; moreover, they are able to better reproduce the short range diffusion process; it is exactly the case of pollutant dispersion in an urban environment at a small spatial scale (Lee and Park, 1994; Rotach, 2001). In this time range (individuated by $t \leq T_L$) the assumption $\sigma^2 = 2Kt$ is not valid; it would actually imply a "constant K" hypothesis and therefore the lack of the memory term (see section 3.2.5). The near field diffusion process through an array of buildings can be well simulated by using a "2-equations" vertical two-dimensional lagrangian model: according to Thomson (1987) the equation integrating the trajectories of each particle are given by (see section 3.2):

$$\begin{cases} du = a_x dt + b_x dr \\ dw = a_z dt + b_z dr \end{cases}, \tag{6.27}$$

$$\begin{cases} dx = udt \\ dz = wdt \end{cases} . \tag{6.28}$$

Acceleration terms read:

$$\begin{cases} a_x = f\left(U, \frac{\partial U}{\partial t}, \frac{\partial U}{\partial x}, \sigma_U, \frac{\partial \sigma_U}{\partial t}, \frac{\partial \sigma_U}{\partial x}\right) \\ a_z = f\left(W, \frac{\partial W}{\partial t}, \frac{\partial W}{\partial z}, \sigma_W, \frac{\partial \sigma_W}{\partial t}, \frac{\partial \sigma_W}{\partial z}\right) \end{cases} , \tag{6.29}$$

while the stochastic term is related to the lagrangian time scale T_L and to turbulence parameters $\sigma_{U,W}$:

$$\begin{cases} b_x = \sqrt{\frac{2\sigma_U^2}{T_L}} \\ b_z = \sqrt{\frac{2\sigma_W^2}{T_L}} \end{cases} . \tag{6.30}$$

U, W are the mean eulerian velocities, calculated through procedure explained in section 6.4.1.1; u, w represent the lagrangian particle velocities; dt is the integration time step; dr is a pseudo-random number extracted from a gaussian PDF with 0 mean and variance dt. At the walls particles are reflected using a geometric criterion to simulate the null flux condition (or stopped to simulate deposition at the ground).

For the unstable atmosphere it is quite natural to connect the lagrangian time scale to the time of transport between the surface and the mixing height: $T_L = \frac{z_i}{\sigma_W}$, where σ_W is used as a characteristic velocity for the vertical spread of plumes. For atmospheric neutral conditions the mixing height in the usual sense for the convective atmosphere might not be present; in this case the vertical scaling height can be taken as $z_i = 0.2\frac{u_*}{f}$ (e.g. Garratt, 1992) where f is the Coriolis parameter. In urban environment a typical value for the lagrangian time scale is, if neglecting the height dependence of this parameter, about $200\,s$ for ground-level sources, while a value of $T_L = 600\,s$ is recommended for elevated sources(Gryning et al., 2003).

The proposed scheme assumes that $\sigma = \sigma_{traffic}$ inside the recirculation zone, and $\sigma = \sigma_{wind}$ outside; in other words σ is supposed to be constant in space in each of the two layers. Therefore, (6.29) assumes a simple form:

$$\begin{cases} a_x = -\frac{u-U}{T_L} + \frac{\partial U}{\partial t} + \frac{\partial \sigma_U^2}{\partial t}\left(\frac{u-U}{2\sigma_U^2}\right) \\ a_z = -\frac{w-W}{T_L} + \frac{\partial W}{\partial t} + \frac{\partial \sigma_W^2}{\partial t}\left(\frac{w-W}{2\sigma_W^2}\right) \end{cases} . \tag{6.31}$$

In order to achieve a sufficient resolution in the trajectory, the integration time step dt is set equal to $0.05T_L$: the release interval is subject to the same limitation reported in

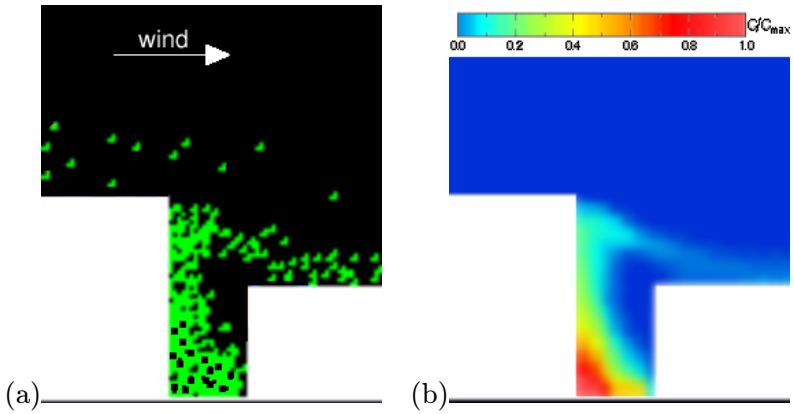

Figure 6.20.: Zoom of the concentration pattern inside the canyon. a) Snapshot of the lagrangian particle random walk and b) color-scale concentration map. Higher values occur on the leeward side.

section 4.1.3 for the LAG3D model .

COPERT III procedure (Ntziachristos and Samaras, 2000) is adopted to simulate vehicles' emission, as described in section 6.2.

6.4.2. Test simulation

Numerical simulations have been carried out in order to test the model. Situations of low and high wind speed and different atmospheric stability class have been analyzed, considering ground level sources located in three adjacent canyons, each characterized by the same traffic daily cycle and, therefore, by the same emission. It should be underlined that the dispersion time-scale variability is comparable to the traffic daily cycle; at least inside the canyon emission and concentration are strongly related, while in the upper layer the memory term is inverse-proportional to atmospheric stability.

Concentration is computed through the box-counting method, being proportional to the number of particles in each cell, under the hypothesis that each particle "carries" 1 mass unit.

Figures 6.21 to 6.24 show pollutant concentration in color-scale maps; concentrations are scaled with the maximum value.

6.4.3. Discussion

Trapping of pollutants inside the street in the leeward side is shown by the above results and is confirmed by various authors, e.g. Rotach (2001); Barlow et al. (2003). Moreover,

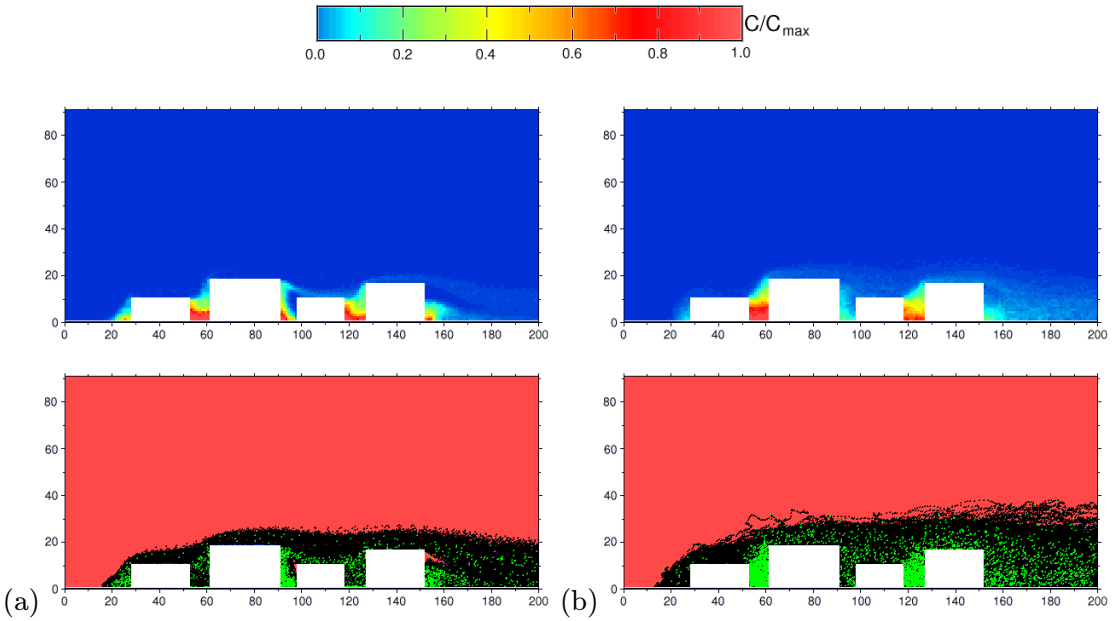

Figure 6.21.: Stable atmosphere: a) high wind speed and b) low wind speed.

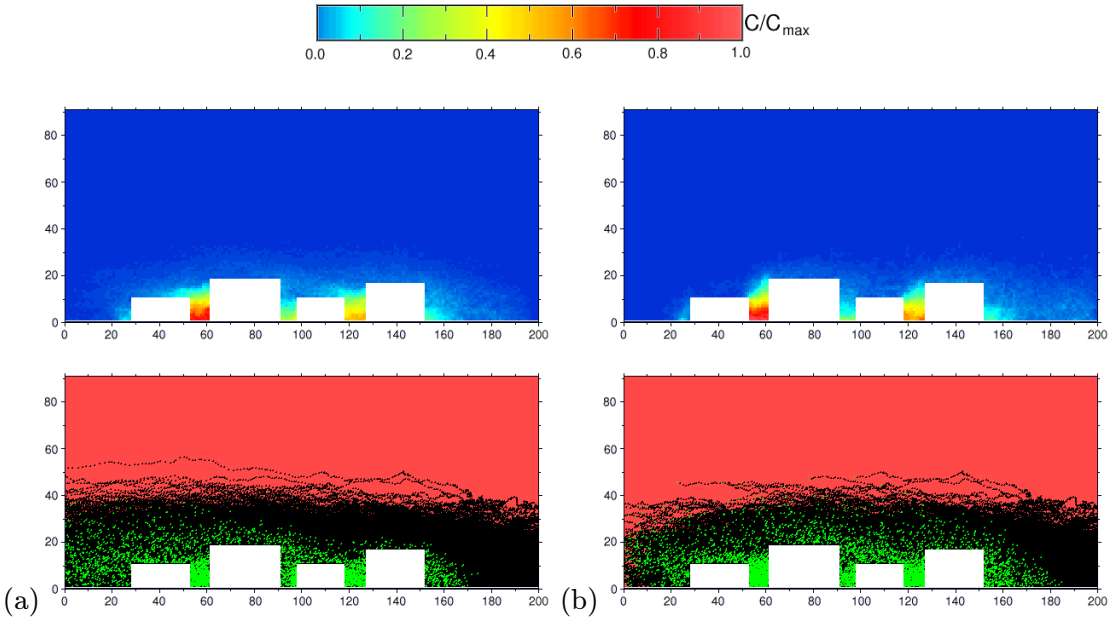

Figure 6.22.: Neutral atmosphere: a) high wind speed and b) low wind speed.

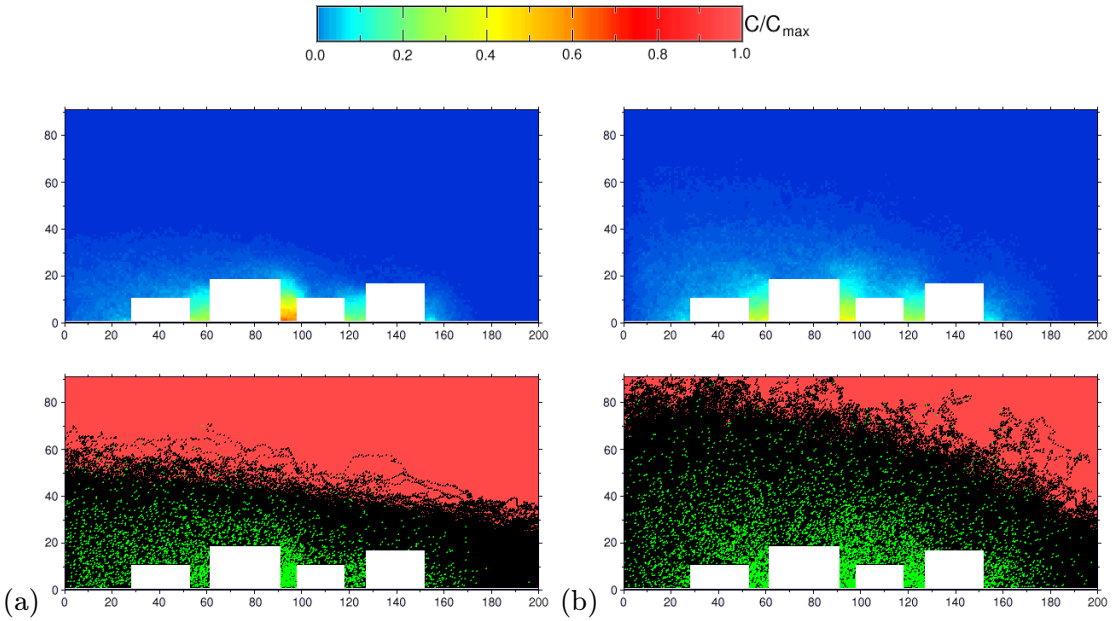

Figure 6.23.: Unstable atmosphere: a) high wind speed and b) low wind speed.

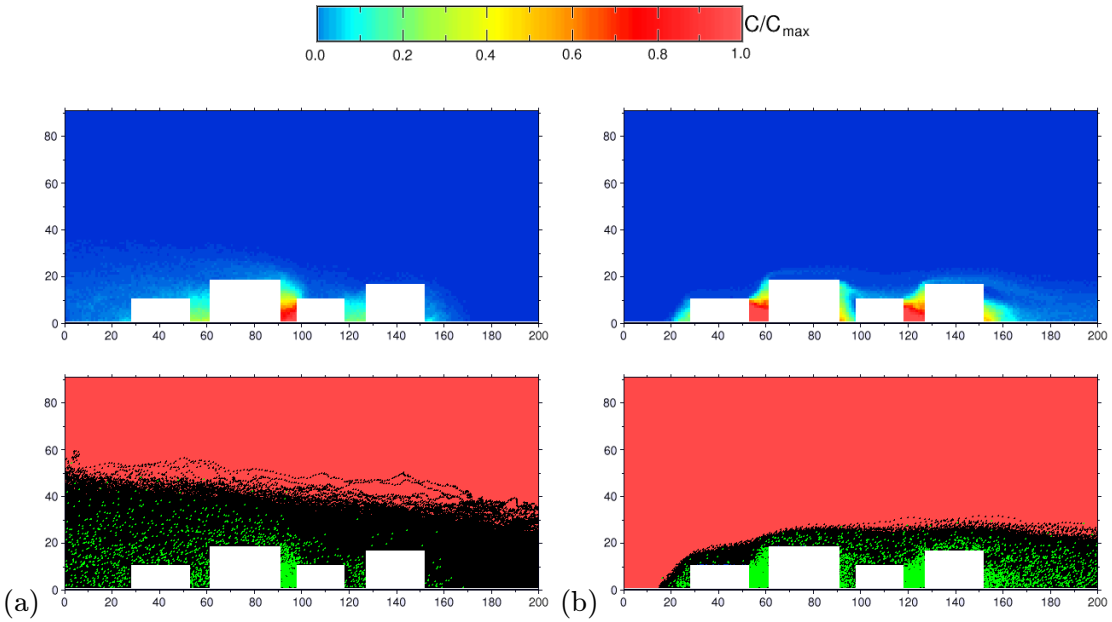

Figure 6.24.: Neutral atmosphere, switching of wind direction.

the concentration on the leeward side of the street can be much larger than that on the windward side, due to the cross-street circulation. This type of local dispersion behaviour creates strong concentration gradients and is poorly predicted by large-scale models.

Some key points can be evidenced, resulting from the performed simulations:

- Sheltering effects of higher buildings on lower ones determines different pollution patterns (see figure 6.24) in case of same emission and atmospheric stability class, but different wind direction.
- The vortex structure tends to be located in the upper part of the canyon: this results in relatively stagnant flow at the ground, and concentration levels much higher than those found in open field, all else conditions being equal. Such behaviour can be experienced in heavily built-up streets, in light wind conditions and with heavy traffic.
- Since canyon effects arise only when wind direction is nearly perpendicular to the street axis, the proposed procedure is applicable only when $3D$ effects are negligible and when (Oke, 1987) the angle between the wind and the perpendicular to the street is less than 20°; when the wind angle exceeds the above limit, an along-canyon component is observed, which cannot be neglected and cannot be simulated through a $2D$ model.
- Difference in concentration between the two sides of the canyon can be observed, especially in the stable and neutral case (figures 6.21 and 6.22); higher concentration values seem to occur on the upwind side; under unstable conditions (figure 6.23) the pollution pattern is more uniform, as expected.
- The local values of the concentration field indicate that the structure of the fluctuations inside the canyon is characterized by spots of high and low concentrations which originate at ground level and move around, depending on the canyon configuration; these results are also confirmed by Gerdes and Olivari (1999).

Although the flow field is estimated with an approximate procedure, and three-dimensional effects are not included, results seem to agree quite well with the finite-volumes eulerian model (see figure 6.25). A possible explanation is that traffic conditions turn out to be more important than meteorological factors in determining the concentration of emitted pollutants.

Finally, we may notice that the discussed algorithm is quite time-consuming; hence, in the case in which $U \gg \sigma_U$ (therefore, not in wind calm), the turbulent fluctuations in

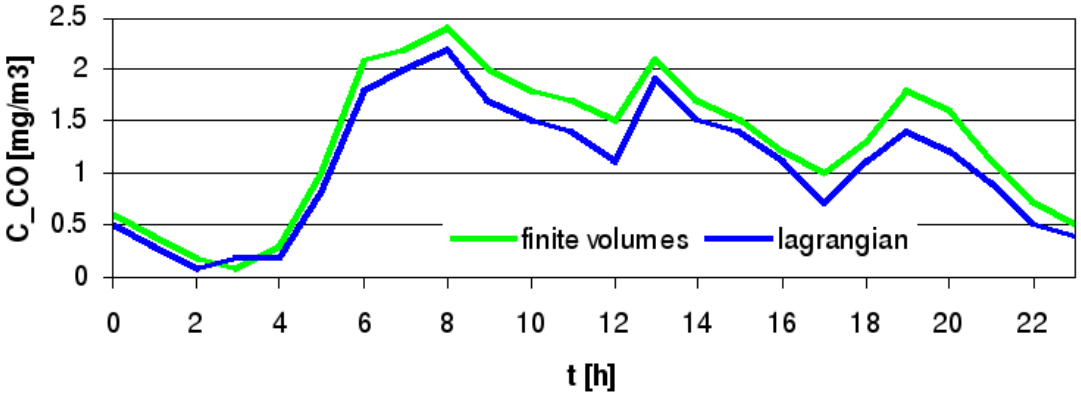

Figure 6.25.: Time evolution of concentration values at roof-level, averaged over the width of the first canyon of figures 6.21-6.24: comparison between lagrangian and finite-volumes eulerian model.

the horizontal direction can be neglected, as discussed in section 3.2.6. In any case, from a practical point of view, the present model may be profitably adopted to compute the virtual source located outside of the roughness (i.e. at roof-level, see section 5.4.1); it is then possible to insert a more realistic source term in a model working at a larger scale.

References

Airborne Particle Expert Group. Source apportionment of airborne particulate matter in the United Kingdom. Technical report, Department for Environment Food and Rural Affairs, UK, 1999.

K. J. Allwine, X. Bian, C. D. Whiteman, and H. W. Thistle. Valdrift: a valley atmopsheric dispersion model. J. Appl. Meteor., 36:1076–1087, 1996.

K. J. Allwine and C. D. Whiteman. Extraterrestrial solar radiation on inclined surfaces. Environmental software, 1:164–169, 1986.

D. Anfossi, E. Ferrero, G. Brusasca, A. Marzorati, and G. Tinarelli. A simple way of computing buoyant plume rise in lagrangian stochastic dispersion model. Atm. Env., 27A:1443–1451, 1993.

D. D. Apsley, D. J. Carruthers, R. Singles, C. McHugh, and S. J. Dyster. ADMS-Urban, An Urban Air Quality Management System. CERC, Cambridge, UK, 2000. Technical specification: Modelling wet deposition.

D. D. Apsley, S. J. Dyster, and C. McHugh. ADMS-Urban, An Urban Air Quality Management System. CERC, Cambridge, UK, 2003. Technical specification: Modelling dry deposition.

L. Arnold. Stochastic Differential Equations: Theory and Applications. Wiley, New York, 1974.

S. P. S. Arya. Air Pollution Meteorology and Dispersion. Oxford University Press, New York, 1999.

J. H. Baerentsen and R. Berkowicz. Monte Carlo simulation of plume dispersion in the convective boundary layer. Atm. Env., 18:701–712, 1984.

N. Bagal, E. R. Pardyjak, and M. J. Brown. Improved cavity parametrization for a fast response urban wind model. Technical report, Los Alamos National Laboratory, 2002.

J. F. Barlow, I. N. Harman, and S. E. Belcher. Scalar fluxes from urban street canyons. part i: Laboratory simulation. Bound. Layer Meteor., 2003. Submitted.

R. Berkowicz. OSPM: a parameterised street pollution model. Environmental Monitoring and Assessment, 65:323–331, 2000.

R. Berkowicz, O. Hertel, N. N. Sørensen, and J. A. Michelsen. Flow and Dispersion Through Groups of Obstacles, chapter Modelling air pollution from traffic in urban areas, pages 121–141. Clarendon Press, Oxford, 1997.

J. J. Berthelier, editor. Determination of Distributions in Simulation of Turbulent Dispersion, Paris, 1991.

A. K. Blackadar. The vertical distribution of wind and turbulent exchange in a neutral atmosphere. J. Geophys. Res., pages 3095–3102, 1962.

M. Bottema. Roughness parameters over regular rough surfaces: experimental requirements and model validation. J. Wind Eng. Indust. Aero., 64:249–265, 1996.

M. Bottema. Urban roughness modelling in relation to pollutant dispersion. Atm. Env., 31:3059–3075, 1997.

G. A. Briggs. Diffusion estimation for small emissions. Technical report, Atmospheric Turbulence and Diffusion Laboratory, NOAA, Oak Ridge, Tennessee, 1973.

G. A. Briggs. Lectures on Air Pollution and Environmental Impact Analysis, chapter Plume rise prediction. American Meteorological Society, New York, 1975.

J. Businger. Turbulent transfer in the atmospheric surface layer. In A. M. Soc., editor, Workshop in Micrometeorology, pages 1–69, 1973.

J. A. Businger. A note on the businger-dyer profiles. Bound. Layer Meteor., 42:145–151, 1988.

G. C. Crone. Parallel Lagrangian models for turbulent transport and chemistry. PhD thesis, Univ. Utrecht, Netherland, 1997.

P. de Haan. On the use of density kernels for concentration estimations within particle and puff dispersion models. Atm. Env., 33:2007–2021, 1999.

P. de Haan and M. W. Rotach. A puff-particle dispersion model. Int. J. Environment and Pollution, 5, 1995.

P. de Haan, M. W. Rotach, and M. Werfeli. Modification of an operational dispersion model for urban applications. J. Appl. Meteor., 40:864–879, 2001.

J. W. Deardorff. Parameterization of the planetary boundary layer for use in general circulation models. Mon. Wea. Rev., 100:93–106, 1972.

G. A. Degrazia, D. Anfossi, J. C. Carvalho, C. Mangia, T. Tirabassi, and H. F. Campos Velho. Turbulence parametrisation for pbl dispersion models in all stability conditions. Atm. Env., 34:3575–3583, 2000.

C. Demuth. A contribution to the analitical steady solution of the diffusion equation for line sources. Atm. Env., 12:1255–1258, 1978.

A. J. Dyer. A review of flux-profile relationships. Bound. Layer Meteor., 7:363–372, 1974.

A. J. Dyer and B. B. Hicks. Flux gradient transport of heat and watervapour in an unstable atmosphere. Q. J. R. Met. Soc., 93:501–508, 1970.

D. G. Erbs, S. A. Klein, and J. A. Duffie. Estimation of diffuse radiation fraction for hourly, daily and monthly average global radiation. Solar Energy Laboratory, University of Wisconsin, Madison, 1981.

R. Eskridge and S. T. Rao. Measurement and prediction of traffic-induced turbulence and velocity fields near highways. J. Appl. Meteor., August 1983.

R. E. Eskridge, W. B. Petersen, and S. T. Rao. Turbulent diffusion behind vehicles: Effect of traffic speed on pollutant concentrations. J. Air and Waste Mgmt. Assoc., March 1991.

T. K. Flesch and J. D. Wilson. A two-dimensional trajectory-simulation model for non-gaussian, inhomogeneous turbulence within plant canopies. Bound. Layer Meteor., 61: 349–374, 1992.

C. W. Gardiner. Handbook of Stochastic Processes for Physics, Chemistry and Natural Sciences. Springer Verlag, Berlin, 1983.

J. R. Garratt. The atmospheric boundary layer. Cambridge University Press, 1992.

F. Gerdes and D. Olivari. Analysis of pollutant dispersion in an urban street canyon. Journal of Wind Engeneering and Industrial Aerodynamics, 82:105–124, 1999.

F. A. Gifford. Further data on relative atmospheric diffusion. J. Meteorol., 14:475–476, 1957a.

F. A. Gifford. Relative atmospheric diffusion of smoke puffs. J. Meteorol., 14:410–414, 1957b.

F. A. Gifford. Statistical properties of a fluctuating plume dispersion model. Adv. Geophys., 6:117–138, 1959.

G. H. Goudsmit, F. Peters, M. Gloor, and A. Wuest. Boundary versus diapycnal mixing in stratified natural waters. J. Geophys. Res., pages 903–914, 1997.

S.-E. Gryning, E. Batchvarova, M. W. Rotach, A. Christen, and R. Vogt. Roof level urban tracer experiment: measurements and modelling. In 26 NATO/CCMS international technical meeting on air pollution modelling and its application, Istanbul, Turkey, 2003.

S.-E. Gryning, A. A. M. Holtslag, J. S. Irwin, and B. Sivertsen. Applied dispersion modelling based on meteorological scaling parameters. Atm. Env., 21:79–89, 1987.

G. Haltiner. Numerical prediction and dynamic meteorology. John Wiley and Sons, New York, 1980.

S. R. Hanna and J. C. Chang. Boundary layer parametrization for applied dispersion modeling over urban areas. Bound. Layer Meteor., 58:229–259, 1992.

I. N. Harman, J. F. Barlow, and S. E. Belcher. Scalar fluxes from urban street canyons. part ii: Model. Bound. Layer Meteor., 2003. Submitted.

S. Heinz and H. van Dop. Buoyant plume rise described by a lagrangian turbulence model. Atm. Env., 33:2031–2043, 1999.

W. C. Hinds. Particulate air pollution. Technical report, UCLA Institute of the Environment, 2001.

U. Hogstrom. Non-dimensional wind and temperature profiles in the atmospheric surface layer: a re-evaluation. Bound. Layer Meteor., 42:55–78, 1988.

A. A. M. Holtslag and C.-H. Moeng. Eddy diffusivity and countergradient transport in the convective atmospheric boundary layer. J. Atmos. Sci., 48:1690–1698, 1991.

A. A. M. Holtslag and A. P. van Ulden. A simple scheme for daytime estimates of the surface fluxes from routine weather data. J. Clim. App. Meteor., 22:517–529, 1983.

R. S. Hotchkiss and F. H. Harlow. Air pollution transport in street canyons. In Report by Los Alamos Scientific Laboratory for US Environmental Protection Agency, 1973.

C. H. Huang. A theory of dispersion in turbulent shear flow. Atm. Env., 13:453–463, 1979.

Y. Ichikawa and K. Sada. An atmospheric dispersion model for the environmental impact assessment of thermal power plants in japan - a method for evaluating topographical effects. J. Air and Waste Manage. Assoc., 52:313–323, 2002.

M. Iqbal. An Introduction to Solar Radiation. Academic Press, New York, 1983.

A. S. Kao and C. Venkataraman. Estimating the contribution of reentrainment to the atmospheric deposition of dioxin. Chemosphere, 31:4317–4331, 1995.

H. Kaplan and N. Dinar. A lagrangian dispersion model for calculating concentration distribution within a built-up domain. Atm. Env., 30:4197–4207, 1996.

K. Koeltzsch. On the relationship between the lagrangian and eulerian time scale. Atm. Env., 33:117–128, 1999.

I. Y. Lee and H. M. Park. Parametrization of the pollutant transport and dispersion in urban street canyons. Atm. Env., 28:2343–2349, 1994.

H. Lettau. Note on aerodynamic roughness parameter estimation on the basis of roughness element description. J. Appl. Meteor., 8:828–832, 1969.

R. J. Leveque. High-resolution conservative algorithms for advection in incompressible flow. J. Num. Anal., 33:627–665, April 1996.

A. K. Luhar and R. E. Bitter. A random walk model for dispersion in inhomogeneous turbulence in a convective boundary layer. Atm. Env., 23:1911–1924, 1989.

A. K. Luhar, M. F. Hibberd, and P. J. Hurley. Comparison of closure schemes used to specify the velocity pdf in lagrangian stochastic dispersion models for convective conditions. Atm. Env., 30:1407–1418, 1996.

A. K. Luhar and S. T. Rao. Lagrangian stochastic dispersion model simulations of tracer data in nocturnal flows over complex terrain. Atm. Env., 28:3417–3431, 1994.

J. L. Lumley and H. A. Panofsky. The structure of atmospheric turbulence. John Wiley and Sons, New York, 1964.

R. W. Macdonald, R. F. Griffiths, and D. J. Hall. An improved method for the estimation of surface roughness of obstacle arrays. Atm. Env., 32:1857–1864, 1998.

A. Martilli, A. Clappier, and M. Rotach. An urban surface exchange parameterisation for mesoscale models. Bound. Layer Meteor., 104:261–304, 2002.

A. S. Monin and A. M. Yaglom. Statistical Fluid Mechanics, volume 2, page 874. MIT Press, Cambridge, 1975.

P. Monti and G. Leuzzi. A closure to derive a three-dimensional well-mixed trajectory model for non-gaussian, inhomogeneous turbulence. Bound. Layer Meteor., 80:311–331, 1996.

N. Moussiopoulos, E. Berge, T. Bohler, F. de Leeuw, E. Gronskey, S. Mylona, and M. Tombrou. Ambient air quality: pollutant dispersion and transport models. European Environmental Agency, 1996.

Y. Nakamura and T. R. Oke. Wind, temperature and stability conditions in an e-w oriented urban canyon. Atm. Env., 1989.

F. T. M. Nieuwstadt. The turbulent structure of the stable, nocturnal boundary layer. J. Atmos. Sci., 41:2202–2216, 1984.

L. Ntziachristos and Z. Samaras. Copert III: Computer programme to calculate emissions from road transport. Technical report, Lab of Applied Thermodynamics, Aristotle University of Thessaloniki, 2000.

J. O'Brien. A note on the vertical structure of the eddy exchange coefficient in the planetary boundary layer. J. Atmos. Sci., 27:1213–1215, 1970.

T. R. Oke. The energetic basis of the urban heat island. Q. J. R. Met. Soc., 108:1–24, 1982.

T. R. Oke. Boundary Layer Climates. Routledge, Cambridge, 1987.

G. W. Paltridge and C. M. Platt. Radiative processes in meteorology and climatology. Elsevier, 1976.

H. A. Panofsky and J. A. Dutton. Atmospheric turbulence. Models and methods for engineering applications. Wiley-Interscience Publication, New York, 1984.

E. R. Pardyjak, M. J. Brown, and N. Bagal. Improved velocity deficit parametrization for a fast response urban wind model. Technical report, Los Alamos National Laboratory, 2002.

F. Pasquill and F. B. Smith. Atmospheric diffusion. Ellis Horwood Ltd., 1983.

C. A. Paulson. The matematical representation of wind speed profile and temperature in the unstable atmospheric boundary layer. J. Appl. Meteor., 9:857–861, 1970.

R. A. Pielke. Mesoscale meteorological modelling. Academic Press, 2nd edition, 2002.

G. Rampanelli. Investigation of Diurnal Atmospheric Boundary Layer Dynamics in Alpine Valleys. PhD thesis, Dept. of Civil and Env. Engineering, Univ. of Trento, Italy, 2004.

A. Robins and R. MacDonald. Review of flow and dispersion in the vicinity of groups of buildings. Technical report, University of Surrey, 2001.

R. Röckle. Bestimmung der Stomungsverhaltnisse im Bereich komplexer Bebauungsstrukturen. PhD thesis, Fachbereich Mechanik der Technischen Hochschule Darmstadt, Germany, 1990.

M. Rotach. Estimation of the wind speed at an urban reference height from an observation at some other height. Technical report, 2000. Meteorology applied to Urban Air Pollution Problems - COST 715.

M. W. Rotach. Turbulence close to a rough urban surface. part i: Reynolds stress. Bound. Layer Meteor., 65:1–28, 1993a.

M. W. Rotach. Turbulence close to a rough urban surface part ii: Variances and gradients. Bound. Layer Meteor., 66:75–92, 1993b.

M. W. Rotach. Determination of the zero plane displacement in an urban environment. Bound. Layer Meteor., 67:187–193, 1994.

M. W. Rotach. Towards meteorological preprocessing for dispersion models in an urban environment. Inter. J. Environment Pollution, 8:548–556, 1997.

M. W. Rotach. Simulations of urban-scale dispersion using a lagrangian stochastic dispersion model. Bound. Layer Meteor., 99:379–410, 2001.

M. Roth and T. R. Oke. Turbulent transfer relationships over an urban surface. i: Spectral characteristics. Q. J. R. Met. Soc., 119:1071–1104, 1993.

M. Santamouris and E. Dascalaki. Wind speed in the urban environment. Technical report, Group Building Environmental Studies, Physics Department, University of Athens, 2003.

L. Santomauro. Dinamica dell'inquinamento atmosferico da impianti industriali. Edizioni Calderini, Bologna, 1975.

B. L. Sawford. Generalized random forcing in random-walk turbulent dispersion models. Phys. Fluids, 29:3582–3585, 1986.

J. S. Scire, F. R. Robe, M. E. Fernau, and R. J. Yamartino. A User's Guide for the CALMET Metorological Model, 1999.

J. S. Scire, D. G. Strimaitis, and R. J. Yamartino. A User's Guide for the CALPUFF Dispersion Model, 2000.

L. Sedefian, S. T. Rao, and W. Petersen. Comments on determination of vehicle emission rates from roadways by mass balance techniques. Environ. Sci. and Tech., March 1981.

G. A. Sehmel. Particle and gas dry deposition: a review. Atmospheric Environment, 14: 1002, 1980.

R. Singles and C. McHugh. ADMS-Urban, An Urban Air Quality Management System. CERC, Cambridge, UK, 2003. Technical specification: Simple NOx chemistry module.

R. Sozzi, T. Georgiadis, and M. Valentini. Introduzione alla turbolenza atmosferica. Pitagora Editrice, Bologna, Italy, 2002.

J. W. Spencer. Fourier series representation of the position of the sun. Search, 2:172, 1971.

A. Stohl. Computation, accuracy and applications of trajectories: a review and bibliography. Atm. Env., 32:947–966, 1998.

R. B. Stull. An introduction to boundary layer meteorology. Kluwer Academic Publishers, 1988.

F. Tampieri. Processi di diffusione nello strato limite atmosferico. Attività seminariali dell'Università degli studi di Trento, 1997.

H. Tennekes. The logarithmic wind profile. J. Atmos. Sci., 30:234–238, 1973.

A. S. Thom. Momentum, mass and heat exchange of plant communities, volume 1, pages 57–109. Academic Press, 1975.

D. J. Thomson. Criteria for the selection of stochastic models of particle trajectories in turbulent flows. J. Fluid. Mech., 180:529–556, 1987.

D. J. Thomson and A. J. Manning. Along-wind dispersion in light wind condition. Bound. Layer Meteor., 98:341–358, 1995.

G. Tinarelli, D. Anfossi, E. Ferrero, U. Giostra, M. G. Morselli, J. Moussafir, F. Tampieri, and F. Trombetti. Lagrangian particle simulation of tracer in the lee of a schematic two-dimensional hill. J. Appl. Meteor., 33:744–756, 1994.

I. Troen and L. Mahrt. A simple model of the atmospheric boundary layer; sensitivity to surface evaporation. Bound. Layer Meteor., 37:129–148, 1986.

F. Trombetti and M. Tagliazucca. Characteristic scales of atmospheric surface layer. Technical report, FISBAT-CNR, Bologna, Italy, 1994.

D. B. Turner. Workbook of Atmospheric Dispersion Estimates. Lewis Publishers, 1994.

A. P. van Ulden. Simple estimates for vertical diffusion from sources near the ground. Atm. Env., 12:2125–2129, 1978.

A. P. van Ulden and A. A. M. Holtslag. Estimation of atmospheric boundary layer parameters for diffusion application. J. Clim. App. Meteor., 24:1196–1207, 1985.

C. D. Whiteman. Breakup of temperature inversions in deep mountain valleys: Part i. observations. J. Appl. Meteor., 21:270–289, 1982.

C. D. Whiteman and B. T. McKee. Breakup of temperature inversion in deep mountain valleys: Part ii. thermodynamic model. J. Appl. Meteor., 21:290–302, 1982.

J. D. Wilson and B. L. Sawford. Review of lagrangian stochastic models for trajectories in the turbulent atmosphere. Bound. Layer Meteor., 78:191–210, 1996.

R. J. Yamartino and G. Wiegand. Development and evaluation of simple models for the flow, turbulence and pollution concentration fields within an urban street canyon. Atm. Env., 20:2137–2156, 1986.

P. Zannetti. Air pollution modelling: theories, computational methods and available software. Van Nostrand Reinhold, New York, 1990.

M. Zanoni. Implementazione di un sistema integrato gis-database per la gestione dei dati di traffico e produzione di mappe delle emissioni. applicazione alla città di trento. Master's thesis, Facoltà di Ingegneria, Università di Trento, Italy, 2002.